

**Jets, Substructure, and Searching for Dark Matter
at the Large Hadron Collider**

by

Siddharth Madhavan Narayanan

Submitted to the Department of Physics
in partial fulfillment of the requirements for the degree of

Doctor of Philosophy

at the

MASSACHUSETTS INSTITUTE OF TECHNOLOGY

August 2018

© Massachusetts Institute of Technology 2018. All rights reserved.

Author
Department of Physics
August 32, 2018

Certified by
Christoph M. E. Paus
Professor of Physics
Thesis Supervisor

Accepted by
Somebody
Chairman, Department Committee on Graduate Theses

Jets, Substructure, and Searching for Dark Matter at the Large Hadron Collider

by

Siddharth Madhavan Narayanan

Submitted to the Department of Physics
on August 32, 2018, in partial fulfillment of the
requirements for the degree of
Doctor of Philosophy

Abstract

Astrophysical observations of gravitational interactions provide strong evidence for the existence of dark matter (DM). Many theories propose and experiments test the hypothesis that DM may have a particle physics origin, but this remains unproven. One such experiment is the Compact Muon Solenoid (CMS) at the Large Hadron Collider (LHC). If DM couples to particles present in protons, it is possible that DM is produced in collisions at the LHC. Because DM is effectively invisible to CMS, we must look for collisions in which DM is produced in association with one or more Standard Model (SM) particles. This thesis describes two different scenarios for the SM particle hypothesis: a single top quark or two light quarks. Both cases result in complicated detector signatures due to the hadronization of final-state quarks. Improved jet substructure techniques to identify some of these unique signatures are presented. Since the observed data is consistent with SM backgrounds in all searches, we translate this result into the most stringent constraints to date on the relevant beyond-SM models.

Thesis Supervisor: Christoph M. E. Paus

Title: Professor of Physics

Contents

1 The CMS experiment at the LHC	7
1.1 The Large Hadron Collider	7
1.2 The Compact Muon Solenoid	10
1.3 Particle reconstruction and identification	20
1.4 Simulation of collisions	24
1.4.1 Physics simulation	24
1.4.2 Detector simulation	24
2 Hadronic Resonance Identification	25
2.1 Reconstruction	25
2.2 Identification	28
2.2.1 Substructure	30
2.2.2 A combined tagger	36
2.3 Data validation	41
3 The Search for $t + p_T^{\text{miss}}$	47
3.1 Signal selection	51
3.1.1 Online trigger selection	52
3.1.2 Offline signal selection	53
3.2 Background estimation	56
3.2.1 Visible final states to constrain invisible final states	56
3.2.2 Theoretically-limited extrapolations	70
3.3 Results	76

3.3.1	Constraints on mono-top models	80
4	The Search for Invisible Decays of the Higgs Boson	85
4.1	Signal selection	86
4.1.1	Online trigger selection	86
4.1.2	EW and QCD production of electroweak bosons	94
4.1.3	Sensitivity optimization	97
4.2	Background estimation	98
4.3	Results	100

Chapter 1

The CMS experiment at the LHC

1.1 The Large Hadron Collider

The Large Hadron Collider (LHC) [17]¹ is a circular particle accelerator, 27 km in circumference and between 40 and 175 m below the surface of the French-Swiss border. Designed to collide protons at a maximum center-of-mass energy $\sqrt{s} = 14$ TeV, the LHC has delivered collisions at $\sqrt{s} = 7, 8$ TeV (Run 1) and $\sqrt{s} = 13$ TeV (Run 2); the target energy $\sqrt{s} = 14$ TeV will be reached in Run 3. In addition to protons, the LHC accelerates and collides heavy nuclei (Pb and Xe) at lower values of \sqrt{s} . In this thesis, we focus exclusively on data recorded from proton collisions during Run 2.

Protons are brought to the LHC by the multi-stage process [5] depicted in Figure 1.1. Hydrogen atoms are stripped of electrons and accelerated by LINAC2 (a linear accelerator) to a kinetic energy of 50 MeV. LINAC2 then feeds the protons into the Booster ring (final energy of 1.4 GeV), followed by the Proton Synchrotron (26 GeV). From the PS, the protons are injected into the Super Proton Synchrotron (450 GeV). Protons exit the SPS and enter the LHC at one of two places, corresponding to two different beams traveling in opposite directions. The two beams intersect in eight places along the LHC, four of which are instrumented by a detector experiment: CMS, ATLAS, LHCb, and ALICE.

Each proton beam in the LHC is accelerated by eight superconducting cavities

¹Unless otherwise specified, all technical specifications of the LHC are derived from Reference [17]

□

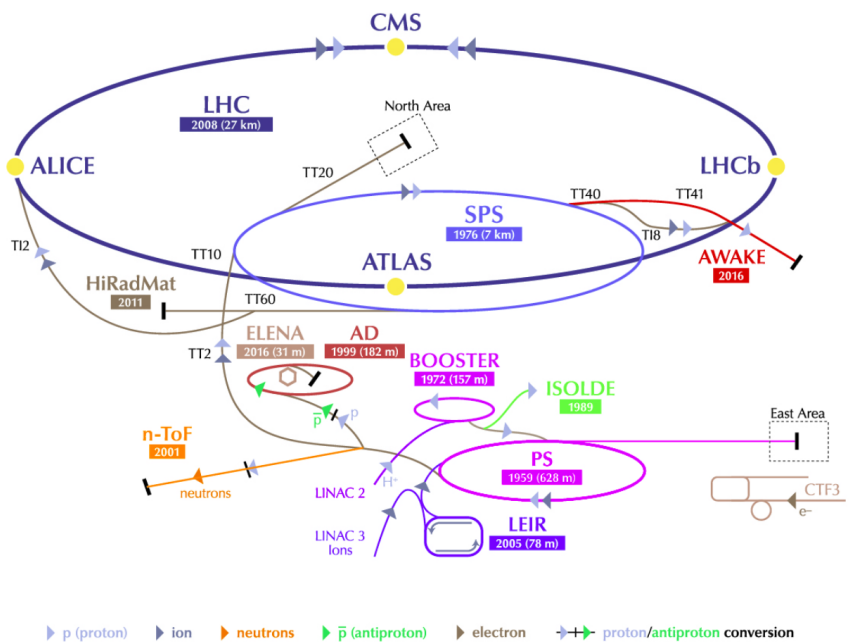


Figure 1.1: Diagram of the CERN accelerator complex. The LHC (dark blue) is fed protons (and heavy ions) by a chain of intermediate accelerators, beginning with LINAC2 (dark pink). Reprinted from Reference [12].

exerting radio frequency longitudinal (i.e. parallel to beam direction) electric fields with a frequency of 400 MHz, The maximum RF voltage seen by each beam is 16 MV per revolution. The physical and temporal design of the RF system creates bunches of protons (corresponding to nodes of the oscillating field) approximately 7.5 cm in length and separated by 25 ns. Superconducting NbTi dipole magnets bend the two proton beams in opposite directions as they travel around the ring. Each of the 1232 dipoles is 14 m long and exerts a transverse B field between 0.54 and 8.33 T. To achieve such high B fields, the magnets are cooled to 2 K by superfluid helium. In addition, a number of quadrupole magnets are used to focus and match the beams between the dipoles².

In addition to the center-of-mass energy \sqrt{s} , the other figure of merit is the number of events producing interesting physics processes, which is defined as:

$$N(pp \rightarrow X) = \int dt L\sigma(pp \rightarrow X) \quad (1.1)$$

where σ is the cross section of the relevant process and L is the instantaneous luminosity of the LHC. The cross section is fixed by nature, and so increasing the luminosity is the only handle to increase N . The instantaneous luminosity of two Gaussian beams is given by [17]:

$$L = \frac{N_b^2 n_b f_{\text{rev}} \gamma F}{4\pi \epsilon \beta^*} \quad (1.2)$$

where:

N_b = particles per bunch

n_b = bunches per beam

f_{rev} = frequency of revolution

$\gamma = E/m$ of beam

ϵ = emittance of beam

²Full details on the various quadrupoles can be found in Table 3.7 of Reference [17].

[]

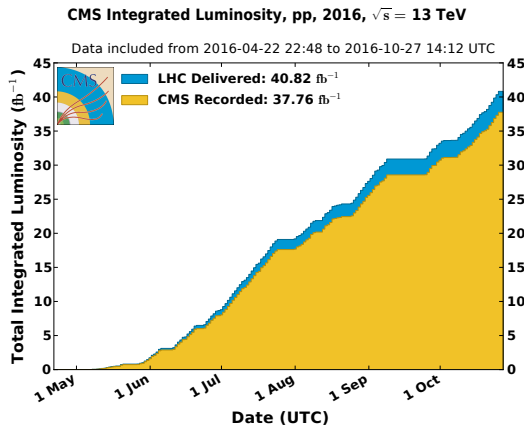


Figure 1.2: Integrated luminosity of the LHC during proton collisions during the 2016 data-taking period [10].

β^* = beta function at collision point

F = factor accounting for beam intersection geometry

The instantaneous luminosity evolves as a function of time, primarily due to n_b and N_b being modified by collisions. The total integrated luminosity after time T is:

$$L_{\text{int}} = \int_0^T dt L(t) = L(0) \tau_L \left(1 - e^{-T/\tau_L}\right) \quad (1.3)$$

where $\tau_L \approx 15 \text{ h}$ is the characteristic beam loss timescale and $L(0)$ is the instantaneous luminosity at $T = 0$. The LHC is designed to deliver $L(0) \sim \mathcal{O}(10^{34}) \text{ cm}^{-2}\text{s}^{-1}$. Figure 1.2 shows the total luminosity delivered by the LHC and recorded by CMS during the 2016 portion of Run 2.

1.2 The Compact Muon Solenoid

The Compact Muon Solenoid (CMS) [9] is one of two general purpose LHC detectors (the other being ATLAS). It is designed to detect and measure stable hadrons, photons, electrons, and muons produced in proton and ion collisions at LHC interaction point 5. From these event descriptions, a number of physics processes can be

probed, including SM measurements [??], BSM searches [??], and the discovery of the Higgs boson [??]. In what follows, we will use the (r, ϕ, η) coordinate system with respect to the z axis:

z = distance along beam axis, with $z = 0$ defined to be at the center of the detector

r = distance from the z axis

ϕ = azimuthal angle in the plane orthogonal to the z axis

η = pseudorapidity ($-\log \theta/2$), with respect to the polar angle θ

In this coordinate system, we define x and y to lie in the plane perpendicular to z , with x pointing from the center of the detector to the center of the LHC. As with the pseudorapidity, it is convenient to use quantities invariant under z -boosts, and so we define the transverse momentum:

$$\vec{p}_T = \begin{pmatrix} p_x \\ p_y \end{pmatrix} \quad (1.4)$$

We will frequently make use of the magnitude of this vector, p_T . CMS can detect collision products that are within the fiducial volume of $0 \leq \phi < 2\pi$ and $-5 \leq \eta \leq 5$. Several detector subsystems (Figure 1.3) are used to identify and reconstruct muons, electrons, photons, and charged and neutral hadrons.

Silicon tracker

Starting from the beam pipe, the first of these subsystems is the silicon tracker [8], used to identify charged particles and measure their momenta. The tracker consists of silicon detector geometries: pixels (providing 3D position measurement) and strips (2D). The arrangement of the pixel and strip layers are shown in Figure 1.4. A near-uniform 3.8 T magnetic field, produced by a superconducting NbTi solenoid, envelopes the tracker. The field lines in the tracker volume are approximately parallel to the beam direction.

[]

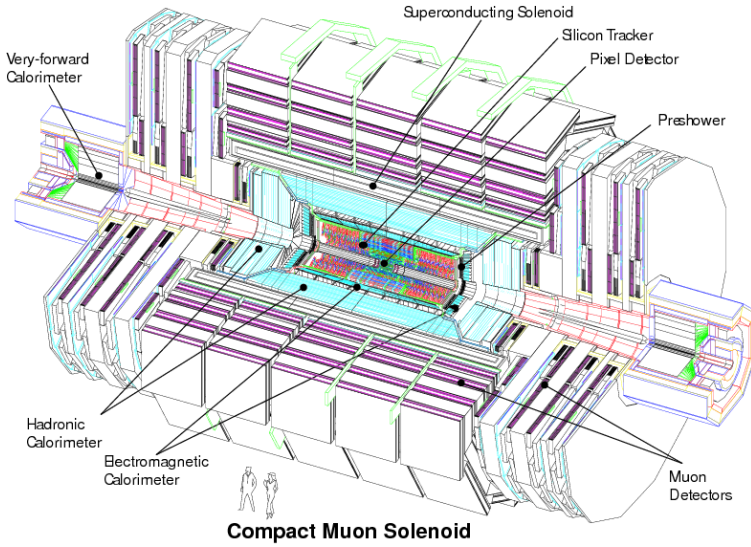


Figure 1.3: Cut-away view of the CMS detector and its subsystems. Reprinted from Reference [9].

A single silicon pixel has dimensions $285 \times 100 \times 150 \text{ } (\mu\text{m})^3$ (in $r \times r\phi \times z$), leading to a position resolution of $\sim 10 \times 30 \text{ } (\mu\text{m})^2$ (in $r\phi \times z$). The 66 million pixels are arranged into 7 layers: 3 cylindrical “barrels” (at $r = 4.4, 7.3, 10.2 \text{ cm}$) and 2×2 “endcap” annuli (at $z = \pm 34.5, \pm 46.5 \text{ cm}$). Outside the pixel layers are the strip layers, consisting of 9.3 million silicon strips arranged into barrels and endcaps. The resolution in $r\phi$ varies between 10 and 50 μm , depending on the location and pitch of the given strip. Certain strip layers contain two layers of strips, rotated through a “stereo” angle (100 mrad) with respect to each other. By matching adjacent hits, the stereo measurement can add a third dimension (z for barrel, r for endcap) to the strip’s 2D measurement, with resolution 100-500 μm . There are a total of 10 barrel layers ($0.2 < r < 1 \text{ m}$) and 24 endcap layers ($0.6 < |z| < 2.8 \text{ m}$).

Pixels with a signal greater than a tuneable readout threshold (typically around $3000Q_e$) are read out. These pixels are then aggregated with adjacent signals to form pixel clusters, which are further subjected to readout thresholds ($\sim 4000Q_e$). The exact position of the particle in this layer (known as a “hit”) is inferred by fitting the charge distribution of the pixels in this cluster to pre-determined templates. A similar

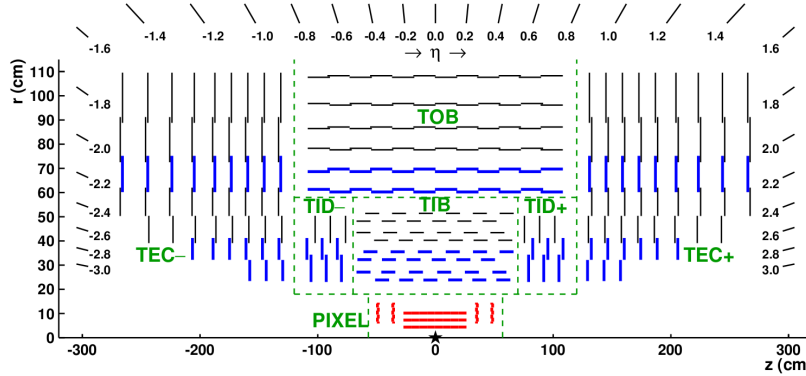


Figure 1.4: Diagram of a slice of the CMS tracking system. The pixel layers are shown in bold red lines. Single-strip (double-strip) layers are indicated by thin black (bold blue) lines. The double-strip modules each consist of two back-to-back strips, rotated with respect to each other, that can provide 3D localization of the hits. Reprinted from Reference [8].

method is employed to determine the strip hit positions, with some modifications to account for Lorentz drift of the charges in the silicon detector due to the B -field. The efficiency of reconstructing hits varies with the detector type, location, and particle momentum, but is generally greater than 99% (99.5% if defective modules are not considered).

Tracks are found using an iterative “inside-out” process, where each iteration has five steps:

1. Define seeds using pixel hits, double-strip hits (i.e. hits with 3D information), and an estimate of the beam spot (collision point). At least 3 hits are needed for the seed.
2. Use a Kalman filter [7, 18] to evolve track seeds through the rest of the tracker and find hits, accounting for the B -field and energy loss.
3. Estimate trajectory parameters after finding all hits.
4. Decide whether to keep found tracks based on quality requirements (e.g. number of missing hits, track χ^2)
5. Remove hits associated with tracks from hit collection and repeat.

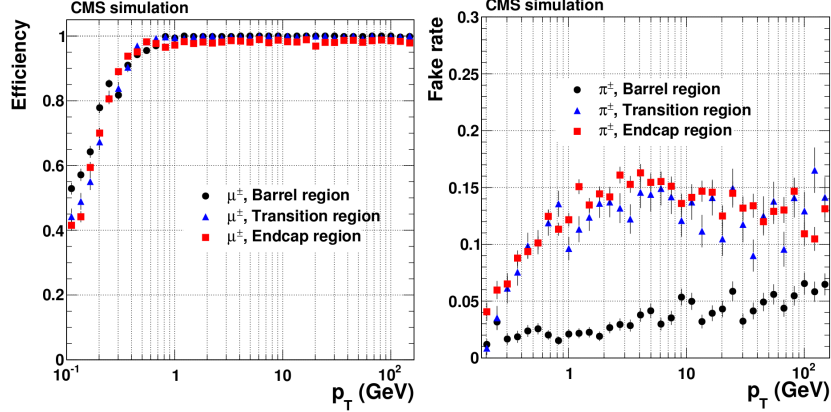


Figure 1.5: Efficiency (fake rate) of the CMS track fit algorithm, evaluated using simulation of muons (charged pions). Reprinted from Reference [8].

The trajectory parameters referred to in step 3 are the 5 parameters of a helix: ρ (curvature), ϕ_0 (azimuthal angle), λ ($\cot\theta$), d_0 (“impact parameter”, minimum r of track), z_0 (minimum $|z|$ of track). The CMS track fit typically has 5-7 iterations, with each successive iteration loosening the seed and track fit requirements to look for more difficult tracks (e.g. missing hits, large d_0). The efficiency and fake rate of this reconstruction, as a function of track p_T , are shown in Figure 1.5. For muons with $|\eta| < 1.5$ and $p_T > 1$ GeV, the tracking efficiency is over 98%, with a combinatorial fake rate of 2-6%.

The excellent position resolution of the pixel detector is used to accurately measure the position of primary vertices, as well as any secondary vertices from the decays of long-lived particles. In the former case, tracks are first clustered together on the basis of the likelihood that the tracks in a cluster arise from a single primary vertex. This is done using a deterministic annealing algorithm [27], which has as free parameters the number of clusters and the probability of each track belonging to each cluster. Having determined the clusters, an adaptive fit algorithm [19] is used to determine the vertex for each cluster. The free parameters of this fit are the three spatial coordinates of the vertex. As the LHC collides bunches of $\mathcal{O}(10^{11})$ protons, we expect multiple primary vertices in a single collision, and this is reflected in Figure 1.6. The vertex defined to

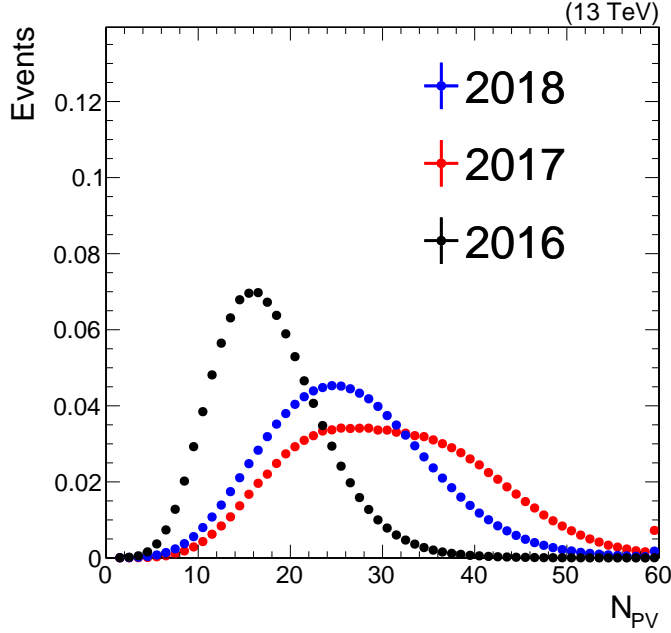


Figure 1.6: The distribution of the number of reconstructed primary vertices in data recorded by CMS during Run 2 of the LHC. While the results in this thesis only concern 2016 data, we show the evolution of N_{PV} as a function of time, as this correlates directly with increased instantaneous luminosity.

be the hard scattering interaction (known as *the* primary vertex³) is the vertex which maximizes:

$$\sum_{j \in \text{track jets}} (p_T^j)^2 + (p_T^{\text{miss}})^2 \quad (1.5)$$

where “track jets” refer to jets (Section 1.3) clustered from the vertex’s tracks, and p_T^{miss} is defined in Section 1.3.

The last reconstruction algorithm concerning the tracker alone is the identification of secondary vertices, which arise from the decay of long-lived particles (e.g. B mesons). The inclusive vertex fitter (IVF) [29] reconstructs such secondary vertices by the following steps:

1. Select a track as a seed if it satisfies $\sqrt{d_0^2 + d_z^2} > 50 \mu\text{m}$ and $d_0 > 1.2\delta d_0$.
2. Choose nearby tracks based on their closest distance to and opening angle with

³This nomenclature is indeed confusing, defining the singular primary vertex to be one of many primary vertices. However, it is standard terminology in CMS publications, so we will continue to use it. In what follows, the distinction will be clear

the seed track.

3. Fit the tracks to a displaced vertex using the adaptive fitter [19].
4. Decide which tracks belong to the candidate secondary vertex and which belong to the primary vertex.
5. Re-fit the secondary vertex position only using the former set of tracks from the previous step.

It is important not only to properly determine the location of the secondary vertex, but also to properly assign tracks. Observables that are a function of the *tracks* (e.g. vertex mass) will be critical for b jet tagging.

Electromagnetic calorimeter

The CMS electromagnetic calorimeter [4] (ECAL) is a homogenous detector with good energy and angular resolution, composed of 76,000 PbWO₄ crystals. The crystals are arranged in two sections: a cylindrical barrel (EB) covering $|\eta| < 1.44$ and two endcap annuli (EE) extending to $|\eta| < 3$. This provides slightly more coverage than the tracking volume. Each crystal in the EB (EE) has dimensions $2.2 \times 2.2 \times 23$ ($2.68 \times 2.68 \times 22$) (cm³), with the long dimension pointing towards the beam. This can be compared to a Moli  re radius $r_M = 2.19$ cm and a radiation length of $X_0 = 0.89$ cm. A cross-sectional area comparable to $r_M \times r_M$ facilitates the differentiation of different electromagnetic (EM) showers arising from electrons and photons. The depth of the crystal (in units of X_0) drives the excellent energy resolution, which is determined using a electron beam:

$$\frac{\sigma_E}{E} = \frac{2.8\%}{\sqrt{E/\text{GeV}}} \oplus \frac{12\%}{E/\text{GeV}} \oplus 0.3\% \quad (1.6)$$

Scintillation photons from the PbWO₄ crystals are collected by avalanche photodiodes (APDs) in the EB and vacuum phototriodes (VPTs) in the EE, which provide amplification factors of 50 and 10, respectively.

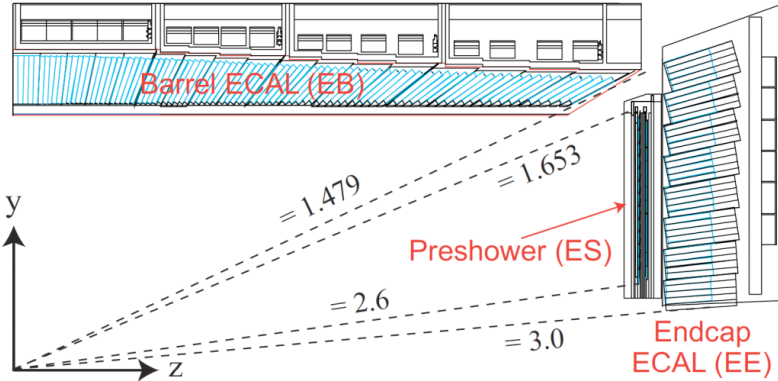


Figure 1.7: One quadrant of the CMS ECAL (symmetric with rotation around z and reflection across $z = 0$). The dashed lines indicate values of η . Reprinted from Reference [4].

At high momenta, the two photons from a π^0 decay may merge into a single ECAL crystal. This primarily occurs at high $|\eta|$ due to the z -boost of the initial state. To differentiate one- and two-photon deposits, a “preshower” detector sits in front of the EE ($1.6 < |\eta| < 2.5$). The preshower detector consists of a lead absorber and silicon strips. A photon (or photon pair) initiates a shower in the lead. The shower can be resolved in the silicon strips, which have resolution $\mathcal{O}(1\text{--}10)$ mm.

The physical placement of all three ECAL components is shown in Figure 1.7.

Due to the bending of a charged particle’s trajectory in the solenoidal B -field, bremsstrahlung photons will be emitted at similar values of η , but spread along ϕ . A “supercluster” (SC) is defined by clustering nearby ECAL energy depositions, allowing for a wider spread in ϕ than in η (Figure 1.8). The particle’s EM energy is defined to be the weighted sum of the energies of all crystals in the SC, where the coefficients account for crystal-specific calibration effects [22]. For an electron or photon, the EM energy is typically the energy of the particle, whereas for other particles (charged hadrons and some muons), it is only a fraction of the total energy.

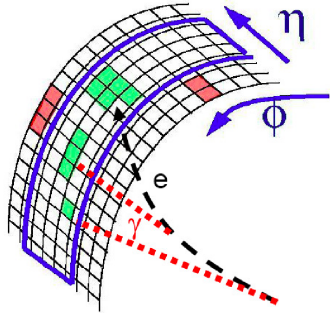


Figure 1.8: The combination of multiple ECAL crystals into a single supercluster, intended to capture energy depositions from bremsstrahlung photons. Reprinted from Reference [6].

Hadronic calorimeter

Muon chambers

The muon detectors are gas ionization chambers and are the outermost component of CMS [30]. The chambers are interleaved with the steel return yoke of the CMS magnet, ensuring a B -field which runs anti-parallel to the field inside the solenoid. This results in the characteristic S -shape of muon trajectories, as the bending changes direction across the solenoid. 3 types of ionization detectors are used: drift tubes (DTs; barrel), cathode strip chambers (CSCs; endcaps), and resistive plate chambers (RPCs; barrel and endcaps). The physical placement of the detectors is shown in Figure 1.9.

The DT cells are filled with a 85%/15% mix of argon and carbon dioxide, with a gold/steel anode wire held at a voltage of 3600 V. The cell is a rectangular prism, with transverse dimensions of $42 \times 13 \text{ mm}^2$ and a longitudinal dimension ranging from 1.9 to 4.1 m. The dimensions and the drift speed of $55\mu\text{m}/\text{s}$ result in a maximum response (drift) time of 400 ns. The DTs are organized into cylindrical “stations” (MB). With the exception of the outermost barrel station (MB4), each MB consists of 3 “superlayers” (SLs). Each SL has 4 parallel drift cells, and so measure position in a particular plane. Of the 3 SLs, two measure $r\text{-}\phi$ position and one measures $r\text{-}z$ position. MB4 does not have an $r\text{-}z$ SL.

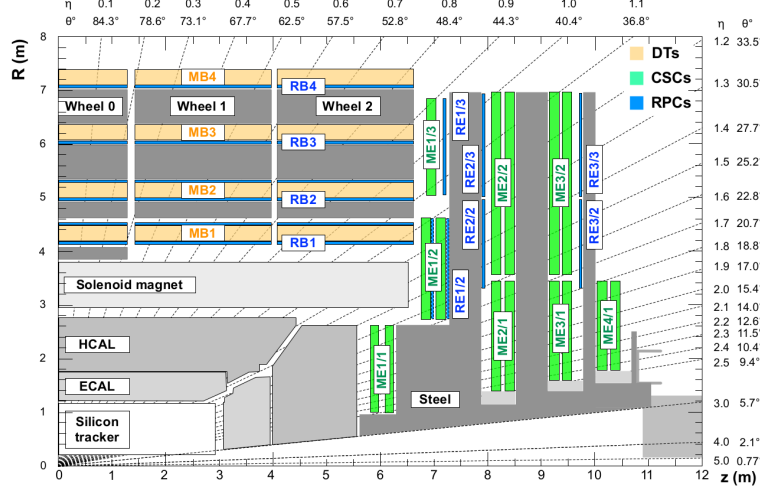


Figure 1.9: One quadrant of the CMS muon detection system, with the DTs (MBs), CSCs (MEs), and RPCs (RBs/REs) labeled. Reprinted from Reference [30].

The endcap is instrumented with CSCs as these have a faster response time and better spatial resolution than DTs. This is needed in the forward region, where both the muon and background fluxes are higher. While the CSC dimensions vary depending on the position of the chamber, each is instrumented with 80 cathode strips, held at voltages (relative to the anode) of 2.9-3.6 kV. The CSC wires have a separation of 2.5-3.16 mm, which governs the position resolution. A 50%/40%/10% mix of CO₂/Ar/CF₄ is used to fill the chambers.

RPCs are interspersed among the DTs and CSCs in both the barrel and endcap. These serve as a very fast muon detector (~ 1 ns) for the online trigger system. The spatial resolution of the RPC hits is worse than the DTs and CSCs.

The hit position resolution of the DTs is 78-120 μm (140-390 μm) in r - ϕ (r - z). For CSC, the resolution varies from 40 to 152 μm . The efficiency of individual reconstructed hits (“rechits”) is over 95%.

Online trigger system

1.3 Particle reconstruction and identification

Particle flow algorithm

Because of the excellent angular granularity of the CMS detector and the momentum resolution of the tracker, a particle flow [28] algorithm is used to correlate information from all detector subsystems to build a global description of each event. Particle flow (PF) algorithms date back to ALEPH [??], and are in contrast to detector-specific physics object-based algorithms used at other experiments (e.g. References [??]).

The key feature of the PF algorithm is to “link” multiple detector signals together into a single PF candidate. This linkage combines inner tracks, ECAL clusters, HCAL clusters, and muon tracks based on their proximity in the (η, ϕ) plane. Inner track helices are extended into the calorimeters, searching for clusters compatible with the trajectory. Similarly, clusters from the ECAL, the ECAL preshower, and the HCAL can be linked without a track present. The remainder of this section is organized according to “blocks” in the PF algorithm. At the end of each block, any detector signature (track, calorimeter cell) which has been assigned to a PF candidate in that block is removed from the set of objects passed to the next block. For example, tracks associated with muons will not be considered when reconstructing charged hadrons.

Muons

The first block of the PF algorithm links inner tracks and muon chamber hits to identify muons. While “standalone” muons can rely solely on muon chamber hits, we also consider muons that use the inner tracker. To construct outside-in “global muons”, standalone muon tracks are first reconstructed using a Kalman filter fit using muon chamber rechits [3, 30]. These standalone tracks are extrapolated inwards to the inner tracker, accounting for effects from the magnetic field and the material budget between the tracker and the muon chambers. A second Kalman filter fit is run to combine the inner track with the standalone track to form a global muon. To

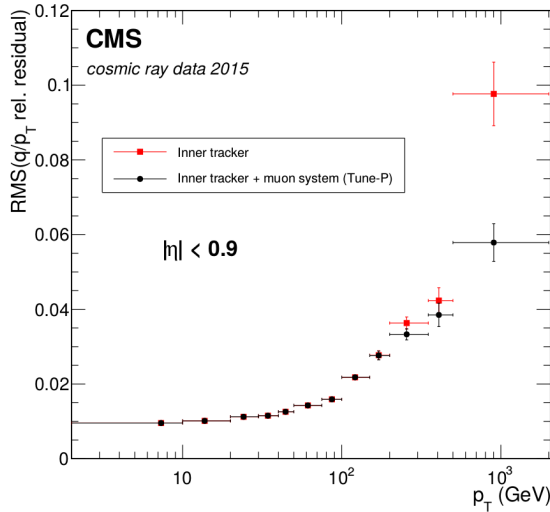


Figure 1.10: Resolution of muon q/p_T , compared between global muon reconstruction and the inner tracks corresponding to muons. The quantity q/p_T is used because the distribution is approximately Gaussian. The salient feature is that the muon systems become important to the momentum measurement at approximately 200 GeV. Reprinted from Reference [30].

reject backgrounds, requirements are placed on the χ^2/N_{dof} (poorly fit tracks, charged hadrons) and d_0, d_z (muons from hadron decays and cosmic rays). The total efficiency of global muon reconstruction is 99%. In addition, “tracker” muons can be reconstructed from the inside-out, extrapolating inner tracks to the muon chambers and re-fitting with muon rechits. The PF algorithm uses both global and tracker muons, but in this thesis, we will only use the former. Figure 1.10 shows the momentum resolution of global muons, compared to the momentum resolution of tracker-only muons (i.e. not using the muon chambers at all, not to be confused with inside-out tracker muons). The PF selection consumes all three types of reconstructed muons: global, tracker, and standalone.

We define two muon identification (ID) criteria that are slightly stronger than the PF selection. The first is a loose ID, which is used to veto muons when defining muon-free data samples. A loose muon is required to be either a global or tracker

Table 1.1: Observables used in identifying muons and rejecting backgrounds

Observable	Notes
p_T	Backgrounds grow at low p_T .
χ^2/N_{dof}	Ensure a good track fit.
$N_{\text{hit}}^{\mu\text{on}}$	At least one hit in the muon chamber in the global fit.
N_{stations}	At least two muon chamber stations contain segments of the track.
d_0	Track impact parameter, remove cosmic rays and hadron decays.
d_z	Track impact parameter, as above but also for pileup.
$N_{\text{hit}}^{\text{pixel}}$	At least one pixel hit.
$N_{\text{hit}}^{\text{tracker}}$	At least 5 hits in the tracker.

muon and have PF isolation less than 0.25. PF isolation is defined as:

$$\left(\sum_{i \in \text{PV charged had.}} p_T^{(i)} + \max \left\{ 0, \sum_{i \in \text{neut. had.}} p_T^{(i)} + \sum_{j \in \gamma} p_T^{(j)} - \frac{1}{2} \sum_{k \in \text{PU charged had.}} p_T^{(k)} \right\} \right) / p_T^{(\mu)} \quad (1.7)$$

where the sums are over PF candidates within $\Delta R < 0.4$ of the muon. PV and PU refer to the primary vertex and pileup vertices, respectively. The tight muon ID requires a global muon, PF isolation less than 0.15, and has selections on the criteria in Table 1.1. The efficiency

To account for differences between data and simulation in the performance of the muon IDs, corrections (known as scale factors) are derived:

$$\text{SF} = \frac{\epsilon_{\text{Data}}}{\epsilon_{\text{MC}}} \quad (1.8)$$

While ϵ_{MC} can be computed directly from MC truth information, ϵ_{Data} must be computed from $Z \rightarrow \mu\mu$ events, using one muon as a reference tag, and the other to probe the efficiency of the ID being tested.

Electrons and photons

Both electrons and photons are seeded using ECAL SCs, with electrons also being associated with an isolated track. Due to the significant material budget of the silicon

Table 1.2: Observables used in identifying electrons and rejecting hadron and photon backgrounds

Observable	Notes
p_T	Backgrounds grow at low p_T and brem. photons can make low- p_T tracking difficult.
$\sigma_{i\eta i\eta}$	Energy-weighted width of cell η in SC. Small for electrons.
$ \Delta\eta(\text{track, SC}) $	$\Delta\eta$ between SC seed crystal and GSF track at PV. Small for electrons.
$ \Delta\phi(\text{track, SC}) $	$\Delta\phi$, as above.
E_H/E_{EM}	Ratio of HCAL and ECAL energies. Large for hadrons.
PF isolation	Sum of energies of other PF candidates near electron. Large for particles in jets.
$ 1/E - 1/p $	Checks if ECAL and tracker agree ($m_e \sim 0$)
$N_{\text{hit}}^{\text{miss}}$	Conversions or bad tracks will have multiple missing hits in the inner tracker.
Conversion veto	Check for a pair of tracks originating at a displaced vertex.

tracker, electrons will lose a significant amount of energy through bremsstrahlung. Although this energy is partially recovered through the supercluster algorithm, the standard Kalman filter tracking fit does not properly account for the non-Gaussian hit uncertainties induced by bremsstrahlung. Therefore, a modified algorithm based on a Gaussian Sum Filter (GSF) [8, 1] is used to fit the track. Hits in the pixel and strip endcap layers consistent with the ECAL SC are used to seed the GSF fit. GSF differs from a Kalman filter by modeling the uncertainties as a Gaussian mixture model instead of a single Gaussian. The primary backgrounds for electron identification are (1) the overlap of a charged hadron with a neutral hadron or photon and (2) a photon which converts into a e^-/e^+ pair in the tracker. Table 1.2 lists the observables used to reject these backgrounds; two cut-based IDs are defined. The “loose” ID selects electrons with $\sim 90\%$ signal efficiency and $\sim 0.5\%$ background acceptance (strongly dependent on the electron phase space); it is used to *veto* electrons. The “tight” ID selects electrons with $\sim 70\%$ signal efficiency and $\sim 0.1\%$ background acceptance; it is used to *select* electron-pure samples.

Photons are defined as ECAL SCs without matched tracks. Table 1.3 describes

Table 1.3: Observables used in identifying photons and rejecting hadron backgrounds

Observable	Notes
p_T	Backgrounds grow at low p_T .
η	EB resolution is better than EE; less hadron background.
$\sigma_{i\eta i\eta}$	Defined in Table 1.2.
E_H/E_{EM}	Defined in Table 1.2.
PF isolations	Defined in Table 1.2. For photons, separate isolation criteria are placed on each PF type (photon, charged hadron, neutral hadron).

the selection variables used to define the loose veto ID ($\epsilon_{sig} \approx 90\%$, $\epsilon_{bkg} \approx 17\%$) and the tight selection ID ($\epsilon_{sig} \approx 82\%$, $\epsilon_{bkg} \approx 12\%$). The direction and energy of a photon are defined by the ECAL SC position and energy, respectively.

To calibrate ECAL SCs, we define the $R_9 = E_{3\times 3}/E_{SC}$. $E_{3\times 3}$ is the sum of the energies of the crystals in a 3×3 square centered on the most energetic crystal in the SC. Much like $\sigma_{i\eta i\eta}$, it is sensitive to the width of the shower shape. A regression to correct the energy scale [22] is trained as a function of SC energy, η , R_9 , and the width of the SC in ϕ . Differences between data and MC in the efficiencies of the electron and photon IDs are corrected using scale factors using $Z \rightarrow ee$ events, as was described for muon IDs. In the case of the photon ID, the electron SC is used as a proxy for the photon.

Jets

Hadronic taus

Missing momentum

1.4 Simulation of collisions

1.4.1 Physics simulation

1.4.2 Detector simulation

Chapter 2

Hadronic Resonance Identification

In this chapter, we describe the reconstruction and identification of heavy ($\gtrsim 100$ GeV) resonances that decay to two or more quarks. Within the Standard Model, the only such resonances are the massive vector bosons ($W, Z \rightarrow q\bar{q}'$), the Higgs boson (typically $H \rightarrow b\bar{b}$), and the top quark ($t \rightarrow bW(\rightarrow q\bar{q}')$). These quarks hadronize into jets (described in Chapter ??), which are typically reconstructed at the LHC using the anti- k_T algorithm (described in Chapter 1.3). The focus of this chapter is on the cases in which the resonance is boosted and the decay products merge, such that they cannot be identified as 2 or 3 distinct jets. In preparation for Chapter 3, we will take the top quark as a concrete example. The studies presented here can (and in some cases have been) applied to other heavy resonances, both within and beyond the Standard Model.

2.1 Reconstruction

The approximate angular separation between the quarks from a heavy resonance decay is[??]:

$$\Delta R \sim \frac{2M}{p_T} \tag{2.1}$$

where M is the resonance mass and p_T is the resonance transverse momentum. Setting $M = m_t$ and $\Delta R = 1.2$ (i.e. the radius at which three $R = 0.4$ jets start to overlap), we

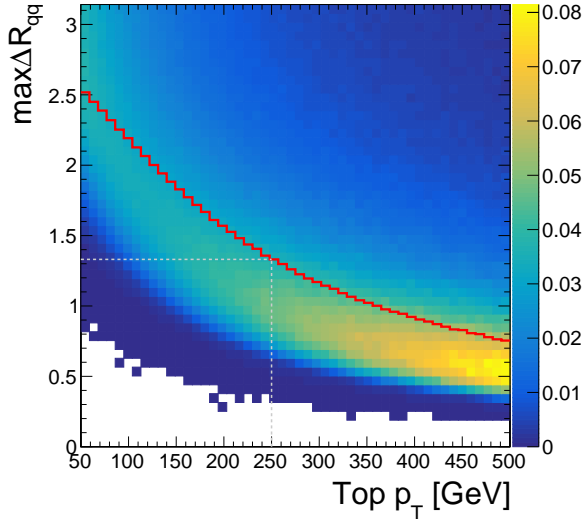


Figure 2.1: Distribution of top quark momenta versus decay radii in a simulated top quark pair sample. The events are weighted such that the inclusive momentum distribution is uniform. The z -axis units are arbitrary, but proportional to the distribution of jets. The solid red line marks the 50% quantile of jets at each value of p_T .

extract a “merging scale” of 300 GeV. This is be verified by checking the distribution of the “decay radius” in top quark simulation. Here, we define decay radius as:

$$\max \Delta R_{qq} \equiv \max_{0 \leq i < j \leq 2} \{\Delta R(q_i, q_j)\}, \text{ where } t \rightarrow q_0 q_1 q_2 \quad (2.2)$$

Using a broad spectrum of generated top quark p_T , Figure 2.1 shows the dependence of the decay radius on the top quark p_T , where we restrict the resonance to satisfy $|\eta| < 2.5$. If we are interested in top quarks with $p_T > 250$ GeV (motivated by the trigger selection (Section 3.1)), then over half of top quarks will be fully contained within a jet of radius 1.5. That is, at $p_T \approx 250$ GeV, it is equally likely that a top quark’s decay products will fall within a single large-radius jet or that they will be resolvable as three separate jets. However, past this threshold momentum, the large-radius jet becomes the preferred reconstruction option. This motivates the use of $R = 1.5$ jets to reconstruct hadronic top quarks with $p_T > 250$ GeV.

There are two tunable parameters in jet reconstruction. We have specified the jet radius, but we must also choose the jet algorithm. The anti- k_T algorithm tends

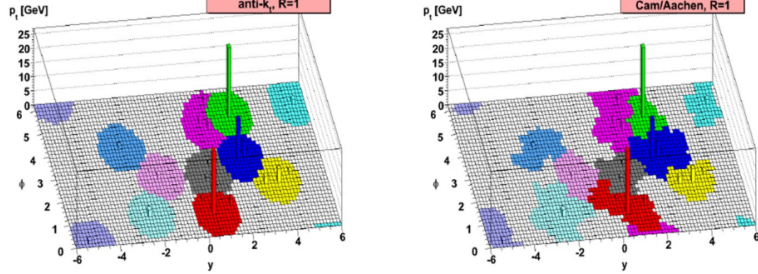


Figure 2.2: Jets clustered using the anti- k_T (left) and CA (right) algorithms. Shown is the y - ϕ plane of a hypothetical calorimeter, unrolled onto a flat surface. The height of each cell represents the p_T of the particle. The anti- k_T jets tend to be more circular when compared to the CA jets. Figures are adapted from [??].

to pick circular jets, whereas the Cambridge-Aachen (CA) algorithm allows for more geometric shapes (Figure 2.2). As the top jets we seek to reconstruct are the sum of three light quark jets, we do not necessarily expect the $R = 1.5$ jet to be circular. Figure 2.3 compares the jet mass distribution for top and light quark/gluon (LQG) jets, where the jets are clustered using both algorithms. CA produces a top jet mass distribution with a narrower peak that sits closer to m_t than anti- k_T . Because of this, and the general improvement in S/B near the top mass peak, we choose the CA algorithm. Hereafter, we will refer to Cambridge-Aachen $R = 1.5$ jets as CA15 jets.

The distance parameter of $R = 1.5$ corresponds approximately to a maximal azimuthal angle separation of $\pi/2$, which can cover half of the detector’s fiducial volume. As the jet is so large, particles from pile-up interactions may accidentally be clustered into a jet from the primary vertex. Fundamental quantities (like top quark momentum) are uncorrelated with the number of primary vertices (N_{PV}), but reconstructed quantities acquire such a dependence due to the extra radiation. These additional particles bias the energy scale of the jet (e.g. the mass) as well as geometric observables (described in Section 2.2). To mitigate these effects, we scale the particles’ 4-momenta by their corresponding PUPPI scores (described in Chapter 1) prior to clustering the jet. Jets clustered using all particles (without PUPPI filtering) have a jet mass and τ_{32}^{SD} distributions (Figure 2.4) in which both the mean and variance have an N_{PV} -dependence. Adding PUPPI stabilizes the mean and ensures that the

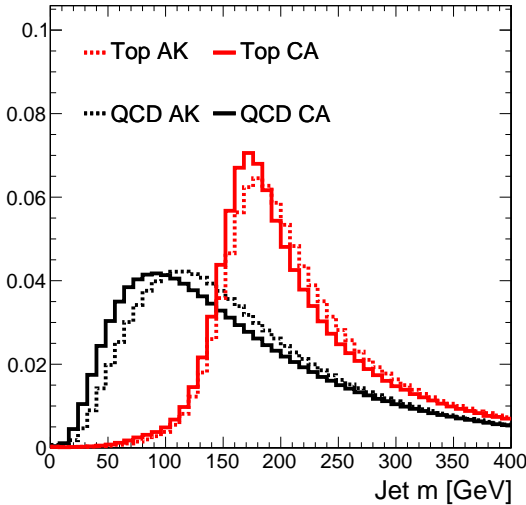


Figure 2.3: Mass distribution for jets clustered using the anti- k_T (dashed) and CA (solid) algorithms. QCD refers to jets originating in QCD multijet events, i.e. from the hadronization of light quarks or gluons.

variance does not grow at large N_{PV} .

2.2 Identification

Having *reconstructed* the candidate top quark jets, we turn to the problem of *identifying* which CA15 jets originate from top quarks as opposed to light q/g hadronization. As indicated in Figure 2.3, the jet mass is a powerful observable, but top (LQG) jets do not necessarily have a mass of m_t ($m_q, m_g \sim 0$). While some of this discrepancy is caused by mismeasurement of the jet energy scale (Chapter 1), a substantial fraction originates from extra radiation being absorbed into the jet. These extra particles arise from pile-up (although this is accounted for by PUPPI), initial state radiation, and underlying event. Many algorithms exist to “groom” such particles from a jet after it has been clustered; here, we will discuss and use the soft drop (SD) method [??]. SD functions by traversing the CA clustering history (a binary tree) in reverse and removing subjets (i.e. branches) of the clustering tree that are deemed to be too soft or wide-angled. More formally, at each node in the clustering tree, the softer subjet

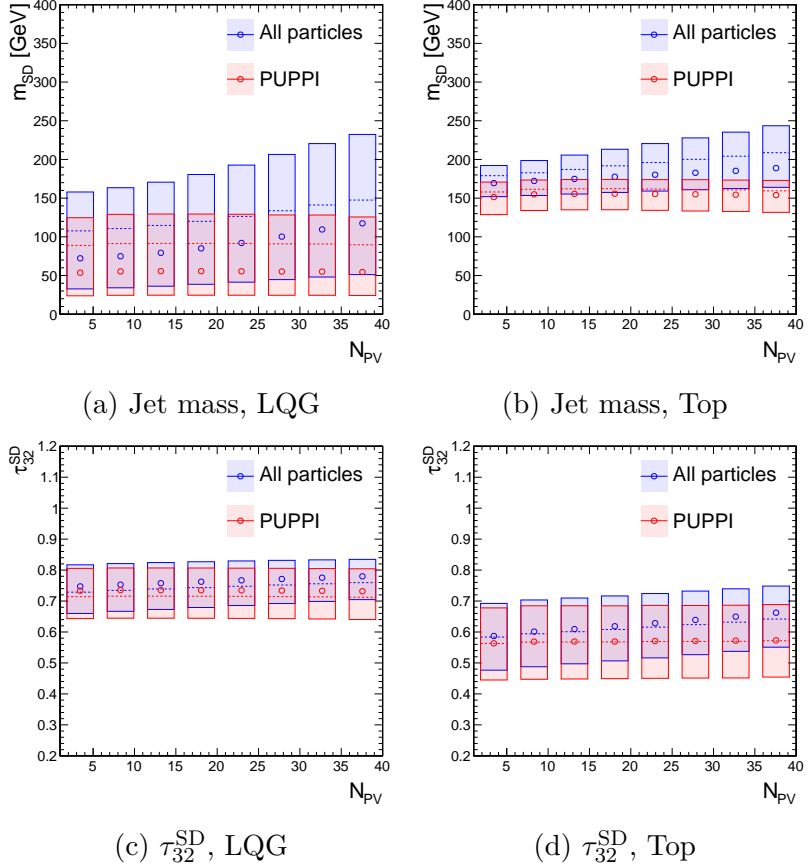


Figure 2.4: Stability of two CA15 jet observables (described in Section 2.2) as a function of N_{PV} . The median (mean) of each N_{PV} bin is represented by an open circle (dashed line), while the [25%, 75%] percentile range is shown with a box.

of the node will be removed if it satisfies the condition:

$$\frac{\min(p_{T,1}, p_{T,2})}{p_{T,1} + p_{T,2}} < \left(\frac{\Delta R_{12}}{R}\right)^\beta \quad (2.3)$$

where $p_{T,i}$ refers to the p_T of the i -th subjet of the node; ΔR_{12} is the ΔR -distance between the two subjet; and R and β are tunable parameters. This process starts at the root node of the clustering tree (i.e. the whole jet) and proceeds iteratively to the leaves (i.e. individual particles). This condition is satisfied if the two subjets are very far apart (assuming $\beta \geq 0$) or if the splitting is very asymmetric in momentum. We define the “SD subjets” (or where clear, simply “subjets”) of a jet to be the two branches of the root node, after branches failing the SD condition have been removed. The particles remaining after this grooming procedure are combined to make the “groomed” or SD jet.

We then define m_{SD} as the mass of the SD jet. Observables may also be defined in terms of the groomed or ungroomed jet. Figure 2.5 compares the ungroomed and groomed mass distributions in top and LQG jets, as a function of jet momentum. It is immediately clear that grooming provides (a) a sharper mass peak in top jets at m_t and (b) a smoothly falling mass distribution in LQG jets that goes to 0. Furthermore, SD ensures the stability of the mass distribution as a function of jet p_T , especially in LQG jets. For these reasons, m_{SD} will be our standard definition of jet mass.

2.2.1 Substructure

A substructure observable is any function of a jet’s constituents that is sensitive to the multi-pronged structure of a heavy resonance decay. In addition to jet mass and b -tagging, substructure is used to reject LQG jets as top decay candidates.

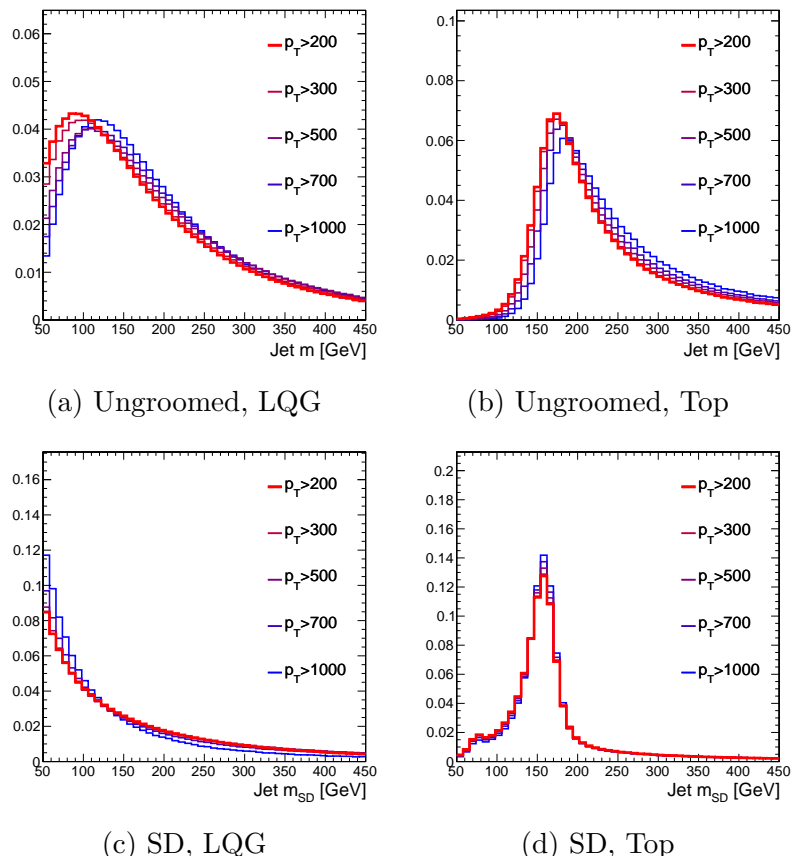


Figure 2.5: Distribution of ungroomed and groomed jet mass in CA15 jets originating from LQG or hadronic top decays. The multiple histograms represent increasingly stringent p_T requirements on the parton that initiates the jet.

N-subjettiness

The *N*-subjettiness (τ_N) is a measure of the compatibility of a jet with an *N*-axis hypothesis [??]. It is defined as:

$$\tau_N = \frac{\sum_{i \in \text{jet}} p_{T,i} \min\{\Delta R_{ia} | a \in A\}}{\sum_{i \in \text{jet}} p_{T,i} R} \quad (2.4)$$

where $R = 1.5$ (the jet radius); ΔR_{ia} is the ΔR distance between the particle i and the axis a ; and A is a set of N axes. Ideally, A would be defined to be the set of axes that minimize τ_N for each jet, but this minimization problem is computationally difficult. Instead, the exclusive k_T algorithm is used to partition the jet's constituents into N subjets (NB: these are not the SD subjets discussed above). Since the k_T distance metric is proportional to $\Delta R^2/R^2$, this approximates the ideal minimization. The set of axes A is taken to be the directions of the N k_T subjets. A small τ_N indicates a high degree of compatibility with the *N*-axis hypothesis. Therefore, we expect a 3-pronged (e.g. top) jet to satisfy $\tau_3 \ll \tau_2$, whereas a 1-pronged (e.g. LQG) jet should satisfy $\tau_3 \lesssim \tau_2$ (for optimal choice of A , $N > M \Rightarrow \tau_N \leq \tau_M$ for any jet). Correspondingly, we take $\tau_{32} \equiv \tau_3/\tau_2$ to be the tagging observable.

Figure 2.6 shows the distribution of τ_{32} . As with jet mass, we may calculate τ_{32} either on the whole jet or on the groomed (SD) jet. The discrimination between top and LQG jets is similar in both cases, but as Figure 2.6c demonstrates, τ_{32}^{SD} has the weaker correlation with m_{SD} in LQG jets. This feature will be critical to validate any tagger in data, as described in Section 2.3.

HEPTopTagger

The HEPTopTagger algorithm de-clusters the jet into many subjets and attempts to reconstruct the W and t decay products out of these subjets [??]. The computation of the tagging variable f_{rec} can be simplified into three steps (a more detailed description is found in the appendix of Reference [??]):

1. Compute subjets of the CA15 jet. This is done in a fashion similar to the SD subjets discussed above, but instead of taking the two subjets of the root node,

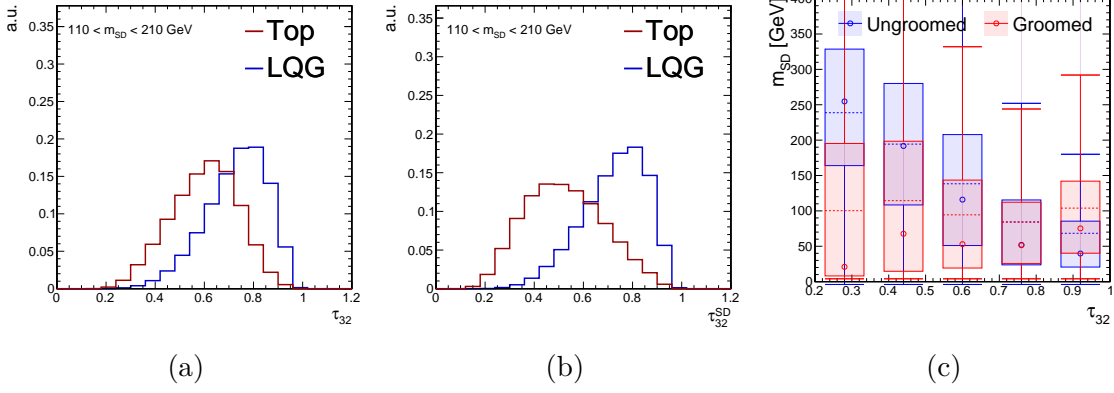


Figure 2.6: Shape of ungroomed (left) and groomed (center) τ_{32} distributions in top and LQG jets, with a mass selection consistent with m_t . Right: the correlation between τ_{32} and m_{SD} in LQG jets, comparing groomed and ungroomed jets.

the tree is traversed until some lower p_T bound is crossed.

2. Test all triplet combinations of the found subjets and define the m_{123} as the groomed mass of the trijet system.
3. Choosing the triplet most consistent with a 3-body top decay (see Equation 12 in Reference [???]), define:

$$f_{\text{rec}} = \min_{0 \leq i < j \leq 2} \left| \frac{m_{ij}/m_{123}}{m_W/m_t} - 1 \right| \quad (2.5)$$

where the indices i, j index elements of the selected triplet.

Figure 2.7 shows the distribution of the selected m_{123} and f_{rec} , although we will only use the latter as a tagging observable. Note that we do not define distinct groomed and ungroomed versions of these observables, as grooming is intrinsically used in defining the subjets.

Energy Correlation Functions

Energy correlation functions measure the correlation of the positions of hard particles in a jet [??]. Heuristically, an N -point ECF is small if the hard particles can be grouped into fewer than N prongs and large if they arise from N or more prongs. An

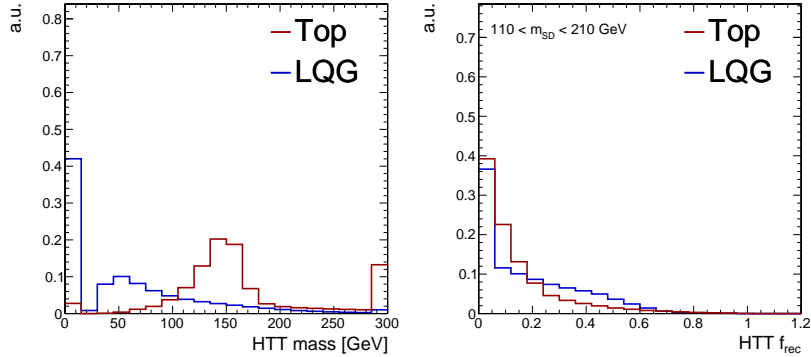


Figure 2.7: Shape of the m_{123} and f_{rec} observables computed by the HEPTopTagger algorithm.

N -point ECF, with angular parameters α and β , is defined as:

$$e(\alpha, N, \beta) \equiv {}_N e_N^\beta = \sum_{K \subset J, |K|=N} \left[\prod_{i \in K} \frac{p_T^{(i)}}{p_T^{(J)}} \right] \times \min \left\{ \prod_{i,j \in P} \Delta R_{ij}^\beta \mid P \subset (K^2 \setminus (k, k)), |P| = \alpha \right\} \quad (2.6)$$

where $K^2 \setminus (k, k)$ indicates all pairs of distinct particles in K . The proposed tagger in Reference [??] is:

$$N_3^{(\beta)} = \frac{e(2, 4, \beta)}{(e(1, 3, \beta))^2} \quad (2.7)$$

Figure 2.8 shows N_3 for various values of β ; given our desire for stability as a function of jet p_T and mass, we only consider ECFs computed on the SD jet. The discrimination power of this ECF ratio is roughly comparable to that of τ_{32}^{SD} . N_3 is motivated by the behavior of 3- and 4-point ECFs in top and LQG jets:

- In top jets, $e(N=4) \ll e(N=3)$, since 3-point correlation functions are large in a 3-pronged jet
- In QCD jets, $e(N=3) \sim e(N=4)$, since both 3- and 4-point ECFs are weak in a 1-pronged jet

Therefore, taking the ratio $e(N=4)/e(N=3)$ constructs a useful observable.

While N_3 has a strong theoretical motivation, it is possible that other functions of ECFs distinguish between top and LQG jets. In order to construct observables that

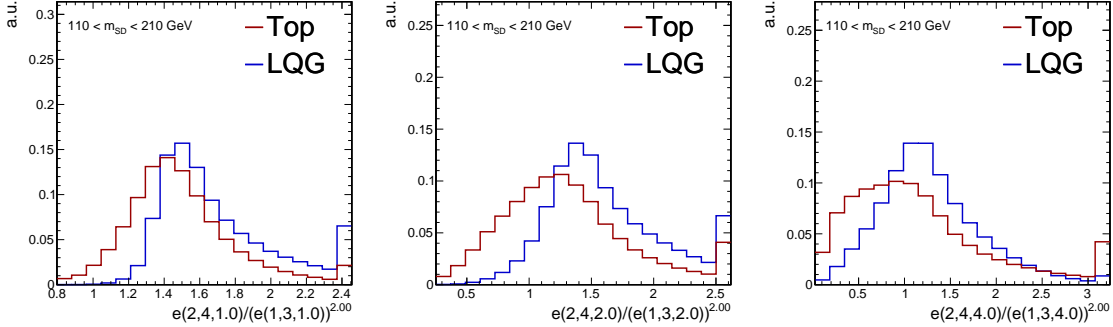


Figure 2.8: Shape of the N_3 observables in top and LQG jets, for various values of β .

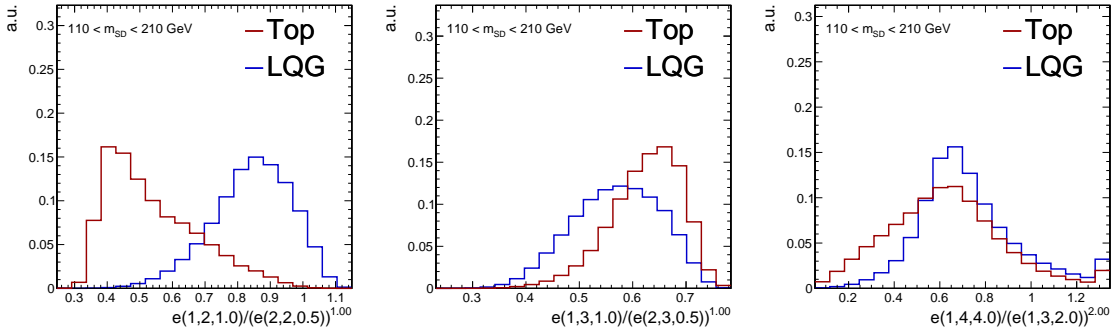


Figure 2.9: Examples of non-trivial ECF ratios other than N_3 that separate top and LQG jet distributions.

do not have a strong dependence on the jet p_T , we restrict ourselves to ratios of the form:

$$\psi(a, N, \alpha, b, M, \beta) = \frac{e(a, N, \alpha)}{(e(b, M, \beta))^x}, \text{ where } M \leq N \text{ and } x = \frac{a\alpha}{b\beta} \quad (2.8)$$

A large subset of this broader class of ECF observables are found to be useful (Figure 2.9), including ratios not of the form $e(N = 4)/e(N = 3)$.

2.2.2 A combined tagger

In principle, we have constructed an infinitely large space of substructure observables.

In practice, we only consider a finite sampling of ECF parameters:

$$\begin{aligned} N &\in \{1, 2, 3, 4\} \\ o &\in \{1, 2, 3\} \\ \beta &\in \{0.5, 1, 2, 4\} \end{aligned} \tag{2.9}$$

This grid results in ~ 900 ψ observables.

To build a single optimal observable out of all the $\{\psi_i\}$ s, we will use a boosted decision tree (BDT). A simplified algorithm to train a single decision tree node n is as follows:

1. Choose a ψ_j , either by sampling randomly or selecting the one most optimal for the next step.
2. Based on the training data fed to the node, select a decision boundary d_n to optimize a loss function. For example, one can use the cross-entropy loss:

$$\ell(X, y; j, d_n) = -\hat{\pi}_B \ln \hat{\pi}_B - \hat{\pi}_S \ln \hat{\pi}_S, \text{ where } \hat{\pi}_c = \hat{P}(y = c | \psi_j < d_n) \tag{2.10}$$

A tree is built iteratively:

1. Train a node n using the above criteria.
2. If a stopping condition is not met (i.e. maximum number of nodes, minimal improvement in $\ell(n)$), train one node on the samples that pass n and another on the samples that fail.

Figure 2.10 provides a pictorial example of how a decision tree can be built.

While decision trees can very accurately describe training data provided sufficient complexity, they also pathologically overfit the data. To mitigate this, while retaining descriptive power, a standard method is to *boost* many simple trees. The simplicity of

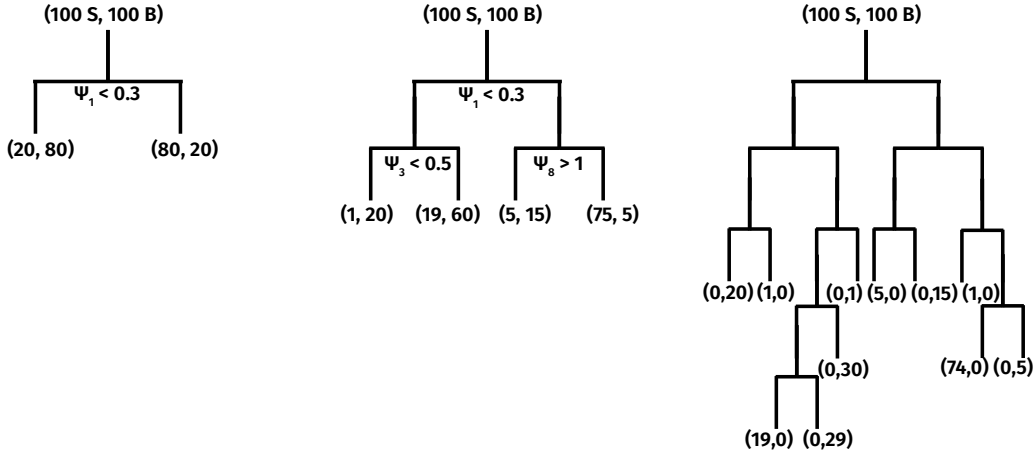


Figure 2.10: Steps in greedily training a simple decision tree.

the tree prevents overfitting, while boosting many trees allows for a complex model. The result of a BDT is a classifier $f_n(x) = \sum_{i=0}^n \nu^i T_i(x)$, where $\nu \leq 1$ is tunable and each T_i is a decision tree. A simplified algorithm to train a BDT is as follows:

1. Define a global loss function, e.g.:

$$L(y_i; f_i) = \ln(1 + \exp(-y_i f_i)) \quad (2.11)$$

2. Train a single tree T_0 and initialize classifier $f_0 = T_0$

3. Until some stopping condition (index $m = 1, \dots$):

- 3.1. Compute the “residual”

$$r_{mi} = -\nabla_f L(y_i; f)|_{f=f_{m-1}(\psi_i)} \quad (2.12)$$

$$L = (y - f_m(\psi))^2 \Rightarrow r_m = y - f_m(\psi) \quad (2.13)$$

- 3.2. Fit a regression tree T_m to predict r_{mi} as a function of x_i :

$$\ell(X, r_m; j, d, \hat{r}) = \sum_{i|\psi_{ji} < d} (r_{mi} - \hat{r})^2 \quad (2.14)$$

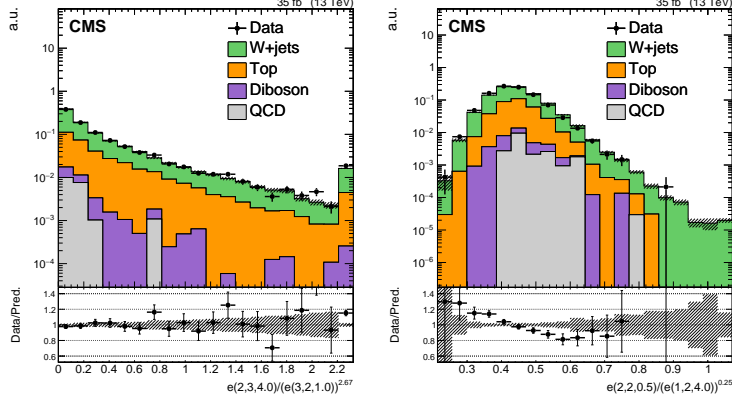


Figure 2.11: Two different ECF ratios in a W +jets selection, heavily enriched in LQG jets. One is fairly well-modeled, while the other is not.

3.3. Update $f_m = f_{m-1} + \nu T_m$

While we would like to train a BDT on the entire space of $\{\psi\}$, there are two issues to be solved: poorly modeled ratios and a large feature space. Firstly, not every ECF ratio is well-simulated by our MC (Figure 2.11). More systematically, we can compute the CDFs of each ψ and define a score:

$$-\log_{10} \text{KS}(F(\psi_i|\text{data}), F(\psi_i|\text{MC})) = -\log_{10} \max |F(\psi_i|\text{data}) - F(\psi_i|\text{MC})| \quad (2.15)$$

where F represents the CDF and KS denotes the Kolmogorov-Smirnov metric on probability distributions. The score is close to 0 for poorly-simulated distributions. Figure 2.12 parameterizes this as a function of N/M (ratio of the number of particles) and $a\alpha/b\beta$ (ratio of the angular powers) and shows an interesting structure. It is found that $3/2$ and $4/2$ ratios are uniformly poorly modeled, as are ratios with large $a\alpha/b\beta$. While this structure is interesting and suggestive, we do not yet understand its origin, and therefore do not use this parameterization to select ECF ratios. Instead, we simply reject any ECF ratio for which $-\log_{10} \text{KS} < 1$.

Even after filtering poorly-modeled ratios, we are left with a sampled ψ grid of ~ 400 points. By inspection, many of the ψ s are highly correlated or not useful at all. It is desirable to reduce the size of the feature space, as computing each ECF is somewhat

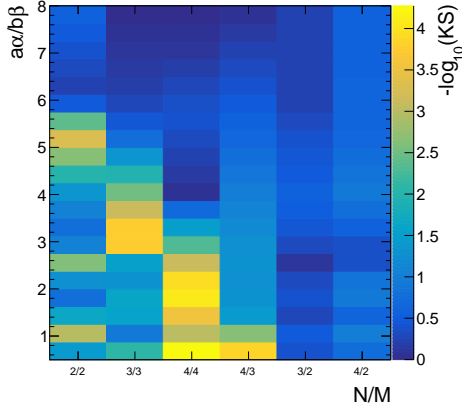


Figure 2.12: The $-\log_{10}$ KS metric as a function of N/M and $a\alpha/b\beta$, computed using events enriched in LQG jets.

computationally-intensive: an N -point ECF on a p -particle jet has $\binom{N}{p}$ terms. Note that standard pre-processing techniques, like principal component analysis, do not reduce the number of features to be computed. While L1 regularization does attempt such a dimensional reduction, it cannot be trivially applied to BDTs. Therefore, we introduce a targeted iterative training method to solve this problem:

1. Train a BDT with trees T_1, \dots, T_n
2. For each ψ_i , define a score:

$$s_i = \sum_{m=1}^n \nu^{m-1} \sum_{\text{nodes using } \psi_i \text{ in } T_m} N_{\text{samples}}(\text{node}) \times (\ell(\text{node}) - \ell(\text{parent}))^2 \quad (2.16)$$

3. Remove (one or more) ψ_i with smallest s_i and repeat until the global loss L worsens significantly

Iterative training is expensive and can require the training of $\mathcal{O}(50)$ BDTs. It is semi-parallelizable, and the entire process typically takes a few hours. However, as the inference samples are 1-2 orders of magnitude larger than the training samples, this method reduces the total CPU time needed to run an analysis. Figure 2.13 shows background acceptance rate at $\epsilon_{\text{sig}} = 0.5$ (a proxy for the global loss) as a function of feature space size. For illustrative purposes, we only show the range [1, 50]. The

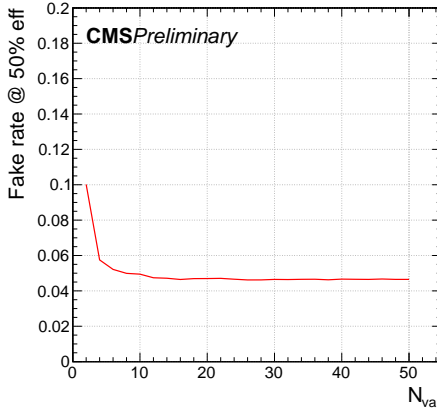


Figure 2.13: Performance of BDTs as a function of the number features used in the training.

inputs for this training are the ECF ratios, as well as τ_{32}^{SD} and f_{rec} , which provide additional information. It is clear that beyond 13-15 features, there is little to be gained by adding additional information.

The features selected by this reduction and classification process are:

$$\begin{aligned}
 & \frac{e(1, 4, 20)}{e(1, 3, 10)^2}, \frac{e(1, 4, 40)}{e(1, 3, 20)^2}, \frac{e(2, 4, 05)}{e(1, 3, 05)^2}, \frac{e(2, 4, 10)}{e(1, 3, 10)^2}, \frac{e(2, 4, 10)}{e(2, 3, 05)^2}, \frac{e(2, 4, 20)}{e(1, 3, 20)^2} \\
 & \frac{e(1, 2, 20)}{e(1, 2, 10)^2}, \frac{e(1, 3, 40)}{e(2, 3, 20)}, \frac{e(3, 3, 10)}{e(1, 3, 40)^{3/4}}, \frac{e(3, 3, 10)}{e(2, 3, 20)^{3/4}}, \frac{e(3, 3, 20)}{e(3, 3, 40)^{1/2}} \\
 & \tau_{32}^{\text{SD}}, f_{\text{rec}}
 \end{aligned} \tag{2.17}$$

While a number of N_3 or other 4/3 ratios appear in this list, we find a number of 2/2 and 3/3 ratios to contribute meaningfully to the classification task as well. Figure ?? shows the distributions of all selected features. Figure ?? shows the background acceptance as a function of signal efficiency, comparing the final BDT (“Combined BDT”) to several other taggers. The “11 ECF” BDT refers to a BDT trained using only the 11 ECF ratios from Equation 2.17, indicating that τ_{32}^{SD} and f_{rec} are critical to achieving the same performance that can be reached with a much larger ECF ratio set (“50 ECF”). For comparison, also shown are the efficiency curves for τ_{32}^{SD} and a BDT trained using τ_{32}^{SD} and f_{rec} only. At fixed signal efficiency $\epsilon_{\text{sig}} = 0.5$, the combined

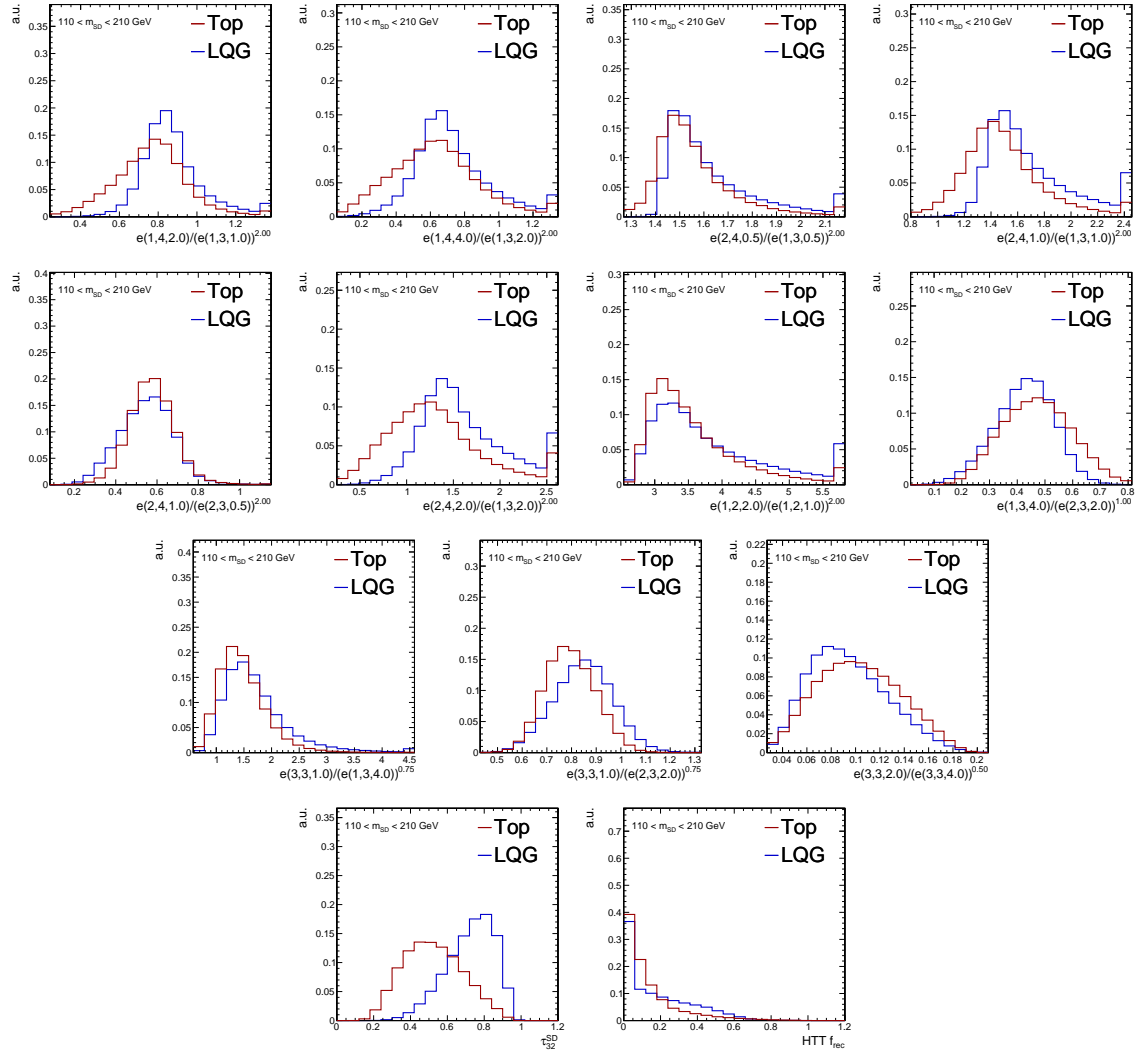


Figure 2.14: Distributions of the 13 features selected by the iterative BDT training

BDT reduces the background acceptance by 30% relative to τ_{32}^{SD} , the standard top ID criterion at the LHC prior to this study.

2.3 Data validation

Prior to using the top BDT to identify top jets and reject LQG jets, we must verify that the simulation describes the BDT distribution properly as compared to data, and correct for any residual discrepancies. Figure 2.16 shows the BDT response and m_{SD} in top- and LQG-enriched selections. Top quarks are isolated by selecting events

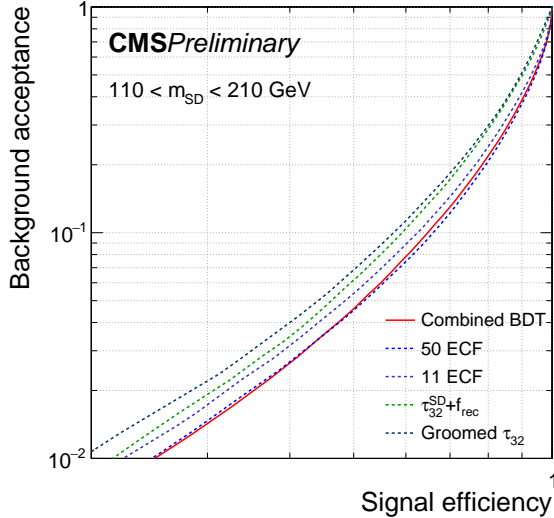


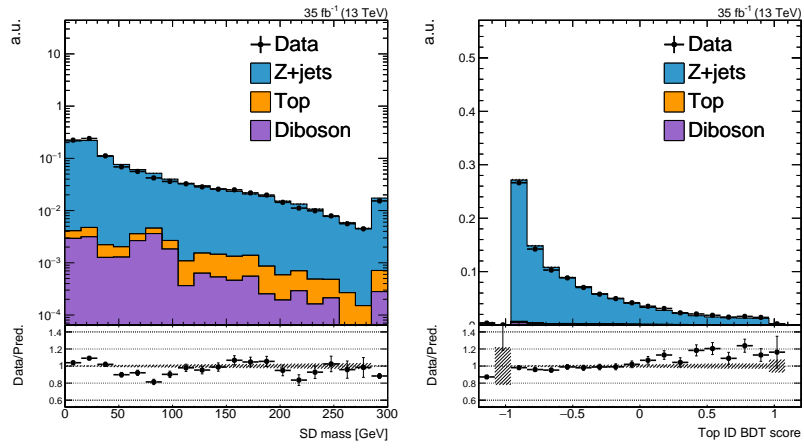
Figure 2.15: Receiver Operating Characteristic (ROC) curve comparing various top identification methods. The “Combined BDT” is the ID method chosen as the final tagger.

that produce $t\bar{t}$ pairs, in which one top quark decays hadronically (the top jet) and the other decays muonically ($t \rightarrow b\mu^+\nu_m u$). The leptonic t is selected by identifying the muon and b jet. We further require that the CA15 jet have $110 < m_{\text{SD}} < 210$ GeV and at least one SD subjet to be b -tagged. LQG jets are selected by using $Z(\rightarrow \mu\mu) + \text{jet}$ events. We require two opposite sign muons, with $|m_{\mu\mu} - m_Z| < 30$ GeV; this selection selects a $\gtrsim 95\%$ pure $Z + \text{jet}$ sample. In both samples, we observe reasonably good agreement between data and simulation.

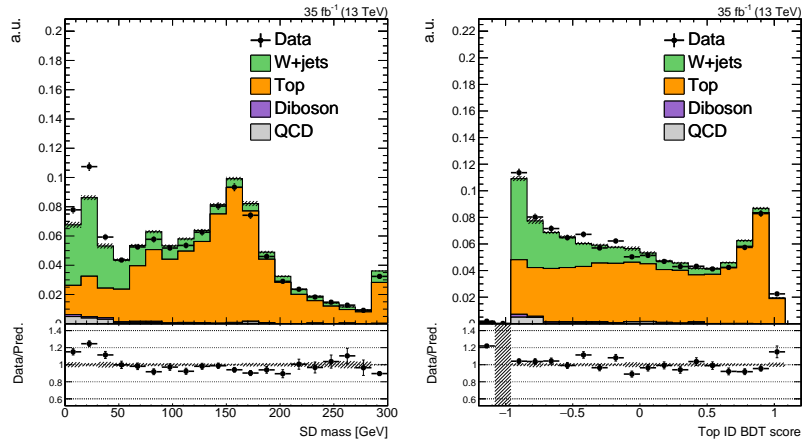
To account for any remaining differences, we define a scale factor (SF):

$$\text{SF}(x) = \frac{\epsilon_{\text{Data}}(\text{BDT} > x \text{ and } 110 < m_{\text{SD}} < 210)}{\epsilon_{\text{MC}}(\text{BDT} > x \text{ and } 110 < m_{\text{SD}} < 210)} \quad (2.18)$$

where x is a particular decision boundary and ϵ is the fraction of data or MC events passing this BDT and mass selection. These are chosen to optimize sensitivity to the mono-top analysis, as described in Chapter 3. The SF is strongly dependent on the type of jet; in particular, we expect different SFs for top and LQG jets. In what follows, we will define two decision boundaries: a loose (0.1) and a tight (0.45)



(a) Dimuon selection



(b) $t\bar{t}$ selection

Figure 2.16: Comparison of the BDT response and jet mass in data and simulation, in top and LQG jets.

category.

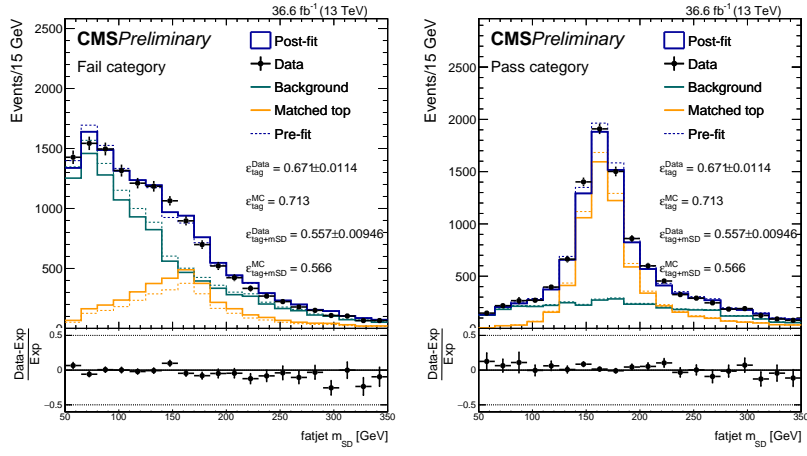
To compute SF_{LQG} , we use the dimuon selection in Figure 2.16, as this contains an essentially pure selection of LQG jets. Two sources of uncertainty are considered: the statistical uncertainties present in the data and MC, and the uncertainties on the theoretical prediction of the cross section of the small non-LQG backgrounds ($t\bar{t}$ and diboson events). The measured SFs are:

$$\begin{aligned} SF_{LQG}(0.1) &= 1.02 \pm 0.05(\text{total}) \\ &\quad \pm 0.04(\text{statistical}) \pm 0.03(t\bar{t} + \text{diboson}) \\ SF_{LQG}(0.45) &= 0.97 \pm 0.07(\text{total}) \\ &\quad \pm 0.06(\text{statistical}) \pm 0.03(t\bar{t} + \text{diboson}) \end{aligned} \quad (2.19)$$

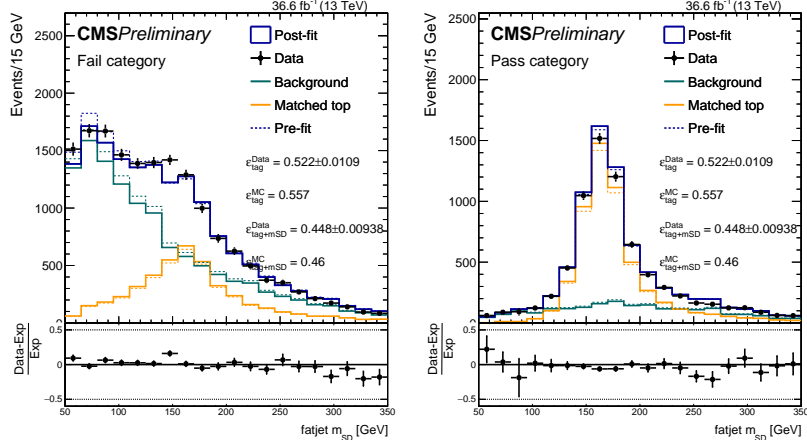
The process for top jets is complicated by the fact that the top pair selection in Figure 2.16 is not sufficiently pure in merged top jets. There is significant contamination from $W+jets$ events. Furthermore, we cannot ensure that every $t\bar{t}$ event selected produces a *merged* top jet - some events may contain jets in which only part of the top's decay products are clustered into the CA15 jet. Therefore, we extract the efficiency by means of a template fit to the mass distribution of passing and failing events, which can separate the top and LQG components in the selection. It is for this reason that we only use groomed observables in the BDT: grooming prevents a strong correlation between the observables and m_{SD} . Such a correlation would cause the mass distribution of passing LQG jets to be indistinguishable from that of passing top jets. Figure 2.17 show the fits in the passing and failing regions for both decision boundaries.

Several sources of uncertainty are considered for this measurement:

- Poisson uncertainties in the data and simulation
- CA15 jet energy scale and resolution
- Definition used to select “merged top” jets, allowing $\max \Delta R_{qq'}$ to vary between 1 and 1.5 (nominal value is 1.2)



(a) Loose BDT-tagged



(b) Tight BDT-tagged

Figure 2.17: Fits to the m_{SD} distribution in a $t\bar{t}$ sample to extract the efficiency in data of the BDT and mass selections. All uncertainties plotted and quoted are statistical in nature.

- Efficiency of selecting b jets

The resultant SFs and associated uncertainties are:

$$\begin{aligned}
 \text{SF}_{\text{top}}(0.1) &= 1.08 \pm 0.04(\text{total}) \\
 &\quad \pm 0.03(\text{statistical}) \pm 0.02(\text{JES} + \text{JER}) \pm 0.02(\text{merging}) \pm 0.002(b) \\
 \text{SF}_{\text{top}}(0.45) &= 1.07 \pm 0.06(\text{total}) \\
 &\quad \pm 0.03(\text{statistical}) \pm 0.02(\text{JES} + \text{JER}) \pm 0.014(\text{merging}) \pm 0.000(b)
 \end{aligned} \tag{2.20}$$

Chapter 3

The Search for $t + p_T^{\text{miss}}$

In this chapter, we discuss the search for dark matter produced in association with a single top quark (“mono-top”). Since the initial state of pp collisions do not contain any appreciable contribution from top quarks, any process that produces a single top quark must involve some flavor violation. In the Standard Model, any such process is heavily suppressed by off-diagonal elements of the CKM matrix. The SM production mechanism for the mono-top signature (Figure 3.1) involves a b quark in the final state, and thus does not couple the third generation with the first or second. True production of mono-top must introduce some such coupling as an extension to the SM, in addition to one (or more) invisible particle to serve as a DM candidate.

To illustrate how beyond-SM physics can produce this final state, we introduce two DM models: a flavor-changing neutral current V and a charged, colored scalar ϕ . These models will also be used to benchmark the sensitivity of the analysis. However, it should be emphasized that the search is motivated and designed without reliance on any specific model; the assumption is that the mono-top final state alone is indicative of new physics, regardless of the specific production mechanism.

The FCNC V is assumed to couple to a fermionic DM candidate χ . A partial Lagrangian of the interaction terms is given by:

$$\mathcal{L}_{\text{int}} = V_\mu \bar{\chi} \gamma^\mu (g_\chi^V + g_\chi^A \gamma_5) \chi + \bar{q}_u \gamma^\mu (g_u^V + g_u^A \gamma_5) q_u V_\mu + \bar{q}_d \gamma^\mu (g_d^V + g_d^A \gamma_5) q_d V_\mu + \text{h.c.}, \quad (3.1)$$

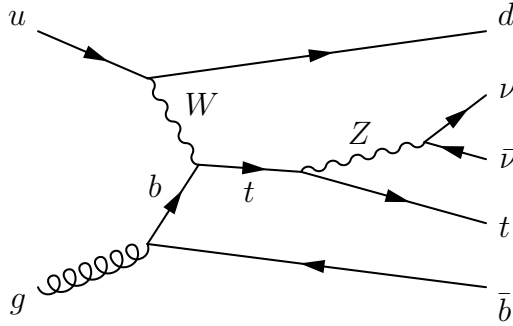


Figure 3.1: Production of mono-top in the SM, in which a top quark is produced in addition to a Z boson and bottom quark. The Z decays to neutrinos, providing large p_T^{miss} .

The model comes with 22 free parameters, broadly organized in three sets:

- The masses m_V and m_χ . (2)
- The couplings g_χ^V and g_χ^A . These, respectively, control the strength of the vector and axial interactions between V and χ . (2)
- The four coupling matrices g_q^X , where $q = u, d$ and $X = V, A$. As before, X determines the type of spin-1 interaction. In principle, different coupling strengths can be permitted for up- and down-type quarks, so this indexed by q . Each g_q^X is a 3×3 matrix, cross-coupling the three quark generations. To preserve $SU(2)_L$ symmetry, we require $g_u^V - g_u^A = g_d^V - g_d^A$. ($3 \times 6 = 18$)

It is the $g_{u,d}^{V,A}$ matrices that determine whether the model can produce mono-top, or mono-bottom, or mono-up, etc. If $g_{u,d}$ is strongly diagonal (i.e. strongest couplings are within generations), then mono-light quark production will dominate, resulting in the mono-jet final state (Figure 3.2a). On the other hand, if we assume the only non-zero elements are those that couple the first and third generations, then mono-top production at the LHC is the best way to probe this model (Figure 3.2b). It is this latter choice that will be made in the rest of this chapter; other choices are best probed using a combination of multiple DM channels, which is left as future work. Furthermore, to respect $SU(2)_L$ symmetry, we make the assumption that $g_u^V = g_d^V$ and $g_u^A = g_d^A$.

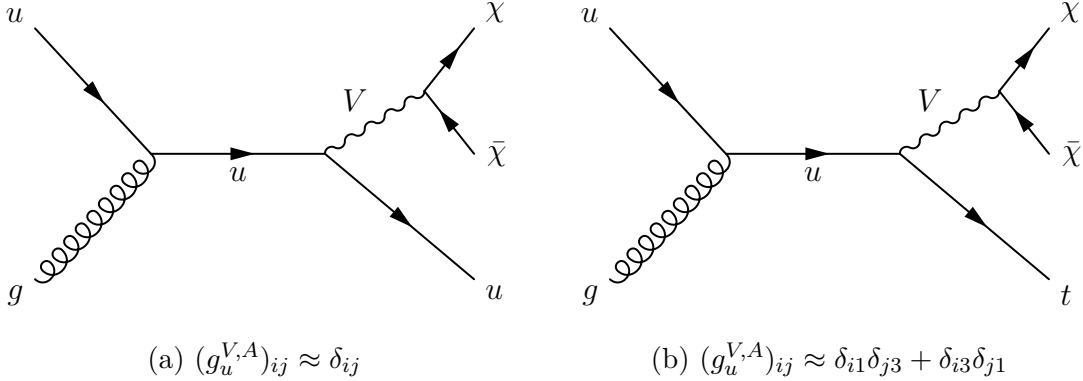


Figure 3.2: Possible DM production at the LHC, assuming a simplified spin-1 extension to the SM.

In the second benchmark model, the charged, colored scalar ϕ couples to down-type quarks, or to a fermionic DM candidate ψ and a top quark. The interaction terms of the Lagrangian is given by:

$$\mathcal{L}_{\text{int}} = \phi \bar{d}_i^C [(a_q)^{ij} + (b_q)^{ij} \gamma^5] d_j + \phi \bar{t} [a_\psi + b_\psi \gamma^5] \psi + \text{h.c.} \quad (3.2)$$

There are 16 free parameters in this model, broadly organized in three categories:

- The masses m_ϕ and m_ψ . (2)
- The couplings at the $\phi \bar{t} \psi$ vertex a_ψ and b_ψ , which respectively control the strength of the scalar and pseudoscalar interactions. (2)
- The couplings at the $\phi \bar{d}_i d_j$ vertex a_q^{ij} and b_q^{ij} where $i, j = 1, 2, 3$. Again, a and b refer the scalar and pseudoscalar couplings, respectively. (12)

In this model, mono-top production primarily occurs through the resonant decay of ϕ to ψ and t , as shown in Figure 3.3.

The two benchmark models show markedly different spectra in Figure 3.4, motivating their use to test different modes of mono-top production. The FCNC produces a falling p_T^{miss} distribution, whereas the scalar resonance produces a p_T^{miss} distribution peaking at approximately $m_\phi/2$.

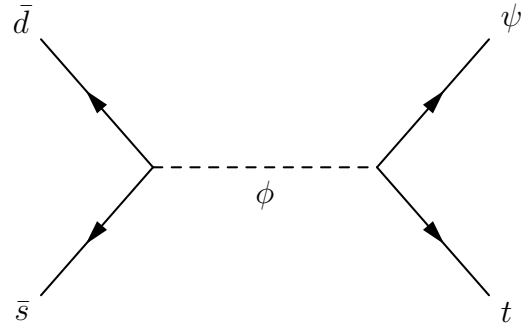


Figure 3.3: Possible DM production at the LHC, assuming the existence of a charged, color scalar that couples to DM and the top quark.

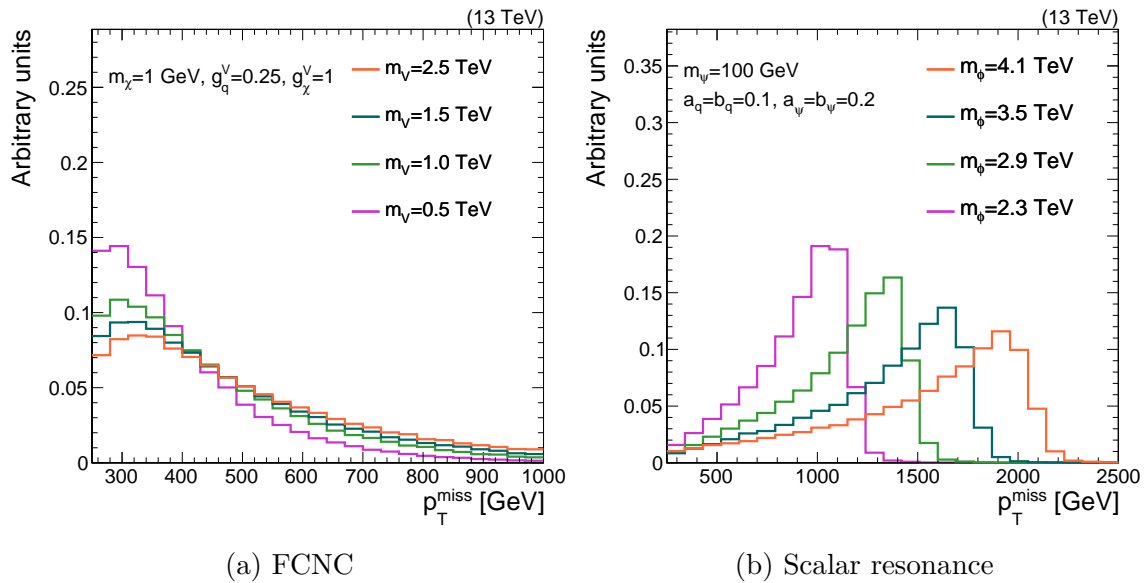


Figure 3.4: Spectra of DM (missing) momentum under various signal hypothesis.

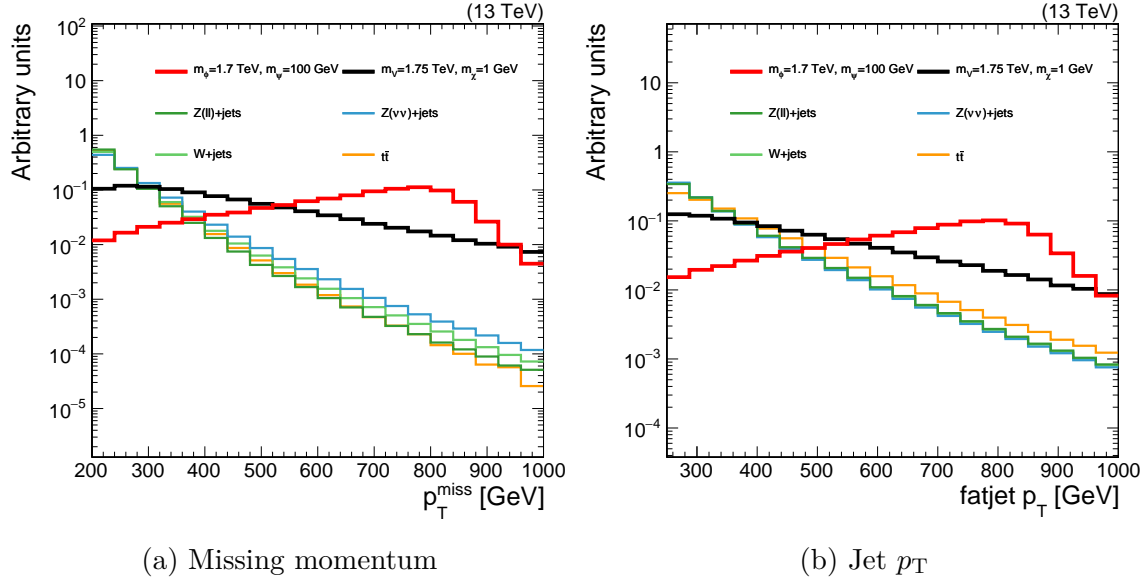


Figure 3.5: Comparison of missing and jet momenta in various backgrounds and signal models.

3.1 Signal selection

When looking at events that pass a simple set of criteria (moderate p_T^{miss} and one CA15 jet), it is clear (Figure 3.5) that the highest signal sensitivity is found in regions of high p_T^{miss} and jet p_T . The three primary background processes are:

- $Z \rightarrow \nu\nu$. When the Z is produced in association with one or more jets, the jet system can (with low probability) pass the criteria used to select a top jet. The neutrinos manifest as p_T^{miss} .
- $W \rightarrow \ell\nu$. As in the case of the Z , additional jets can mimic the signature of a top jet. Typically, the charged lepton in the final state is vetoed, but if it is out of acceptance (e, μ) or fails ID criteria (τ_h), then it is not identified.
- $t\bar{t} \rightarrow b\bar{q}\bar{q}' + \bar{b}\ell\nu$. As in the case of the W , a charged lepton in the final state may not be properly identified. Unlike the previous two processes, a semi-leptonic $t\bar{t}$ event contains a real hadronic top quark decay.

3.1.1 Online trigger selection

Data events are first selected by the L1 trigger system by requiring $p_{T,L1}^{\text{miss}} > 70 \text{ GeV}$, where:

$$p_{T,L1}^{\text{miss}} = - \left(\sum_{i \in C} \vec{p}_i \right)_T, \quad C = \{\text{calorimeter deposits with } |\eta| < 3.0\} \quad (3.3)$$

Events that pass this selection are sent to the HLT system, where we place requirements on the both the missing momentum ($p_{T,\text{HLT}}^{\text{miss}}$) and the missing hadronic momentum ($H_{T,\text{HLT}}^{\text{miss}}$). These are defined as:

$$p_{T,\text{HLT}}^{\text{miss}} = - \left(\sum_{i \in \text{particles}} \vec{p}_i \right)_T, \quad \text{all particles except muons} \quad (3.4)$$

$$H_{T,\text{HLT}}^{\text{miss}} = - \left(\sum_{i \in \text{jets}} \vec{p}_i \right)_T, \quad \text{jets passing noise-rejection ID} \quad (3.5)$$

The HLT decides to keep an event if $\min(p_{T,\text{HLT}}^{\text{miss}}, H_{T,\text{HLT}}^{\text{miss}})$ is higher than a specified threshold. Over the course of the data-taking period considered in this chapter, this threshold varied from 90 to 120 GeV.

Note that in all of the trigger decisions, muons are implicitly (in the L1) or explicitly (in the HLT) excluded from the missing momentum calculations. This means that an event which produces high-momentum muons can be selected using these triggers. This flexibility will be exploited in Section 3.2.

Since the online environment and reconstruction are significantly limited as compared to the offline reconstruction of U , we do not expect the trigger decision to be a step function at $U = 120 \text{ GeV}$. Therefore, we define and measure a trigger efficiency:

$$\epsilon_{\text{trig}}(U) = \frac{N_{\text{pass trig}}(U)}{N(U)} \quad (3.6)$$

This is measured using $W \rightarrow \mu\nu$ events containing one or more high- p_T jets. The events are triggered using single- μ triggers (which have lower thresholds and efficiencies ~ 1 in this phase space). We then require events have exactly one well-identified

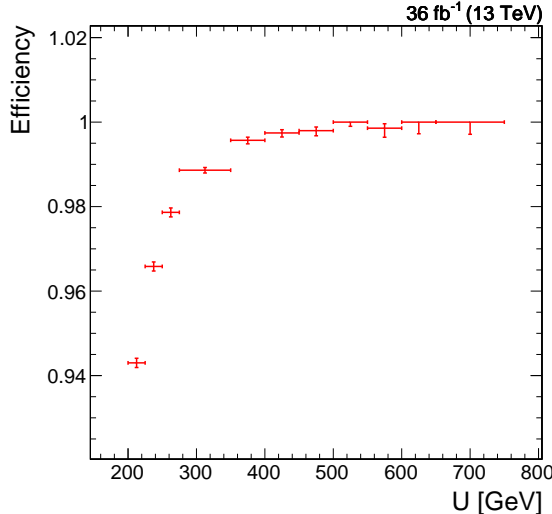


Figure 3.6: Efficiency of the p_T^{miss} trigger measured in single-muon events.

muon and at least one jet with $p_T > 100$ GeV. Figure 3.6 shows the efficiency as a function of U . To avoid the steeply-rising part of the curve, we choose a threshold of $U > 250$ GeV in the analysis.

3.1.2 Offline signal selection

Events in the signal regions (SRs) are then selected according to Table 3.1, chosen to be consistent with the signal topology while mitigating the aforementioned SM backgrounds. As described in Section ??, two working points (WPs) are defined for the top ID BDT. The signal events (passing all other selection criteria) are partitioned into a “loose” SR and a “tight” SR on the basis of which WP the top candidate jet satisfies.

Figure 3.7 shows the p_T^{miss} distributions, as predicted by MC and as observed in collected data, in the two signal regions.

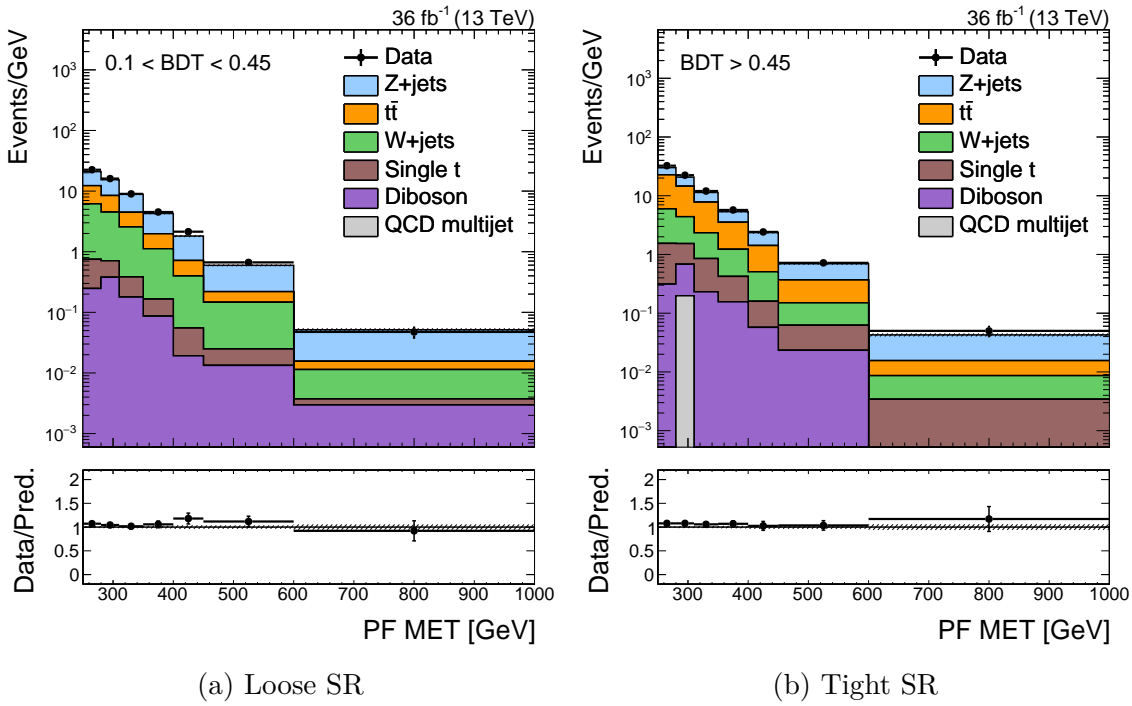


Figure 3.7: p_T^{miss} distributions in the two mono-top signal regions. The bottom section of each figure shows the ratio of the data and the prediction. The only uncertainties plotted in these figures are those arising from Poisson fluctuations in data (black bars) and MC (grey band).

Table 3.1: Criteria used to select events for the mono-top search signal regions. Note that two SRs are defined, based on the BDT score.

Criterion	Notes
$p_T^{\text{miss}} > 250 \text{ GeV}$	Signal events should have large missing momentum. Exact threshold is chosen to maximize online trigger efficiency.
1 CA15 jet with $p_T > 250 \text{ GeV}$	Top quark candidate. Recoils against p_T^{miss} , so threshold is set at 250 GeV.
CA15 jet $110 < m_{\text{SD}} < 210 \text{ GeV}$	Consistency with top quark mass.
At least one b -tagged sub-jet	Identifying B hadron produced from top decay/hadronization.
No b -tagged narrow jets	Rejecting semi-leptonic $t\bar{t}$ decays.
No identified e, μ, τ_h	Suppress $W+\text{jet}$ and $t\bar{t}$ processes.
No identified γ	Suppress $\gamma+\text{jet}$ processes.
$\min_{\text{jets}} \Delta\phi(\text{jet}, p_T^{\text{miss}}) > 0.5$	Remove events with large p_T^{miss} caused by mismeasured jets.
CA15 jet BDT	Identifying top decay structure. If the jet passes the tight WP, it is placed in the “tight” SR. Otherwise, if it only passes the loose WP, it is placed in the “loose” SR.

3.2 Background estimation

Searching for DM amounts to looking for an excess of data events over the SM prediction at large values of p_T^{miss} . Therefore, the p_T^{miss} distribution of the three primary SM backgrounds described in Section 3.1 must be predicted with small uncertainty. The MC simulation provides a reasonable description of the data, but the theoretical uncertainties inherent in the MC (primarily due to higher-order QCD effects) can range up to 20%. To reduce the prediction uncertainty further, a “data-driven” approach is used to estimate the SM processes in the SR. In this context, “data-driven” refers to the use of control data (i.e. data that cannot contain signal) to directly estimate or supplement the estimation of SM processes in the SR.

3.2.1 Visible final states to constrain invisible final states

As a starting point, let us tackle the estimation of $Z \rightarrow \nu\nu$ in the SR. Since the momentum imbalance (up to experimental effects) in a $Z \rightarrow \nu\nu$ event is just the transverse momentum of the Z boson (p_T^Z), we must estimate p_T^Z . To good approximation, the p_T^Z distribution is independent of the decay mode of the Z boson. Therefore, it is natural to estimate $p_T^{\text{miss}}(Z \rightarrow \nu\nu)$ by measuring $p_T^Z(Z \rightarrow \mu\mu)$, as muons are easily identifiable and reconstructible.

However, there is one important distinction between $\nu\nu$ and $\mu\mu$ events. In the latter, p_T^Z can be directly measured, whereas in the former it must be inferred through a momentum imbalance. Effects like jet energy scale and acceptance can impact p_T^{miss} , but not $p_T^{\mu\mu}$. Therefore, instead of directly measuring $p_T^{\mu\mu}$ in $\mu\mu$ events, we define and use the hadronic recoil U :

$$\vec{U} = \vec{p}_T^{\text{miss}} + \sum_{\mu} \vec{p}_T^{\mu} + \sum_e \vec{p}_T^e + \sum_{\gamma} \vec{p}_T^{\gamma} \quad (3.7)$$

In the SR (where there are no e, μ, γ), $U = p_T^{\text{miss}}$. In $Z \rightarrow \mu\mu$ events, U mimics the momentum imbalance, if we had pretended the identified muons did not exist when computing p_T^{miss} . Therefore, U is an exact analogy for p_T^{miss} in the SR. Figure 3.8

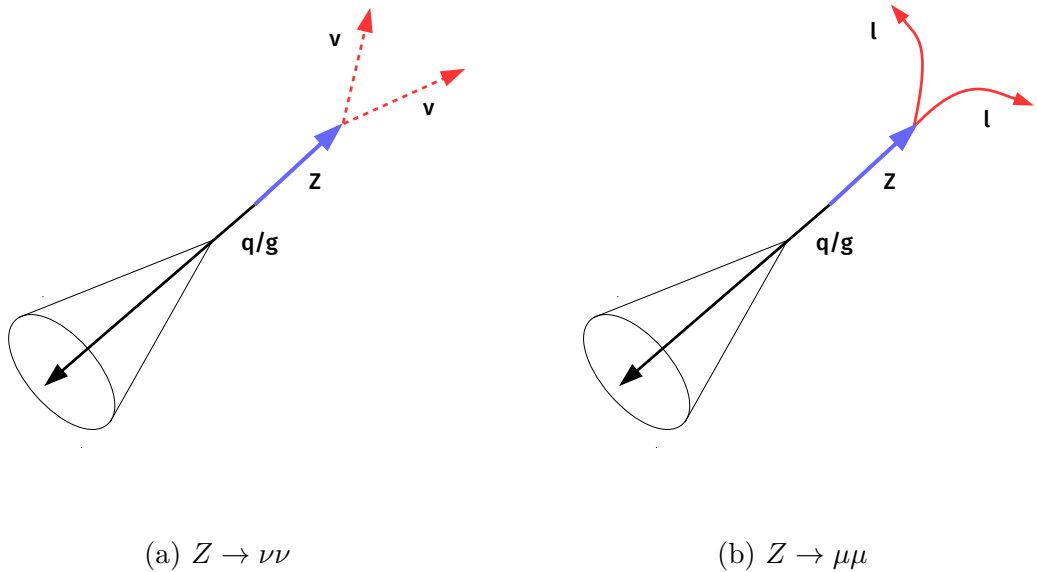


Figure 3.8: Schematic representation of two Z decay modes: to neutrinos (as in the SR) and to muons (as in the CRs). Note that in both cases, U is sensitive to the same effects arising from the measurement of the jet recoiling against the Z boson, whereas $p_T^{\mu\mu}$ is largely independent of the jet.

makes the same argument in a schematic fashion.

Table 3.2 describes the criteria used to define events in the “ $\mu\mu$ ” control regions (CRs). Figure 3.9 shows the distribution of U in these CRs, as well as the $m_{\mu\mu}$ and p_T^μ distributions.

The control data is used to constrain the SR prediction by means of “transfer factors” $T_{Y,i}^X$, where X refers to a particular CR (e.g. $\mu\mu$), Y refers to a particular process (e.g. Z), and i refers to a particular bin in the CR (e.g. $200 < U < 250$ GeV in the tight category). Formally:

$$T_{Z,i}^{\mu\mu} = \frac{N_i^{\text{SR}}(Z \rightarrow \nu\nu)}{N_i^{\mu\mu}(Z \rightarrow \mu\mu)} \quad (3.8)$$

The transfer factors are estimated using MC simulation. To encode the effects of

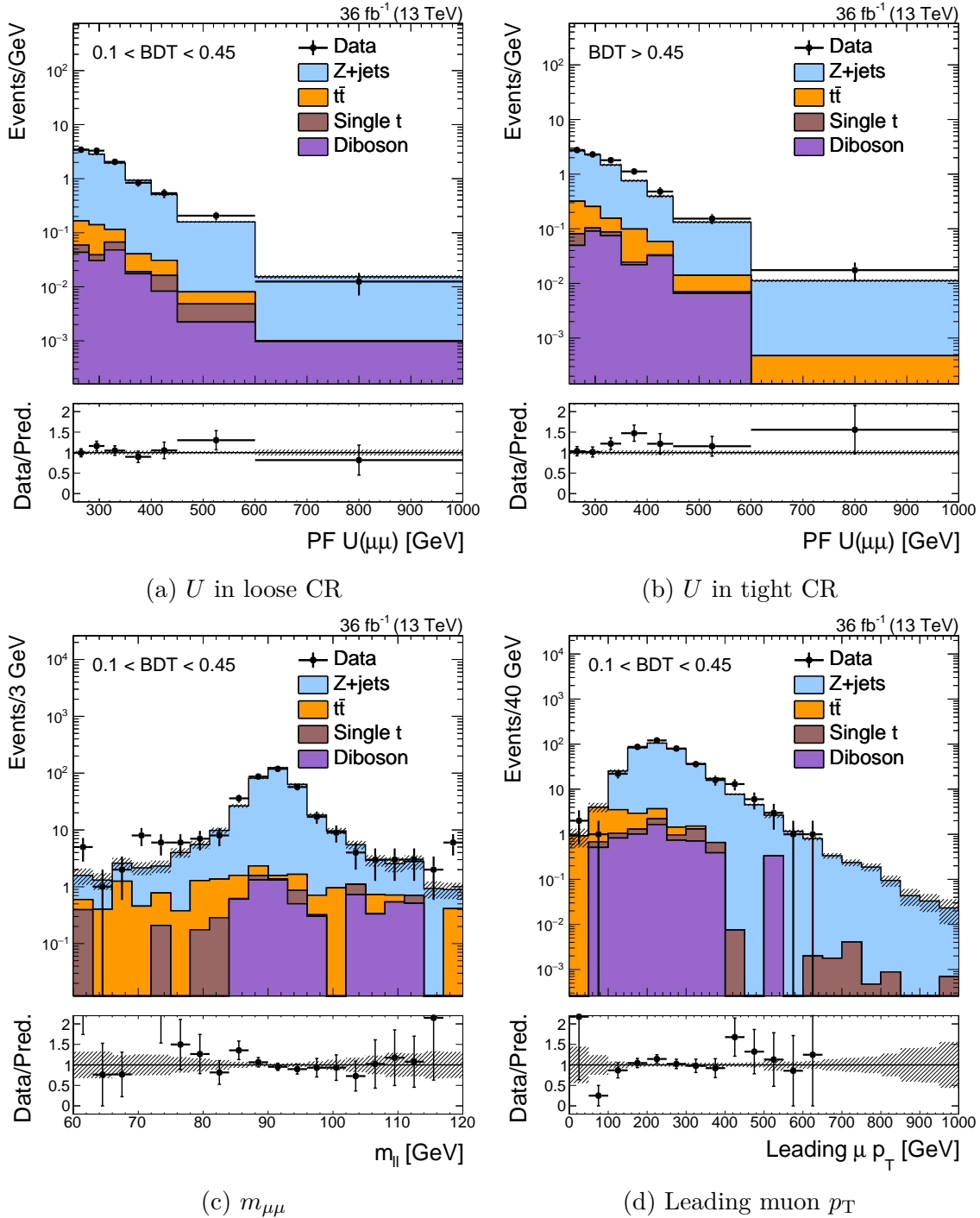


Figure 3.9: Various kinematic distributions in the two mono-top $\mu\mu$ CRs. Note the clearly discernible peak in the $m_{\mu\mu}$ distribution near m_Z

Table 3.2: Criteria used to select events for the mono-top $Z \rightarrow \mu\mu$ CR. As with the SR, the region is further split based on the jet BDT score.

Criterion	Notes
$U > 250$ GeV	Mimicking the selection in the SR; also constrained by trigger thresholds.
1 CA15 jet with $p_T > 250$ GeV	Same as SR
CA15 jet $110 < m_{SD} < 210$ GeV	Same as SR
Well-identified μ^-, μ^+ pair, with $ m_{\mu\mu} - m_Z < 30$ GeV	Identifying the $Z \rightarrow \mu\mu$ resonance.
No identified e, τ_h	Same as SR.
No identified γ	Same as SR
$\min_{\text{jets}} \Delta\phi(\text{jet}, U) > 0.5$	Same as SR
CA15 jet BDT	Same as SR

various uncertainties, we introduce nuisance parameters $\boldsymbol{\theta}$. That is:

$$T_{Y,i}^X \rightarrow T_{Y,i}^X(\boldsymbol{\theta}) \equiv T_{Y,i}^X \times \prod_{j=0}^{n_\theta} (1 + \theta_j) \quad (3.9)$$

$$\theta_j \sim p_j(\theta_j) \quad (3.10)$$

where n_θ is the number of nuisance parameters and $p_j(\theta_j)$ is some prior distribution for each nuisance (see below for how the priors are used). The priors are typically chosen to have a central value (e.g. mean, median) at 0, with a finite variance that encodes the uncertainty. In this chapter, we assume p_j is either a normal distribution centered at 0 or a log-normal distribution (in cases where negative values are undesirable). We will use the terms “uncertainty” and “nuisance parameter” interchangeably.

Let $\text{Pois}(d|\lambda)$ refer to the Poisson probability of observing d with an expected mean of λ . In terms of these transfer factors, the likelihood for the data observed in the signal and $\mu\mu$ control regions is:

$$\begin{aligned} \mathcal{L}(\mathbf{d} \mid \mu, \boldsymbol{\mu}_{\text{SR}}^{Z \rightarrow \nu\nu}, \boldsymbol{\theta}) = \prod_{i \in \text{bins}} & \left[\text{Pois}\left(d_i^{\text{SR}} \mid \mu S_i^{\text{SR}}(\boldsymbol{\theta}) + \mu_{\text{SR},i}^{Z \rightarrow \nu\nu} + B_i^{\text{SR}}(\boldsymbol{\theta})\right) \right. \\ & \times \text{Pois}\left(d_i^{\mu\mu} \mid \frac{\mu_{\text{SR},i}^{Z \rightarrow \nu\nu}}{T_{Z,i}^{\mu\mu}(\boldsymbol{\theta})} + B_i^{\mu\mu}(\boldsymbol{\theta})\right) \left. \right] \times \prod_{j=0}^{n_\theta} p_j(\theta_j) \end{aligned} \quad (3.11)$$

where the following notation is used:

d_i^X : The data observed in bin i of region X . For now, $X = \text{SR}, \mu\mu$.

S_i^{SR} : The predicted number of signal events in bin i of the SR, under some fixed signal hypothesis.

μ : The “signal strength”. Essentially an unconstrained nuisance parameter that scales up or down the total signal yield.

$\mu_{\text{SR},i}^P$: The expected number of events from process P in bin i of the SR. This is also an unconstrained nuisance parameter.

B_i^X : The predicted number of “minor” background events in bin i of region X . Here, “minor” refers to all SM processes that are not the signal and are not estimated using a data-driven method.

The signal and background yields \mathbf{S} and \mathbf{B} are estimated using MC. Note that the inclusion of the priors in the likelihood constrains the nuisance parameters to be close to their “nominal” values; moving a θ_j to fit the data incurs a large cost from the prior.

If we set $B_i = \mu = 0$ (the null hypothesis, ignoring small minor backgrounds), a simple picture emerges of how the likelihood is maximized. The parameters $\mu_{\text{SR}}^{Z \rightarrow \nu\nu}$ float freely to satisfy $d_{\text{SR},i} \sim \mu_{\text{SR},i}^{Z \rightarrow \nu\nu}$ and $d_{\mu\mu,i} \sim \mu_{\text{SR},i}^{Z \rightarrow \nu\nu} / T_{Z,i}^{\mu\mu}(\boldsymbol{\theta})$. If both constraints cannot be satisfied simultaneously by scaling $\mu_{\text{SR}}^{Z \rightarrow \nu\nu}$, the (constrained) nuisance parameters $\boldsymbol{\theta}$ modify the transfer factor $T_Z^{\mu\mu}$. Table 3.6 shows the relevant uncertainties for $T_Z^{\mu\mu}$, and Figure 3.10 shows the shape of uncertainties that evolve as a function of U .

The transfer factors are shown in Figure 3.11. The exact values of $T_Z^{\mu\mu}(\boldsymbol{\theta})$ have two salient features:

1. The values are strictly greater than one. This is due to (a) $\mathcal{B}(Z \rightarrow \nu\nu) > \mathcal{B}(Z \rightarrow \mu\mu)$ and (b) a non-100% efficiency in reconstructing and identifying muons. This implies that the constraining power of the $\mu\mu$ CR is less than that of the SR, especially at high U (i.e. the Poisson uncertainties are larger).

Table 3.3: Uncertainties affecting the $\mu\mu \leftrightarrow \nu\nu$ extrapolation. “Shape” uncertainties have different priors for each bin, but are assumed to be correlated across bins.

Uncertainty	1 s.d.	Notes
μ ID	2%	
μ track	1%	
τ_h veto	3%	
$Z + \text{heavy flavor}$	3%	
Trigger	0-2%	Shape
b -tag	$\sim 0.5\%$	Shape
$udcsg$ -mistag	3-4%	Shape

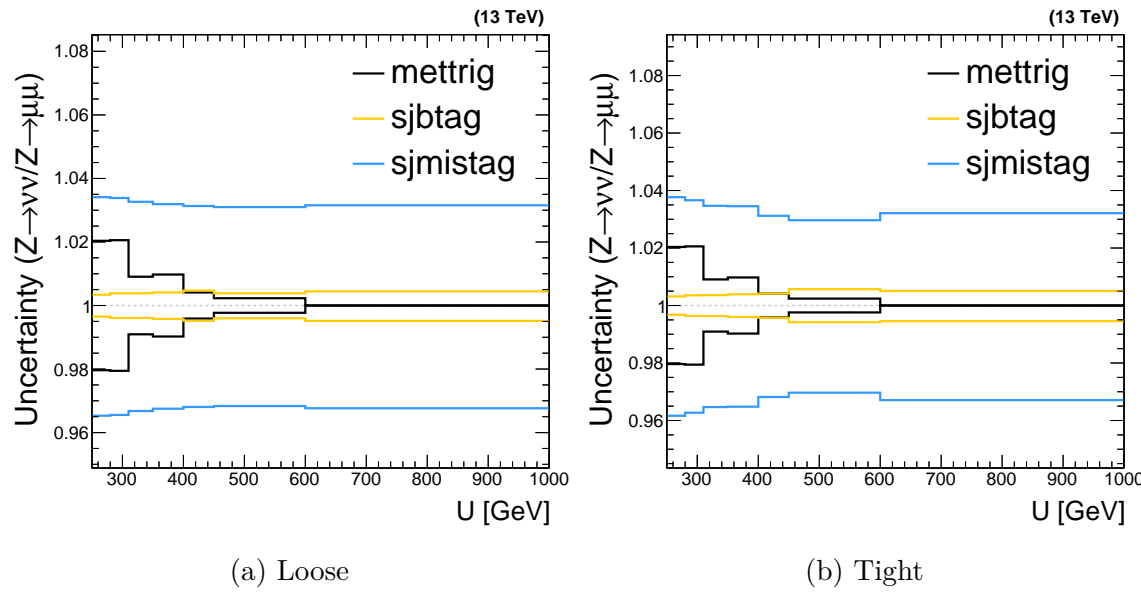


Figure 3.10: Shape uncertainties affecting $T_i^{\mu\mu}$ in both categories, as a function of U .

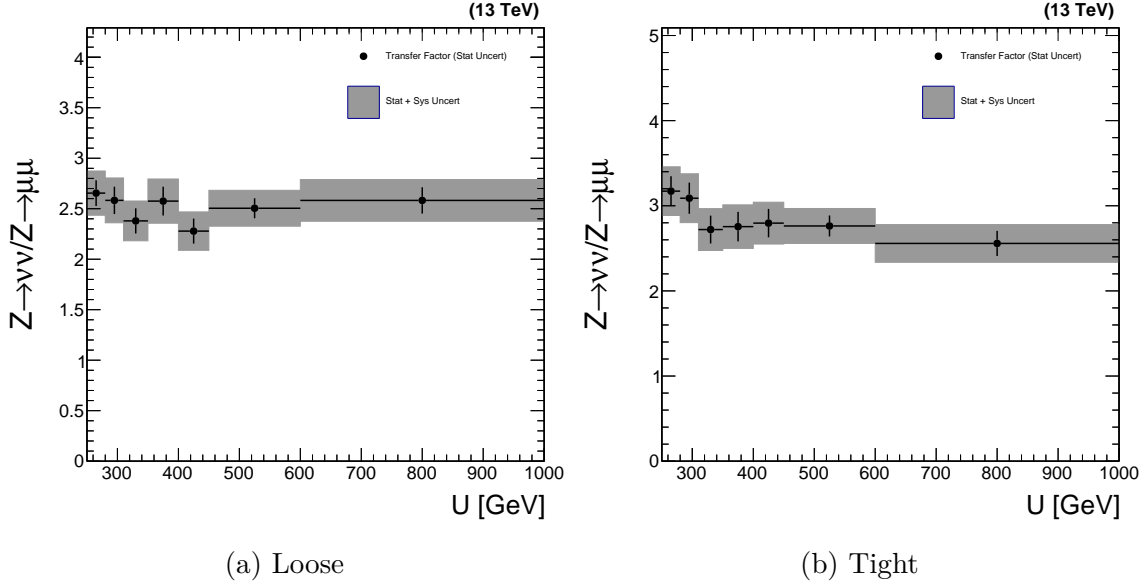


Figure 3.11: The transfer factors $T_{Z,i}^{\mu\mu}$ as a function of recoil and BDT score. The vertical black bars represent the Poisson uncertainties in the MC simulation, while the grey bands represent the sum of Poisson uncertainties and other, systematic, uncertainties. All uncertainties are represented as one standard deviation.

2. The one standard deviation variation of all uncertainties that impact $T_{Z,i}^{\mu\mu}$ are contained within a 10% envelope. This is already a factor of two smaller than the inherent $\sim 20\%$ uncertainties in the MC simulation.

To account for point (1), we can simply add more control data by also looking at $Z \rightarrow ee$ decays. Essentially all of the arguments used for the $\mu\mu$ CRs applies to the ee CRs. Figures 3.12-3.13 show the data/simulation agreement and the transfer factors for the new dielectron regions. A further set of statistical constraints to improve the estimate at high U (which is where the signals are most enhanced) is described in Section 3.2.2.

Similar methods are used to predict the W +jets and $t\bar{t}$ contributions in the SRs; these three backgrounds comprise at least 95% of the SM processes. In both cases, the momentum imbalance in the SR is a proxy for the momentum of the W boson, since the charged lepton is lost. A sketch of the event topologies is shown in Figure 3.14. Following the same arguments as used for the $Z \rightarrow ll$ CRs, we can use the hadronic recoil U in CRs that measure visible final states of W and $t\bar{t}$.

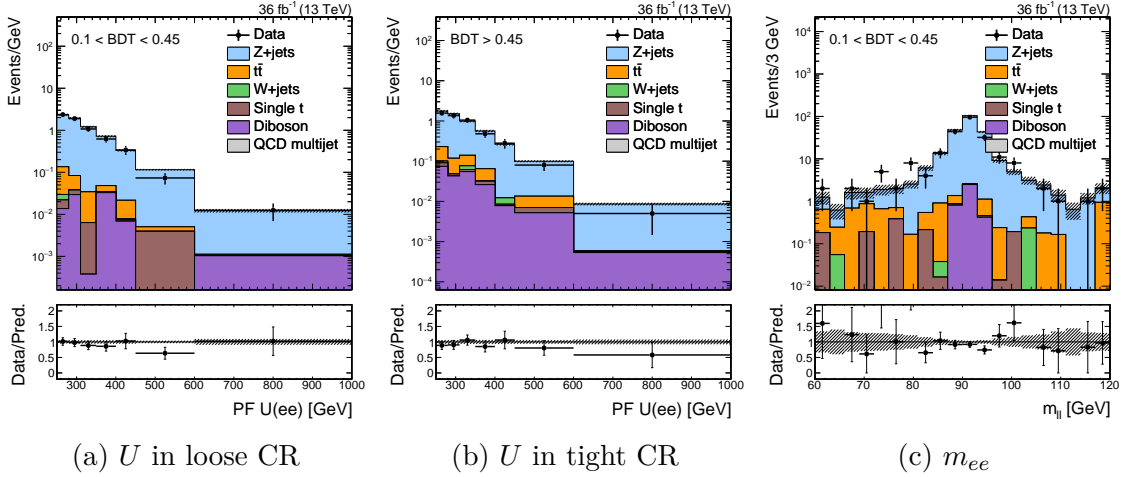


Figure 3.12: Various kinematic distributions in the two mono-top ee CRs.

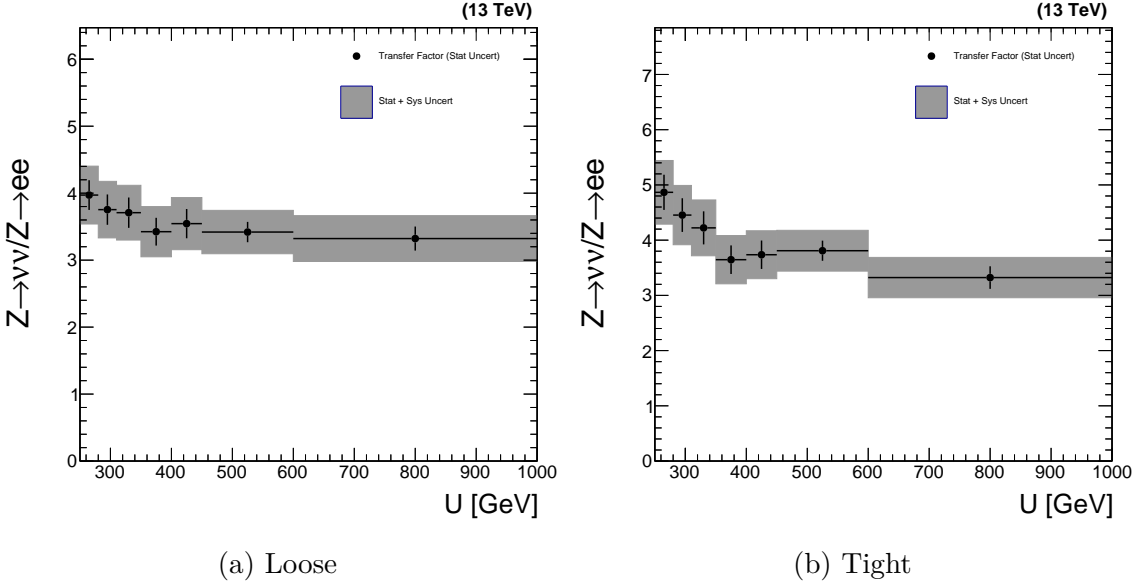


Figure 3.13: The transfer factors T_i^{ee} as a function of recoil and BDT score. The vertical black bars represent the Poisson uncertainties in the MC simulation, while the grey bands represent the sum of Poisson uncertainties and other, systematic, uncertainties. All uncertainties are represented as one standard deviation.

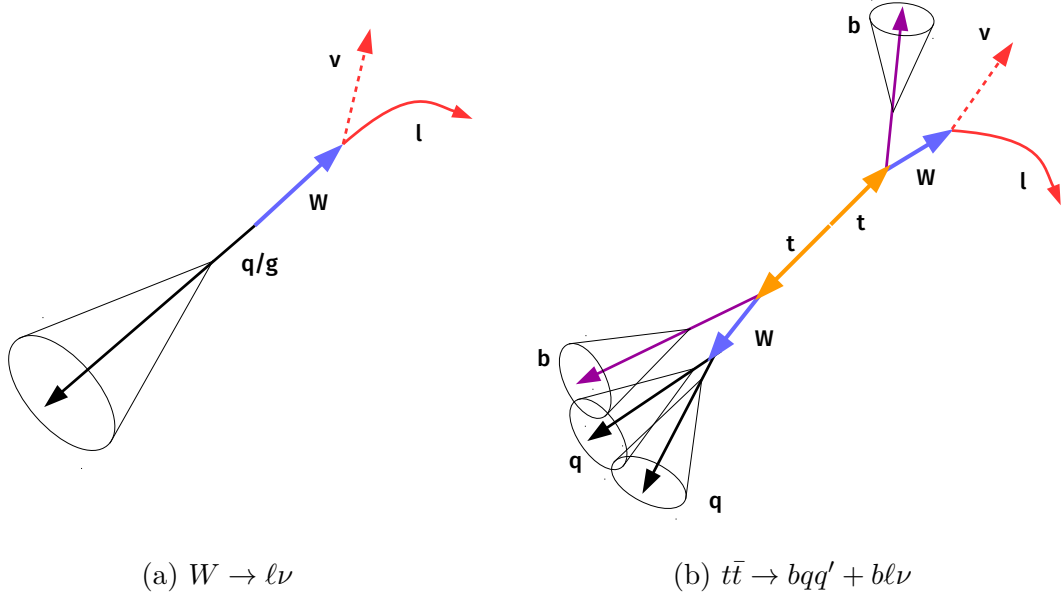


Figure 3.14: Schematic representation of the W and $t\bar{t}$ SM processes. In both cases, $U \approx p_T^W$. Furthermore, if the charged lepton is lost, $U = p_T^{\text{miss}} \approx p_T^W$.

Starting with muon final states (electrons will follow naturally), we define two sets of CRs based on the number of identified B hadrons. The selection for the $b\mu$ CRs (to measure $t\bar{t}$) is shown in Table 3.4. The selection for the μ CRs (to measure W) is shown in Table 3.5. Figures 3.15-3.16 show various kinematic distributions in these regions.

Each CR gets a set of transfer factors to constrain the targeted process in the SR: $\mathbf{T}_{t\bar{t}}^{b\mu}$ and \mathbf{T}_W^μ . In the tight μ CR (Figures 3.16b-3.16c), the stringent top ID requirement enhances the $t\bar{t}$ and suppresses the W contribution. Since we cannot create a pure W in the tight category, we introduce an additional set of transfer factors $\mathbf{T}_{t\bar{t}}^\mu$. This extra constraint uses the $b\mu$ CRs to estimate the $t\bar{t}$ component in the μ CRs, thereby leaving only one large degree of freedom in the μ CRs. These three sets of transfer factors, and the corresponding uncertainties, are shown in Figure 3.17.

As we added the ee CRs to complement the $\mu\mu$ CRs, we also add be (e) CRs to augment the statistical power of the $b\mu$ (μ) CRs, especially at high recoil. Figures 3.18 and 3.19 respectively show some kinematic distributions and the transfer factors corresponding to these electron constraints.

Table 3.4: Criteria used to select events for the mono-top $b\mu$ CR. As with the SR, the region is further split based on the jet BDT score.

Criterion	Notes
$U > 250 \text{ GeV}$	Mimicking the selection in the SR; also constrained by trigger thresholds.
1 CA15 jet with $p_T > 250 \text{ GeV}$	Same as SR
CA15 jet $110 < m_{SD} < 210 \text{ GeV}$	Same as SR
At least one b -tagged sub-jet	Identifying B hadron produced from hadronic top decay.
Exactly one b -tagged narrow jet	Identifying B hadron produced from leptonic top decay.
Exactly one well-identified μ	Produced from $W \rightarrow \mu\nu$
No identified e, τ_h	Same as SR.
No identified γ	Same as SR
$\min_{\text{jets}} \Delta\phi(\text{jet}, U) > 0.5$	Same as SR
CA15 jet BDT	Same as SR

Table 3.5: Criteria used to select events for the mono-top μ CR. As with the SR, the region is further split based on the jet BDT score.

Criterion	Notes
$U > 250 \text{ GeV}$	Mimicking the selection in the SR; also constrained by trigger thresholds.
1 CA15 jet with $p_T > 250 \text{ GeV}$	Same as SR
CA15 jet $110 < m_{SD} < 210 \text{ GeV}$	Same as SR
No b -tagged sub-jets	Suppressing semi-leptonic $t\bar{t}$ decays
No b -tagged narrow jets	Suppressing semi-leptonic $t\bar{t}$ decays
Exactly one well-identified μ	Produced from $W \rightarrow \mu\nu$
No identified e, τ_h	Same as SR.
No identified γ	Same as SR
$\min_{\text{jets}} \Delta\phi(\text{jet}, U) > 0.5$	Same as SR
CA15 jet BDT	Same as SR

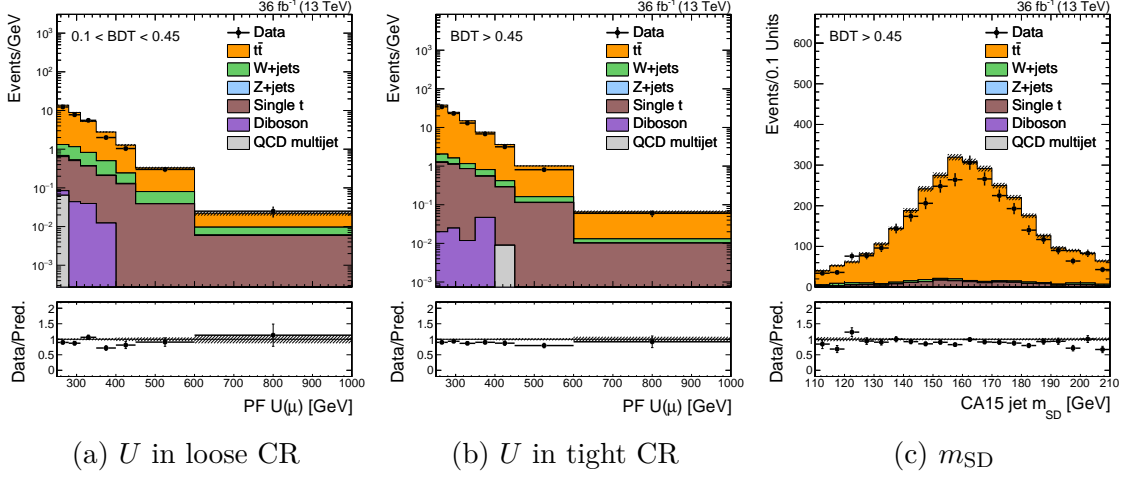


Figure 3.15: Various kinematic distributions in the two mono-top $b\mu$ CRs.

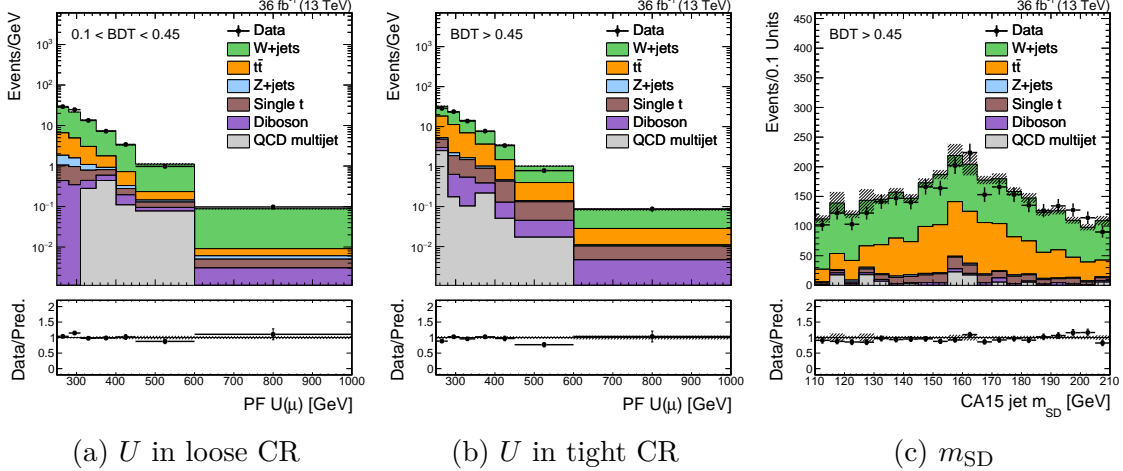


Figure 3.16: Various kinematic distributions in the two mono-top μ CRs.

Table 3.6: Uncertainties affecting the various single-muon extrapolations. “Shape” uncertainties have different priors for each bin, but are assumed to be correlated across bins.

Uncertainty	1 s.d. ($T_{t\bar{t}}^{b\mu}$)	1 s.d. (T_W^μ)	1 s.d. ($T_{t\bar{t}}^\mu$)	Notes
μ ID	1%	1%	1%	
μ track	0.5%	0.5%	0.5%	
τ_h veto	3%	3%	3%	
W +heavy flavor		3%		
Trigger	0-2%	0-2%	0-2%	Shape
b -tag	2%	$\sim 0.5\%$	3-6%	Shape
$udcsg$ -mistag	1%	5%	1%	Shape

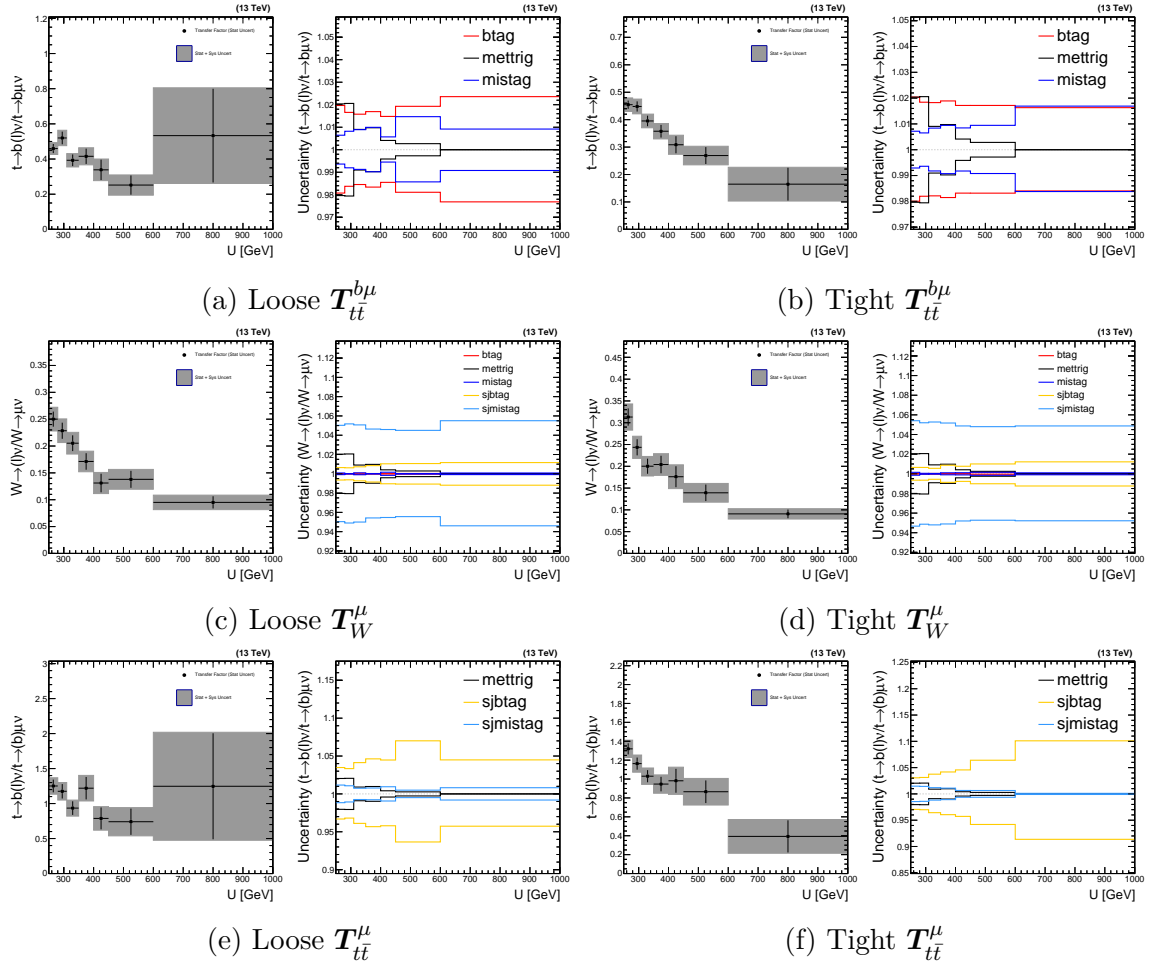


Figure 3.17: The transfer factors $T_{t\bar{t}}^{b\mu}$, T_W^μ , and $T_{t\bar{t}}^\mu$; and corresponding shape uncertainties.

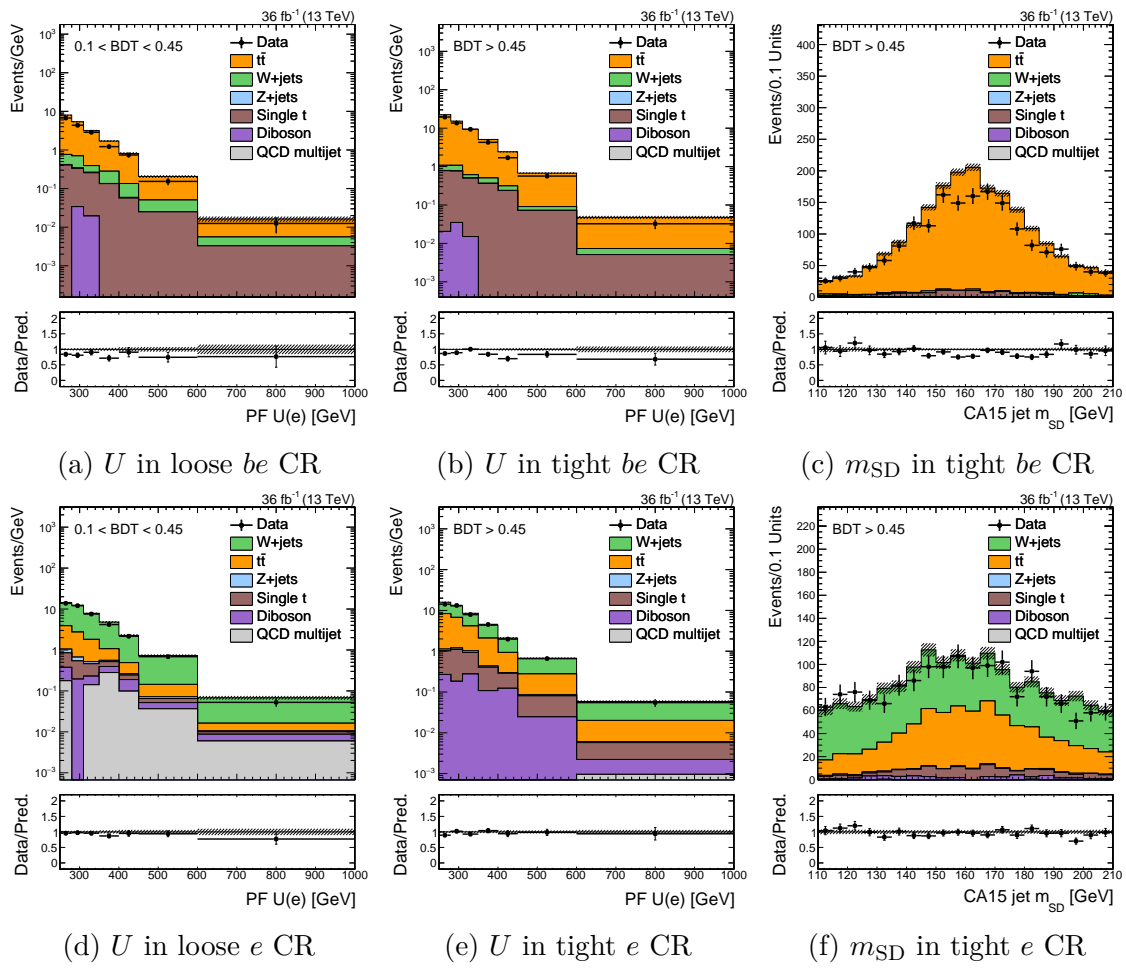


Figure 3.18: Various kinematic distributions in the mono-top be CRs (top) and e CRs (bottom).

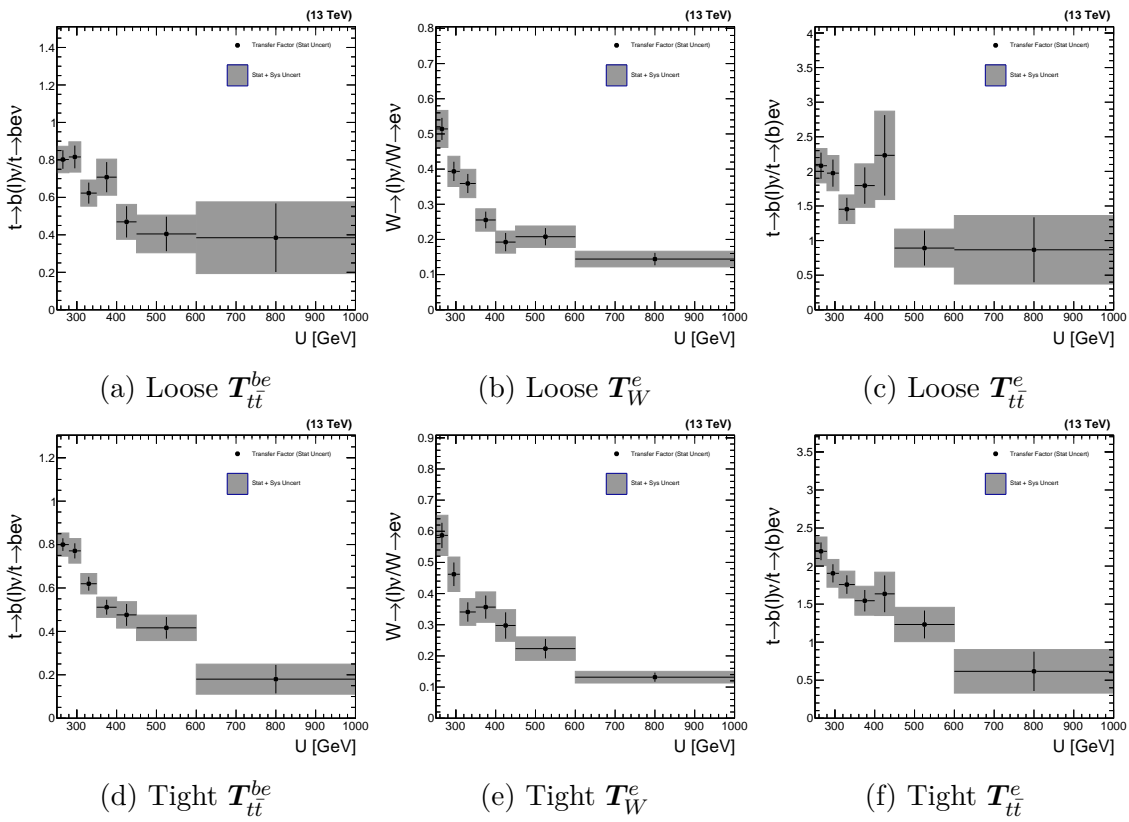


Figure 3.19: The transfer factors \mathbf{T}_{tt}^{be} , \mathbf{T}_W^e , and \mathbf{T}_{tt}^e

Having defined (almost all of) the CRs and transfer factors, we can write down a complete likelihood for the mono-top search:

$$\begin{aligned} \mathcal{L}(\mathbf{d} | \mu, \boldsymbol{\mu}_{\text{SR}}^{Z \rightarrow \nu\nu}, \boldsymbol{\mu}_{\text{SR}}^{W \rightarrow \ell\nu}, \boldsymbol{\mu}_{\text{SR}}^{t\bar{t}}, \boldsymbol{\theta}) = \\ \prod_{i \in \text{bins}} \left[\text{Pois}\left(d_i^{\text{SR}} \mid \mu S_i^{\text{SR}}(\boldsymbol{\theta}) + \mu_{\text{SR},i}^{Z \rightarrow \nu\nu} + \mu_{\text{SR},i}^{W \rightarrow \ell\nu} + \mu_{\text{SR},i}^{t\bar{t}} + B_i^{\text{SR}}(\boldsymbol{\theta})\right) \right. \\ \times \prod_{X=\mu\mu,ee} \text{Pois}\left(d_i^X \mid \frac{\mu_{\text{SR},i}^{Z \rightarrow \nu\nu}}{T_{Z,i}^X(\boldsymbol{\theta})} + B_i^X(\boldsymbol{\theta})\right) \\ \times \prod_{X=b\mu,be} \text{Pois}\left(d_i^X \mid \frac{\mu_{\text{SR},i}^{t\bar{t}}}{T_{t\bar{t},i}^X(\boldsymbol{\theta})} + B_i^X(\boldsymbol{\theta})\right) \\ \left. \times \prod_{X=\mu,e} \text{Pois}\left(d_i^X \mid \frac{\mu_{\text{SR},i}^{W \rightarrow \ell\nu}}{T_{W,i}^X(\boldsymbol{\theta})} + \frac{\mu_{\text{SR},i}^{t\bar{t}}}{T_{t\bar{t},i}^X(\boldsymbol{\theta})} + B_i^X(\boldsymbol{\theta})\right) \right] \times \prod_{j=0}^{n_\theta} p_j(\theta_j) \quad (3.12) \end{aligned}$$

3.2.2 Theoretically-limited extrapolations

Despite the combination of the $\mu\mu$ and ee regions, there are still large statistical uncertainties in the estimate of $Z \rightarrow \nu\nu$ at high U . This is apparent in Figure 3.12, in which exactly one event is observed in the last bin of the tight CR. The dilepton CRs are limited by $\sigma(pp \rightarrow Z \rightarrow \nu\nu) > \sigma(pp \rightarrow Z \rightarrow \ell^+\ell^-)$; accordingly, to alleviate this limitation, we look to a process with a much bigger cross-section. In similar regions of final-state phase space, $\sigma(pp \rightarrow \gamma + \text{jets}) \sim 30 \times \sigma(pp \rightarrow Z(\rightarrow \nu\nu) + \text{jets})$. Therefore, it is natural to use the γ +jet production spectrum as a way to estimate the Z +jet spectrum. As before, let us define another transfer factor:

$$T_{\gamma,i}^\gamma = \frac{N_i^{\text{SR}}(Z \rightarrow \nu\nu)}{N_i^\gamma(\gamma)} \quad (3.13)$$

However, unlike the \mathbf{T}_Y^X we have discussed so far (which correlate similar processes, e.g. $Z \rightarrow \nu\nu/Z \rightarrow \mu\mu$), T_{γ}^γ is highly sensitive to the theoretical predictions of the Z and γ spectra.

To reduce the impact of higher-order effects on \mathbf{T}_γ^γ , we ensure that the numerator and denominator are predicted to as high an order as possible. Leading-order MC is used to simulate V +jet processes, because higher-order simulations are much more

computationally intensive. We therefore choose to produce a less accurate LO simulation, as opposed to a more accurate, but statistically-limited, NLO simulation. While producing sufficient NLO simulation for the analysis is prohibitive, we can compute certain inclusive distributions at NLO. Since $U \approx p_T^V$ is the quantity of interest in this analysis, we want to ensure this distribution is accurately predicted. It is clear from Figure 3.20 that adding an additional QCD order induces large corrections, both at low and high p_T^V . In the LO simulation, we can obtain an estimate of the uncertainty due to NLO effects by varying the renormalization and factorization scales (μ_R, μ_F) by factors of two. This is represented by the red envelope and grey band in Figure 3.20 and clearly is insufficient to cover NLO effects. Therefore, we compute a simple correction for the NLO QCD effects, known as a k -factor:

$$k_{Z,\text{QCD}}(p_T^Z) = \frac{d\sigma_{\text{NLO QCD}}(Z)/dp_T^Z}{d\sigma_{\text{LO}}(Z)/dp_T^Z} \quad (3.14)$$

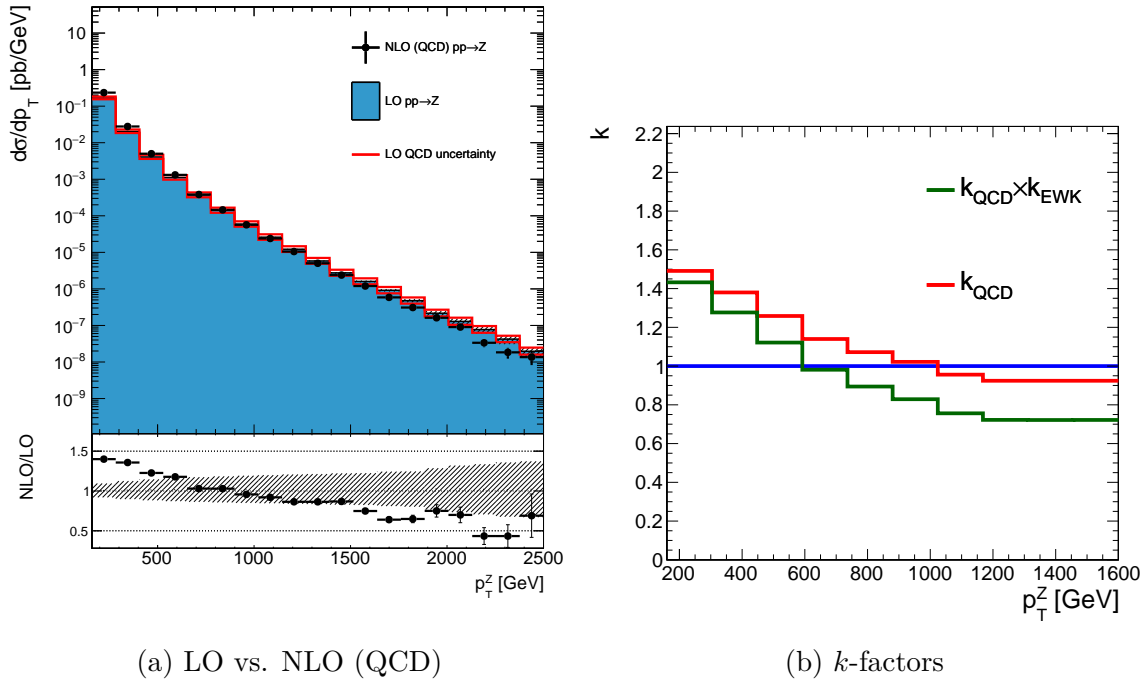
We include another k -factor, k_{EWK} , to correct for higher-order EWK effects. Unlike k_{QCD} , k_{EWK} is derived using a theoretical calculation [20, 21, 25] instead of NLO simulation. k_{EWK} covers NLO EWK terms, as well as large Sudakov logarithms that appear at high p_T^V in the NNLO expansion (NLL).

Figure 3.21 compares the k -factors for all three $V + \text{jet}$ processes. While there are similar trends as a function of p_T^V , it is clear that the corrections are quite different for each process. Therefore, transfer factors like T_{γ}^{γ} are strongly sensitive to NLO effects, i.e.:

$$T_{\gamma,i}^{\gamma} = \frac{N_i^{\text{SR}}(Z \rightarrow \nu\nu)}{N_i^{\gamma}(\gamma)} \neq \frac{N_i^{\text{SR,LO}}(Z \rightarrow \nu\nu)}{N_i^{\gamma,\text{LO}}(\gamma)} \quad (3.15)$$

The distributions in Sections 3.1-3.2 are all corrected using these k -factors. Figure 3.22 shows the equivalent for CRs that target $\gamma + \text{jet}$ events, and Table 3.7 describes the selection used to define these CRs.

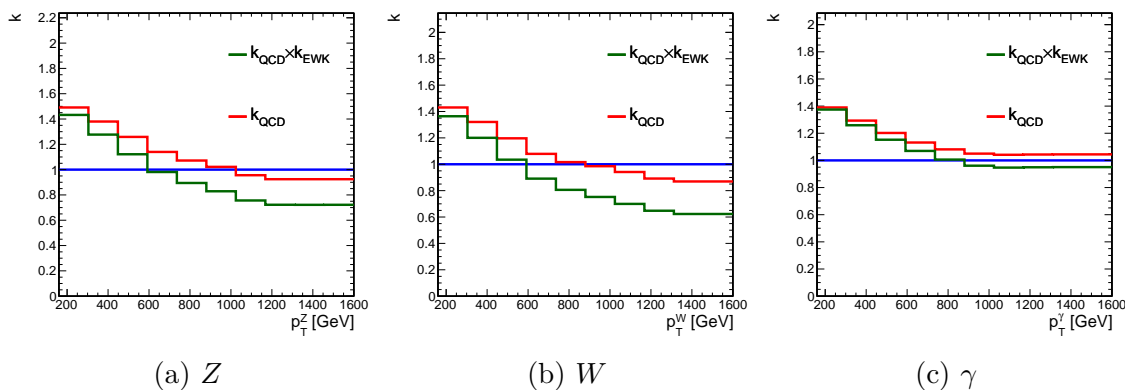
Now that we can describe T_{γ}^{γ} at NLO, we must assess the impact of unknown higher-order terms on the transfer factors. We account for variations caused by uncertainties in the PDF model by taking the RMS of the 100 parameter variations prescribed for the NNPDF3.0 set [2]. By varying μ_F and μ_R by factors of 0.5 and



(a) LO vs. NLO (QCD)

(b) k -factors

Figure 3.20: Theoretical predictions for p_T^Z in $Z + \text{jet}$ events and the corresponding k -factors. No detector simulation is applied in these figures; all quantities are directly from MC simulation of the physics process. “LO QCD uncertainty” refers to an estimate of the effect of the QCD renormalization and factorization scales on the LO simulation. The grey band in the ratio is the quadrature sum of the QCD and statistical uncertainties.

Figure 3.21: Differential k -factors for each of the $V + \text{jet}$ processes.

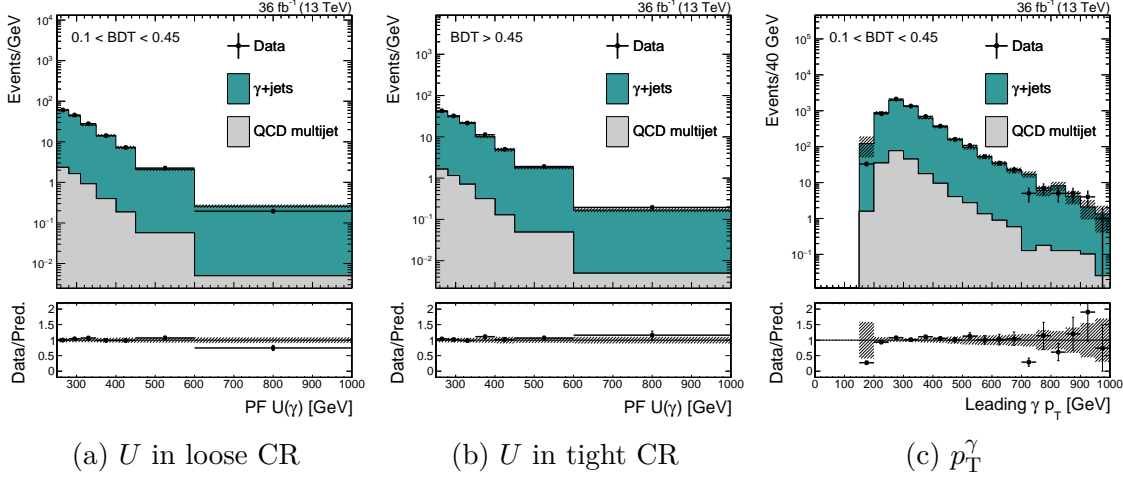


Figure 3.22: Various kinematic distributions in the two mono-top γ CRs.

Table 3.7: Criteria used to select events for the mono-top γ CR. As with the SR, the region is further split based on the jet BDT score.

Criterion	Notes
$U > 250$ GeV	Mimicking the selection in the SR
1 CA15 jet with $p_T > 250$ GeV	Same as SR
CA15 jet $110 < m_{SD} < 210$ GeV	Same as SR
No identified μ, e, τ_h	Same as SR.
Well-identified γ with $p_T^\gamma > 175$ GeV	High- p_T photon, set by trigger threshold
$\min_{\text{jets}} \Delta\phi(\text{jet}, U) > 0.5$	Same as SR
CA15 jet BDT	Same as SR

2, we assess the effect of the integration scale choices on \mathbf{T} . These scale and PDF uncertainties cover all unknown QCD effects on the production of electroweak bosons. To be conservative, they are assumed to be uncorrelated between processes. However, the uncertainties are correlated between all bins (i.e. as a function of p_T^V). A second set of uncertainties is included for higher-order EWK effects, following what is suggested in References [13, 14, 15, 20, 21, 23, 24, 25, 26] and agreed upon in the LHC Dark Matter Working Group. These EWK uncertainties break down into three categories:

- Unknown Sudakov logarithms in the NLL correction. These uncertainties are correlated across processes (Z, W, γ).
- Missing NNLO EWK effects not covered by the NLL correction. These are not correlated across processes.
- The full difference between the NLL correction and an exponentiation of the NLO correction; also not correlated across processes.

It should be stressed that while these uncertainties apply to the prediction of each V +jet processes, they do not affect transfer factors that correlate processes differing only in decay mode or acceptance. This is simply because these uncertainties primarily deal with the initial state or the production of an electroweak boson, which is not related to the description of the decay to leptons or the experimental identification of leptons and b -jets. That is:

$$T_{Z,i}^{\mu\mu} = \frac{N_i^{\text{SR}}(Z \rightarrow \nu\nu)}{N_i^{\mu\mu}(Z \rightarrow \mu\mu)} \approx \frac{N_i^{\text{SR,LO}}(Z \rightarrow \nu\nu)}{N_i^{\mu\mu,\text{LO}}(Z \rightarrow \mu\mu)} \quad (3.16)$$

Now that we have tools to construct transfer factors of the form $N(V)/N(V')$ with reasonably small uncertainties (i.e. smaller than the statistical uncertainty of the data), it is natural to add another transfer factor to our toolbox:

$$T_{Z/W,i}^{\text{SR}} = \frac{N_i^{\text{SR}}(Z \rightarrow \nu\nu)}{N_i^{\text{SR}}(W \rightarrow \ell\nu)} \quad (3.17)$$

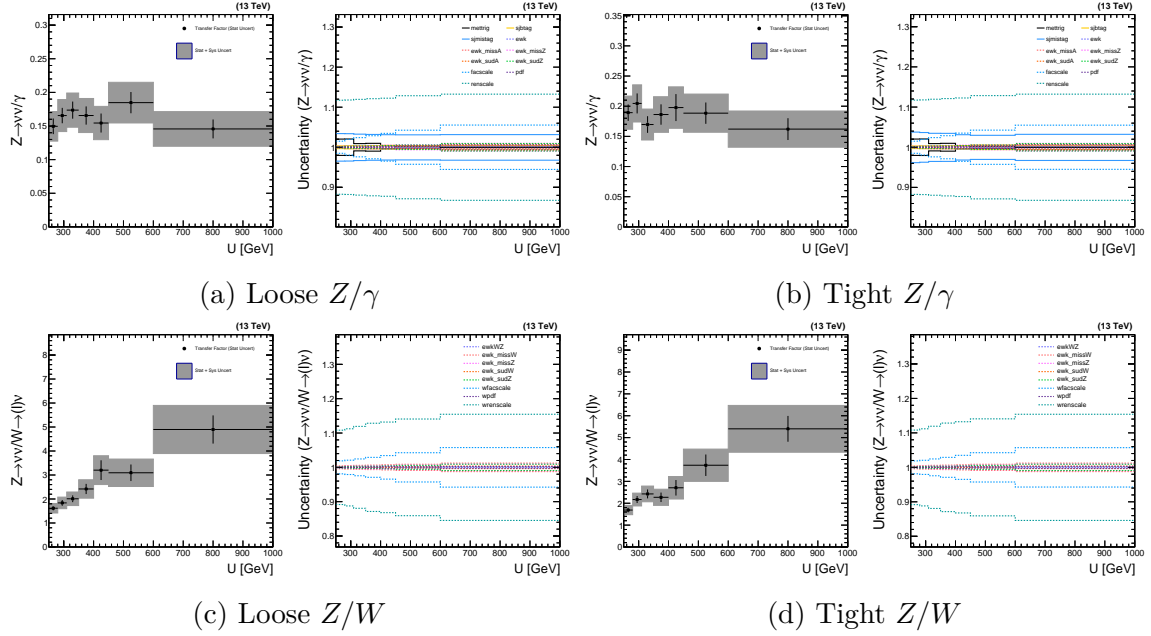


Figure 3.23: The transfer factors \mathbf{T}_γ^γ and $\mathbf{T}_{Z/W}^{\text{SR}}$; and corresponding shape uncertainties.

This allows us to use the e, μ CRs (which target $W + \text{jet}$ production) to further reduce the uncertainty in the estimation of $Z \rightarrow \nu\nu$ in the SR. For technical reasons, the transfer factor is defined as the ratio Z/W in the SR. However, the SR and the μ CR are connected through a product of transfer factors:

$$N_i^{\text{SR}}(Z \rightarrow \nu\nu) = T_{Z/W,i}^{\text{SR}}(\hat{\boldsymbol{\theta}}) \times T_{W,i}^\mu(\hat{\boldsymbol{\theta}}) \times N_i^\mu(W \rightarrow \ell\nu) \quad (3.18)$$

where $\hat{\boldsymbol{\theta}}$ is the maximum-likelihood estimate of $\boldsymbol{\theta}$.

Figure 3.23 shows these additional transfer factors and their shape uncertainties. It is clear from inspection that $\mathbf{T}_\gamma^\gamma \ll 1$, and the same holds for the effective transfer factor $\mathbf{T}_{Z/W}^{\text{SR}} \times \mathbf{T}_W^\mu$. This indicates that the CR data to which the transfer factor is linked has greater statistical power than the SR data.

Having included all of these components, the likelihood can be written as:

$$\begin{aligned}
\mathcal{L}(\mathbf{d} \mid \mu, \boldsymbol{\mu}_{\text{SR}}^{Z \rightarrow \nu\nu}, \boldsymbol{\mu}_{\text{SR}}^{t\bar{t}}, \boldsymbol{\theta}) = & \\
\prod_{i \in \text{bins}} \left[\text{Pois}\left(d_i^{\text{SR}} \mid \mu S_i^{\text{SR}}(\boldsymbol{\theta}) + \mu_{\text{SR},i}^{Z \rightarrow \nu\nu} + \frac{\mu_{\text{SR},i}^{Z \rightarrow \nu\nu}}{T_{Z/W,i}^{\text{SR}}(\boldsymbol{\theta})} + \mu_{\text{SR},i}^{t\bar{t}} + B_i^{\text{SR}}(\boldsymbol{\theta})\right) \right. & \\
\times \prod_{X=\mu\mu, ee} \text{Pois}\left(d_i^X \mid \frac{\mu_{\text{SR},i}^{Z \rightarrow \nu\nu}}{T_{Z,i}^X(\boldsymbol{\theta})} + B_i^X(\boldsymbol{\theta})\right) & \\
\times \prod_{X=b\mu, be} \text{Pois}\left(d_i^X \mid \frac{\mu_{\text{SR},i}^{t\bar{t}}}{T_{tt,i}^X(\boldsymbol{\theta})} + B_i^X(\boldsymbol{\theta})\right) & \\
\times \prod_{X=\mu, e} \text{Pois}\left(d_i^X \mid \frac{\mu_{\text{SR},i}^{Z \rightarrow \nu\nu}}{T_{W,i}^X(\boldsymbol{\theta}) T_{Z/W,i}^{\text{SR}}(\boldsymbol{\theta})} + \frac{\mu_{\text{SR},i}^{t\bar{t}}}{T_{tt,i}^X(\boldsymbol{\theta})} + B_i^X(\boldsymbol{\theta})\right) & \\
\times \text{Pois}\left(d_i^\gamma \mid \frac{\mu_{\text{SR},i}^{Z \rightarrow \nu\nu}}{T_{\gamma,i}^\gamma(\boldsymbol{\theta})}\right] \times \prod_{j=0}^{n_\theta} p_j(\theta_j) & \tag{3.19}
\end{aligned}$$

The discussion in this section has largely relied on arguments from simulation and calculation. We can, however, validate that our estimates of \mathbf{T} and the corresponding uncertainties are reasonable by using CR data and appropriate proxies. For example, to test $\mathbf{T}_\gamma^\gamma \sim N(Z \rightarrow \nu\nu)/N(\gamma)$, we can look at $N(Z \rightarrow \mu\mu)/N(\gamma)$. Up to differences in branching ratio and muon identification, these ratios are identical. Figure 3.24 shows some examples of these proxy ratios. In particular, we see that the Z/γ , Z/W and W/γ ratios are well-described the MC, especially as compared to the systematic uncertainties that are assigned.

3.3 Results

Having built this likelihood, we perform a maximum likelihood fit to the data in all regions simultaneously. The results of a ML fit under a background-only hypothesis (i.e. setting $\mu = 0$) is shown in Figures

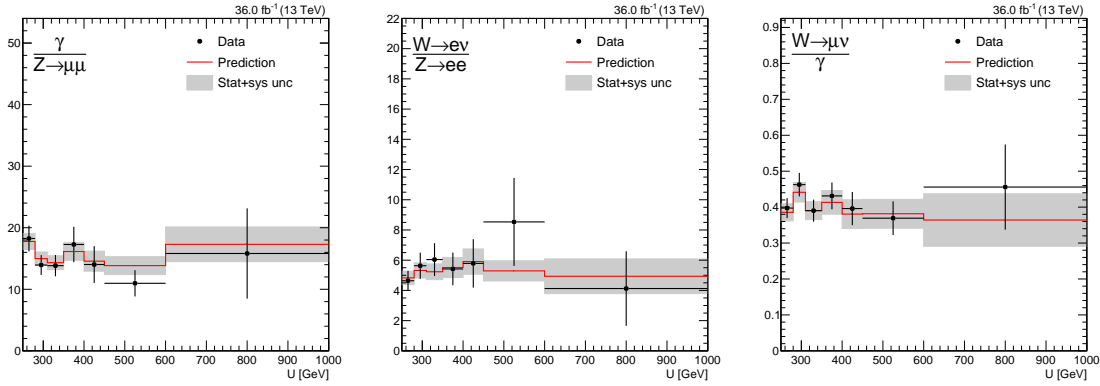


Figure 3.24: Data validation of CR-to-CR transfer factors in the loose category. Only ratios with theoretically-limited systematic uncertainties are shown.

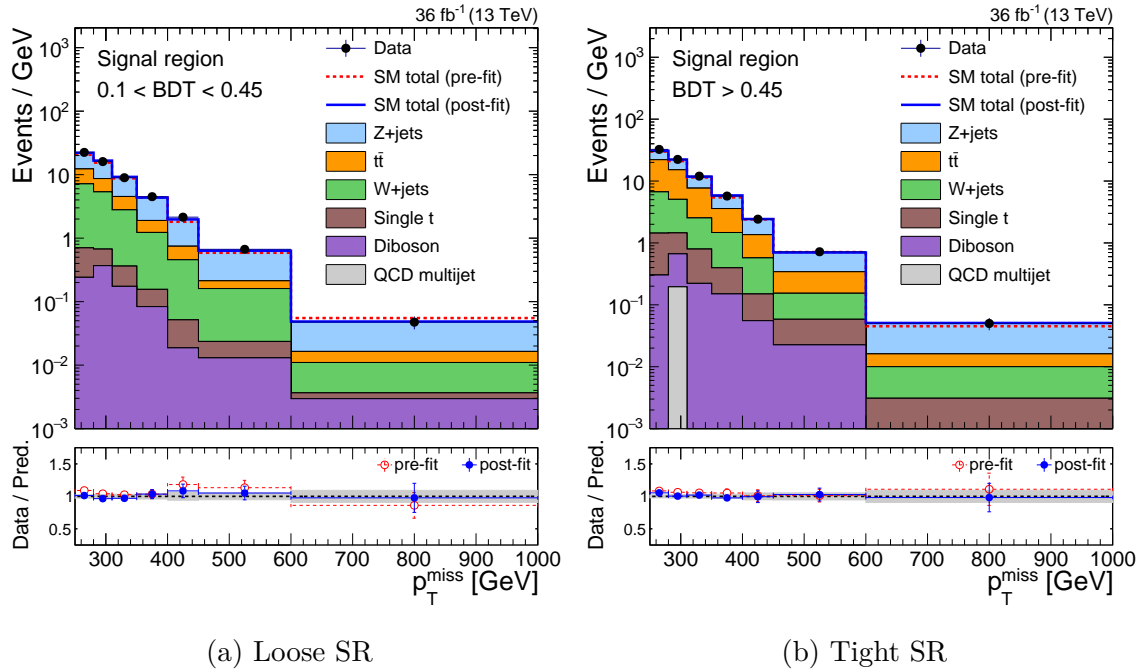


Figure 3.25: Comparison of pre- and post-fit results in the SRs, after simultaneously fitting all channels. The fit is performed having fixed $\mu = 0$.

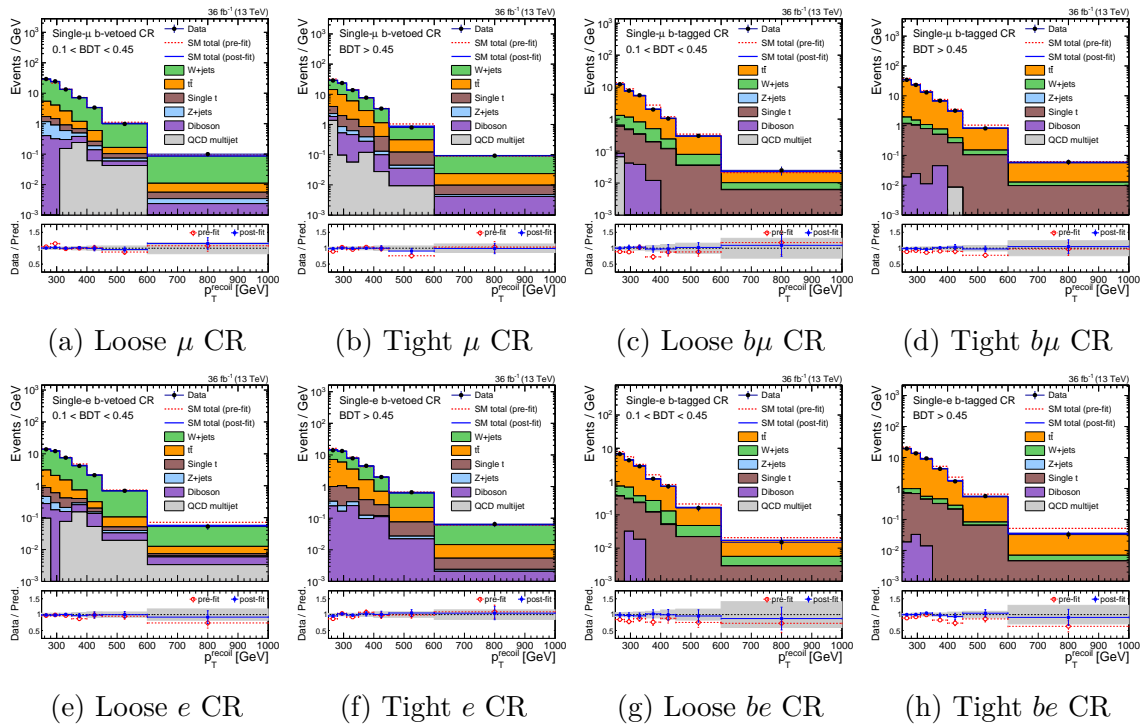


Figure 3.26: Comparison of pre- and post-fit results in the single-lepton CRs, after simultaneously fitting all channels. The fit is performed having fixed $\mu = 0$.

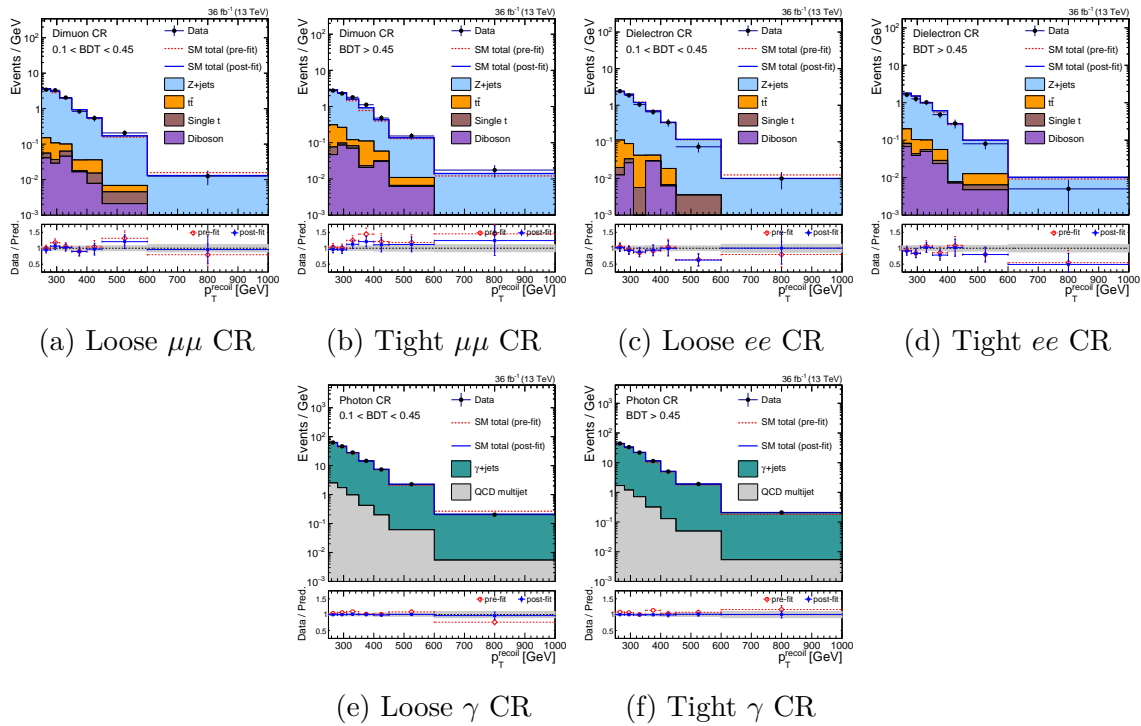


Figure 3.27: Comparison of pre- and post-fit results in the di-lepton and photon CRs, after simultaneously fitting all channels. The fit is performed having fixed $\mu = 0$.

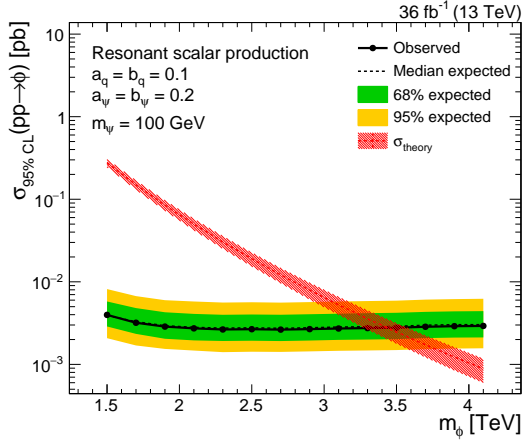


Figure 3.28: 95% CLs upper limits on the cross section of the production of ϕ , where the resonance mass m_ϕ is scanned. Values of m_ϕ for which $\sigma_{95\% \text{ CLs}} < \sigma_{\text{theory}}$ are excluded at 95% confidence level. The dashed black line represents the median expected exclusion, with the green and yellow bands representing the 1 and 2 standard deviation envelopes on the expected exclusion. The red band represents the 1 standard deviation of the uncertainty on the theory cross section (driven by higher-order QCD terms).

3.3.1 Constraints on mono-top models

The results of the previous section show that the background-only (B-only) model is able to describe the data. To quantify the preference of the B-only model to a signal+background model (S+B), we compute 95% CLs upper limits on the signal strength μ for each signal hypothesis. A description of CLs upper limits and the asymptotic profile likelihood method is given in Section [?].

We begin with the simpler of the two models: the resonant scalar. Figure 3.28 shows the upper limit on the cross section of ϕ production as a function of m_ϕ . A fixed value of m_ψ is chosen such that $m_\psi \ll m_\phi$. In this regime, the exact value of m_ψ does not strongly affect the kinematics or cross section; in the opposite regime, the decay $\phi \rightarrow t\bar{\psi}$ is strongly suppressed. The values of the couplings a_q, b_q and a_ψ, b_ψ are similarly fixed to reasonable values. The cross section (and therefore the signal strength μ) roughly scales as $(a_q + b_q)^2$ and $(a_\psi + b_\psi)^2$. Given these assumptions, the observed data excludes scalars with mass $m_\phi < 3.4$ TeV. This can be compared to the expected exclusion, which is also 3.4 TeV.

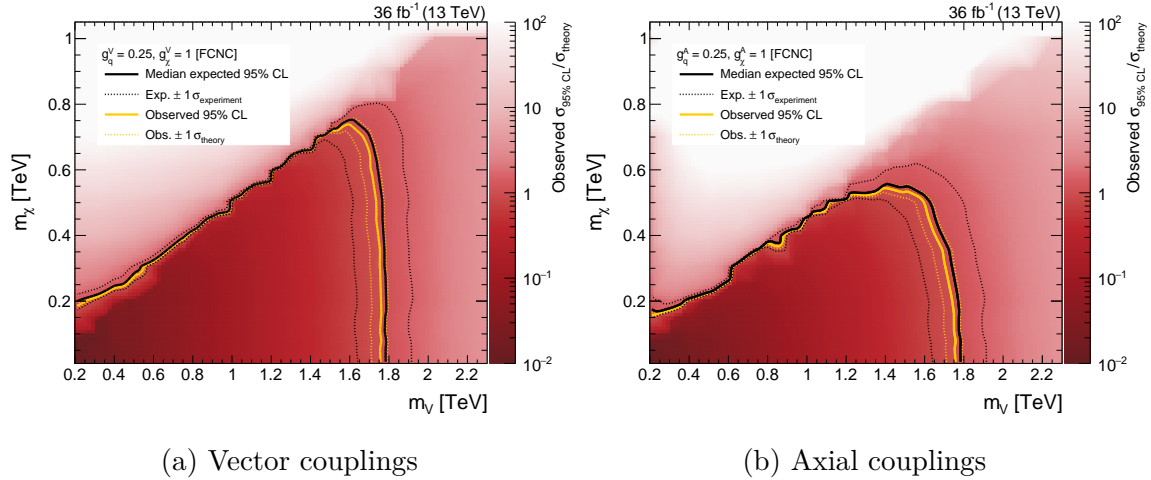


Figure 3.29: 95% CLs upper limits on the signal strength ($\mu = \sigma/\sigma_{\text{theory}}$) of the flavor-violating process $pp \rightarrow t\chi\bar{\chi}$ as a function of m_V and m_χ . Two hypotheses are tested: assuming $g_\chi^V, g_q^V \neq 0$ (vector-like) and assuming $g_\chi^A, g_q^A \neq 0$ (axial vector-like).

The FCNC model contains many more non-trivial parameters, and so we do not simply fix all but one. First, fixing the couplings (at values agreed upon by the LHC Dark Matter Working Group in Reference [16]), we show the upper limits as a function of (m_V, m_χ) in Figure 3.29. Both vector-like and axial vector-like couplings are probed independently. In either scenario, assuming $m_\chi < 50$ GeV, we are able to exclude $0.2 < m_V < 1.75$ TeV. The lower bound arises from measurements of m_t and Γ_t ; allowing $m_V \lesssim 200$ GeV modifies Γ_t beyond measured bounds as the $t^{(*)} \rightarrow Vu$ channel opens. As m_χ crosses the $m_V/2$ boundary, σ_{theory} drops off rapidly, reducing the strength of the exclusion. In the vector case, this defines a clear exclusion triangle bounded by $m_V < 1.75$ TeV and $2m_\chi < m_V$. In the axial-vector case, Γ_V is much narrower, modifying the transition to the off-shell region. On the entire plane, the observed exclusion is consistent with the median expected exclusion within one standard deviation.

Sticking to two-dimensional projections of the parameter space, Figure 3.30 shows the excluded regions as a function of mediator mass m_V and all four free couplings $g_q^V, g_q^A, g_\chi^V, g_\chi^A$. As the DM mass is fixed to be strictly on-shell regardless of m_V , there are no visible differences between the vector and axial-vector scenarios. Assuming

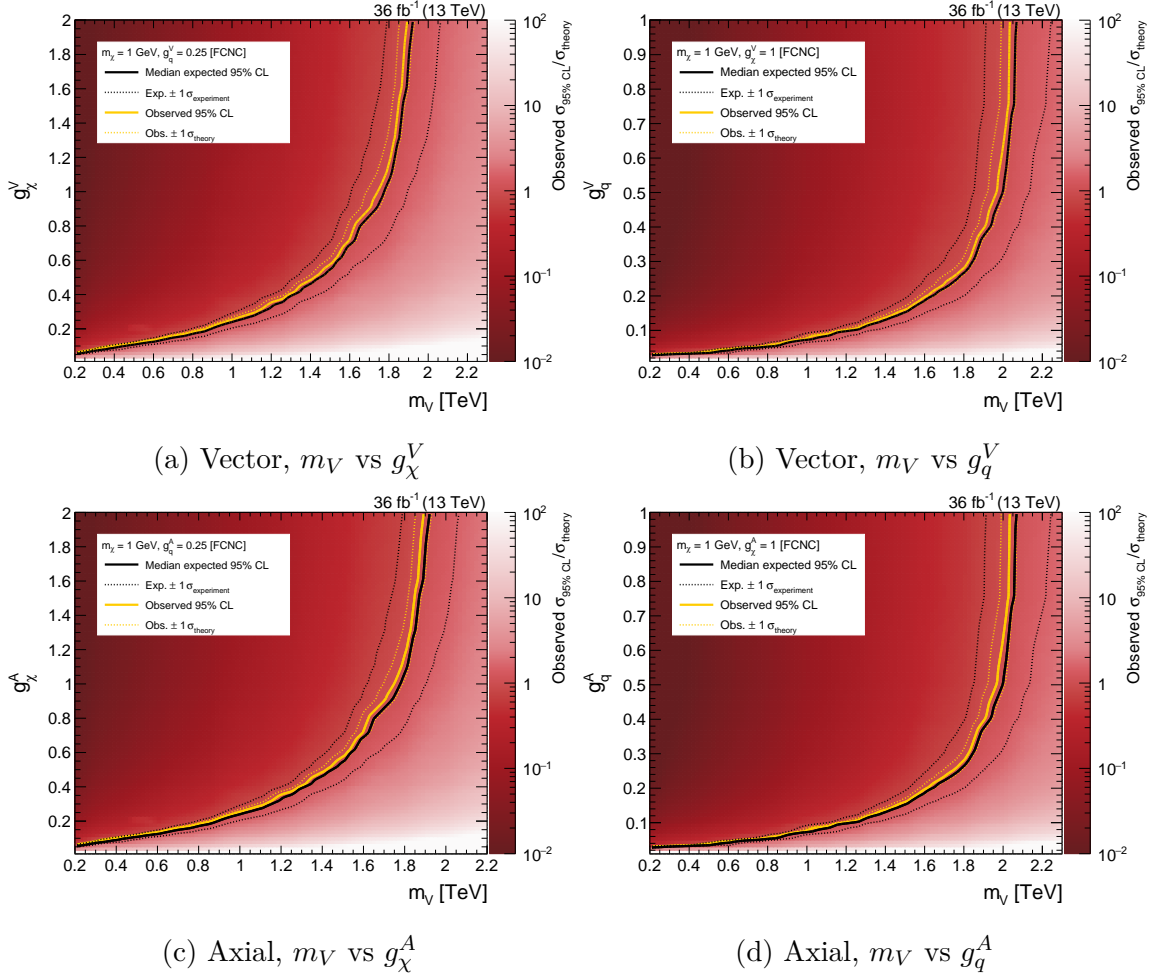


Figure 3.30: 95% CLs upper limits on the signal strength ($\mu = \sigma/\sigma_{\text{theory}}$) of the flavor-violating process $pp \rightarrow t\chi\bar{\chi}$ as a function of m_V , g_q , and g_χ . Two hypotheses are tested: assuming $g_\chi^V, g_q^V \neq 0$ (vector-like) and assuming $g_\chi^A, g_q^A \neq 0$ (axial vector-like). The DM mass m_χ is fixed at 1 GeV.

sufficiently low masses (still corresponding to viable hypotheses), we exclude couplings as weak as $g_q \cdot g_\chi \sim 0.01$.

It is difficult to fully visualize more than two dimensions of the parameter space at a time. Figure 3.31 shows the largest mediator mass that is excluded as a function of g_q^V, g_χ^V (assuming $g_q^A = g_\chi^A = 0$). Given sufficiently large couplings, we exclude FCNCs as massive as 2.5 TeV, while only assuming that $2m_\chi < m_V$.

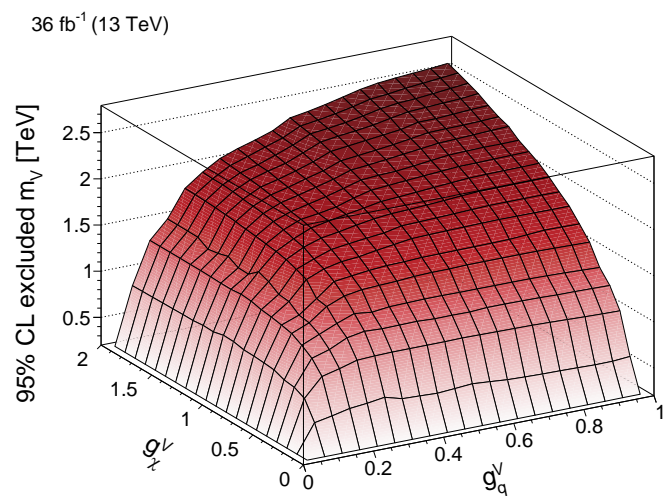


Figure 3.31: Maximum excluded value of m_V for each set of couplings, assuming vector-only couplings.

Chapter 4

The Search for Invisible Decays of the Higgs Boson

The discovery of the SM Higgs boson [???] involved multiple production modes. Gluon fusion has the largest cross section (49 pb) at the LHC because of the large gluon PDF, followed by vector boson fusion (VBF) (3.8 pb), WH (1.4 pb), and ZH (0.89 pb) [11]. While gluon fusion is the most frequent mode, the unique detector signatures of the other production modes can be combined the various Higgs decay signatures to define a signal topology with few backgrounds.

Many DM models [???] allow for DM fermions or scalars to acquire mass through the Higgs mechanism, coupling to the SM Higgs boson. If the DM candidate χ satisfies $2m_\chi < m_H$, then we expect to observe $H \rightarrow \chi\bar{\chi}$. From measurements of the visible branching fractions, we can indirectly place an upper bound of $\mathcal{B}(H \rightarrow \chi\bar{\chi}) < 0.2$ [???]. In this chapter, we describe a direct search for $H \rightarrow \chi\bar{\chi}$ decays.

As with the case of the mono-top search, the $H \rightarrow \chi\bar{\chi}$ process manifests as p_T^{miss} . Each of the aforementioned Higgs production modes translates into a $p_T^{\text{miss}} + X$ signature, where X refers to one or more SM particles. Figure 4.1 shows each of the signatures; in this chapter, we will focus on the VBF production mode, as the unique final state topology provides the best sensitivity to $H \rightarrow \chi\bar{\chi}$.

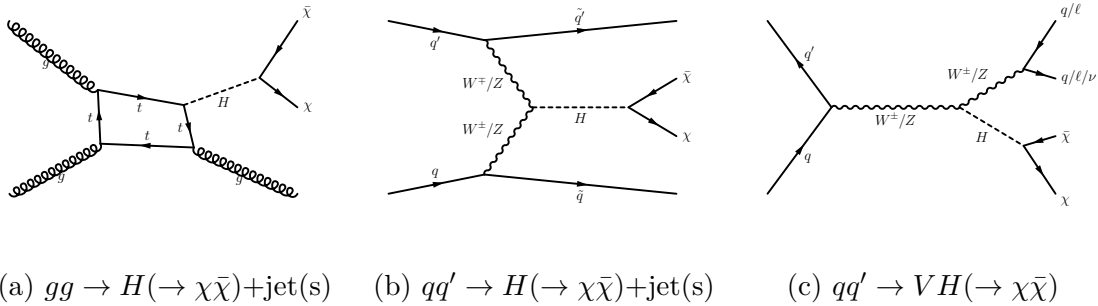


Figure 4.1: Diagrams that contribute to the production of the SM Higgs boson at the LHC, with the subsequent decay to DM candidates. The shown diagrams are all chosen to generate large p_T^{miss} through the presence of one or more SM particles in the final state.

4.1 Signal selection

VBF $H \rightarrow \chi\bar{\chi}$ events are characterized by large p_T^{miss} and two jets. These jets are typically:

- Fairly forward in the detector
- Far apart from each other in η
- Highly energetic (large E , moderate p_T)
- Close together in ϕ

A candidate VBF $H \rightarrow \chi\bar{\chi}$ event displaying these properties is shown in a CMS event display in Figure 4.2.

4.1.1 Online trigger selection

The same trigger decisions (L1 and HLT) as described in Section 3.1.1 are used to select events in this analysis. However, the L1 seeds for the 2016 data run were designed with mono-top-like analyses in mind; i.e., searches where the momentum imbalance is created by central objects. To avoid noise and resolution issues in the forward calorimeters, the L1 seed only considers energy deposits in the region $|\eta| < 3$. Therefore, VBF events in which both jets are in the forward region are not selected.

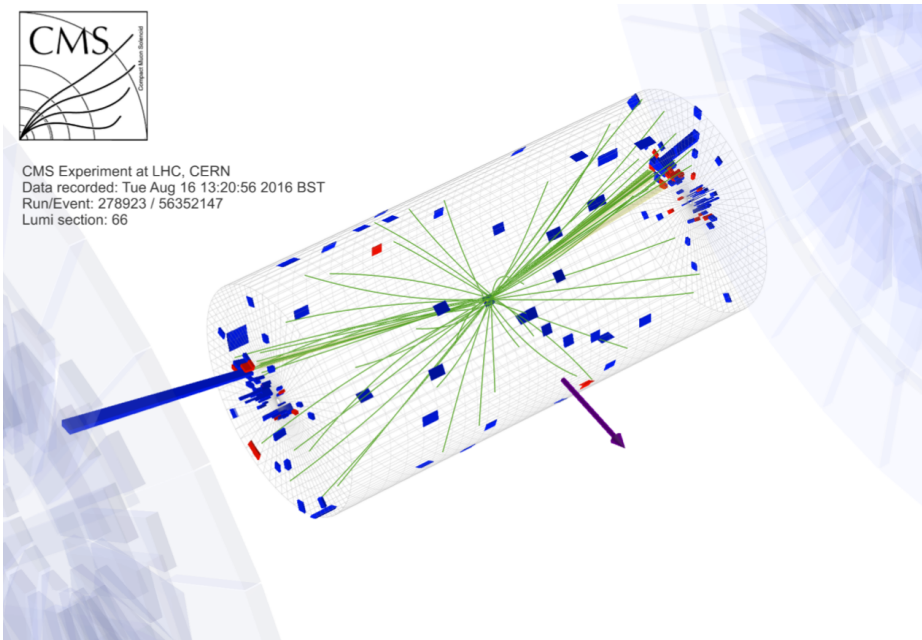


Figure 4.2: Candidate VBF $H \rightarrow \chi\bar{\chi}$ event with two energetic forward jets ($p_T = 180, 107$ GeV) and large p_T^{miss} (360 GeV). Red (blue) towers represent deposits in the hadronic (electromagnetic) calorimeter. Green lines are tracks reconstructed from hits of charged particles in the tracker. The blue arrow represents the direction and magnitude of the p_T^{miss} .

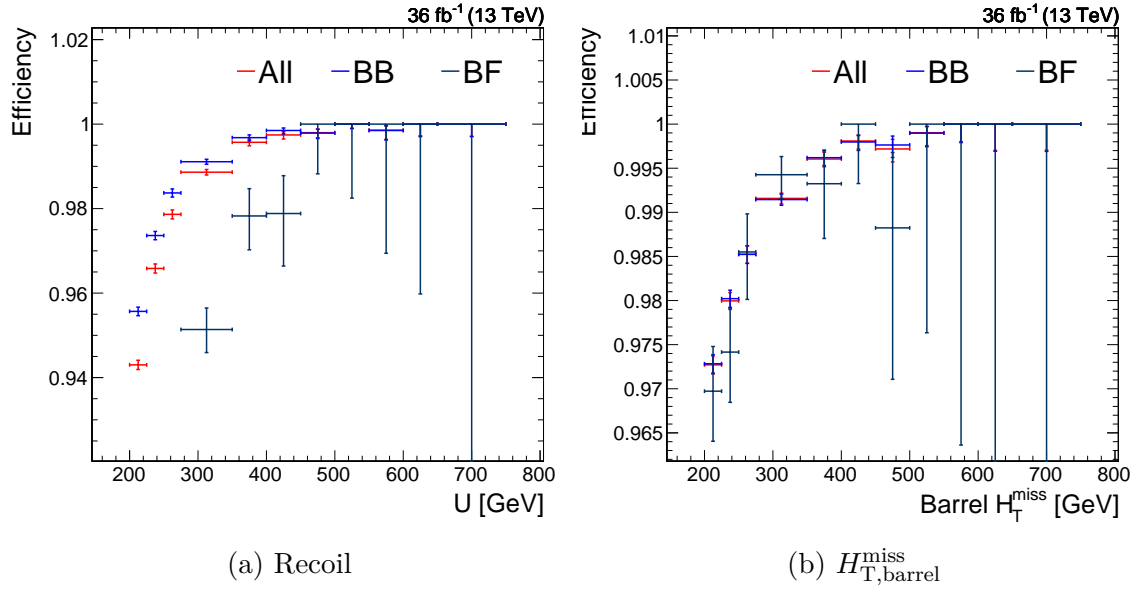


Figure 4.3: Trigger efficiency of events with a VBF-like topology (two jets with $p_T > 80, 40$ GeV) as a function of two different observables. Events are split into two categories: those where both jets have $|\eta| < 3$ (BB) and those where exactly one jet has $|\eta| > 3$ (FF). "All" refers to the sum of these categories.

This is visible in Figure 4.3a, where events are classified based on the location of the two highest- p_T jets. Events with both jets in the barrel (BB) have a higher efficiency than events with one jet in the forward detector (BF). Note that events with two forward jets (FF) are not considered at all, as the efficiency for such events is essentially zero.

The trigger efficiency is truly characterized by the energy deposited in the $|\eta| < 3$ region of the detector, and will be dominated in VBF events by the energy of jets. Accordingly, we define the “missing barrel hadronic transverse momentum”:

$$H_{\text{T,barrel}}^{\text{miss}} = \left| \left(\sum_{j \in \text{barrel}} \vec{p}_j \right)_{\text{T}} \right|, \text{ where barrel refers to jets with } |\eta| < 3 \quad (4.1)$$

As shown in Figure 4.3b, the three categories (BB, BF, All) have similar behavior as a function of $H_{T,\text{barrel}}^{\text{miss}}$. Therefore, we use this parameterization of the efficiency to correct MC simulation to match data.

A second L1-related issue that plagues the 2016 dataset is caused by a “pre-firing”

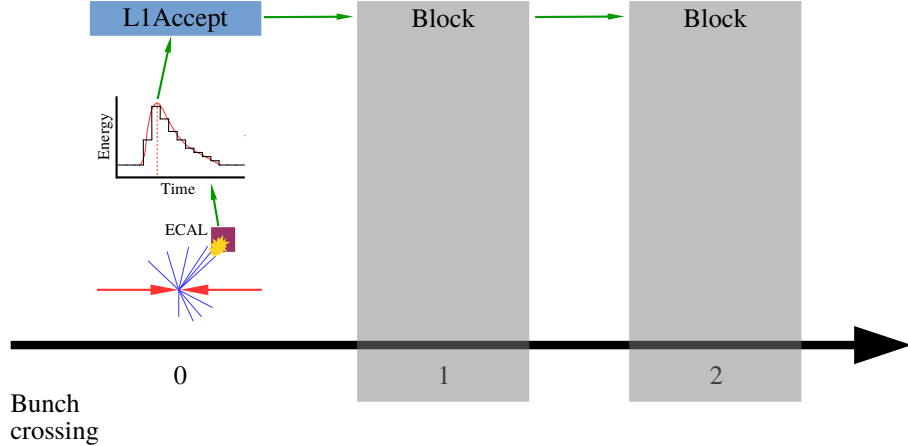


Figure 4.4: A normal event in which an ECAL seed triggers the L1A signal. The subsequent two bunch crossings are blocked. BX₀ refers to the event containing the physics object of interest. Green arrows indicate causality.

effect. When an L1 seed is triggered to accept an event (“L1Accept” or “L1A”), the following two bunch crossings (not necessarily corresponding to collisions) are blocked from firing L1As. At most, two in four consecutive events can fire L1A (i.e. the sequence L1A, blocked, blocked, L1A). Figure 4.4 is an example of a normal ECAL L1 seed accepting an event and blocking the subsequent bunch crossings. In what follows, we will refer to the bunch crossing with an interesting collision (i.e. the one we would like the trigger to select) as BX₀.

A pre-fire refers to the case in which a malformed detector signal is mis-reconstructed, so that the peak of the pulse appears to have occurred in the previous bunch crossing (BX₋₁). In this particular case, a region of the ECAL ($2.5 < |\eta| < 3$) suffered from a loss in transparency due to radiation damage and would produce pulse shapes that are poorly described by the model used to extract the pulse energy and time. When this happens, the L1 seeds for ECAL-based signatures (e.g. electron triggers) can fire an L1A for BX₋₁. This ECAL L1 seed in BX₋₁ will zero out the corresponding ECAL clusters in BX₀ (known as zero suppression), further biasing the event description. So, we would have an L1A for an arbitrary event (BX₋₁), and the interesting event (BX₀) would be blocked from passing the L1 altogether. This is depicted in Figure 4.5. Typically, BX₋₁ contains uninteresting physics signatures, and so is not

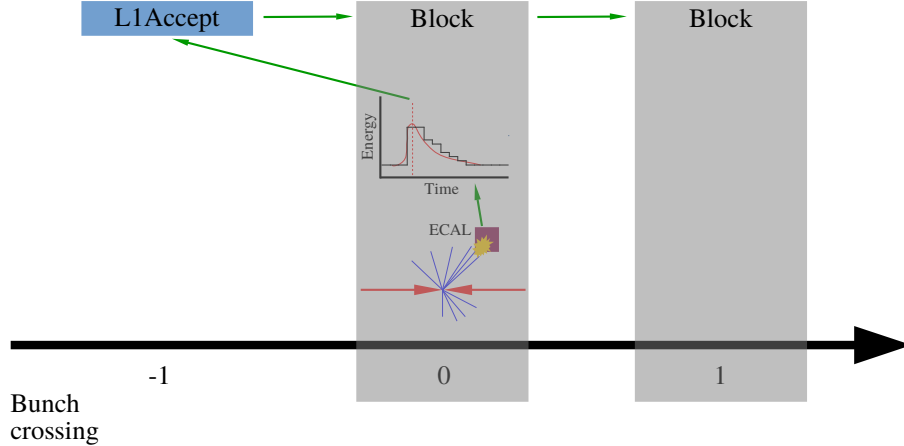


Figure 4.5: A pre-fired event in which an ECAL seed triggers the L1A signal for BX_{-1} . The subsequent two bunch crossings (including the one of interest) are blocked. BX_0 refers to the event containing the physics object of interest. Green arrows indicate causality.

accepted by the HLT.

To measure how often an ECAL energy deposit (typically left by a jet) causes an event to be lost by pre-firing, we need to compute the following efficiency:

$$\epsilon_{\text{pre-fire}}(p_T, \eta, \phi) = \frac{N_{\text{pre-fire}}(p_T, \eta, \phi)}{N_{\text{all events}}(p_T, \eta, \phi)} \quad (4.2)$$

However, by definition, pre-fired events cannot be recorded, and therefore $N_{\text{pre-fire}}(p_T, \eta, \phi)$ is difficult to measure. A very small subset of the recorded dataset (0.2%) consists of “un-pre-fireable” events. These are recorded events (BX_0) in which an L1A fired 3 bunch crossings prior (BX_{-3}). Due to the blocking rules, L1A cannot fire in BX_{-2} and BX_{-1} . Even if there is an ECAL seed in BX_0 that pre-fires, it will be blocked from firing an L1A, and therefore BX_0 is protected. If some other object in BX_0 manages to pass L1 and HLT decisions, then BX_0 will be recorded and can be studied. A schematic of such events is shown in Figure 4.6.

The L1 trigger system records trigger primitive (TP) information (4-vectors of physics objects considered in an L1 selection) for BX_{-1} if BX_0 is triggered. This means we can identify the cases in which a physics object in BX_0 coincides with a TP in BX_{-1} , indicating a pre-fire. Therefore (using the bunch crossing numbering in

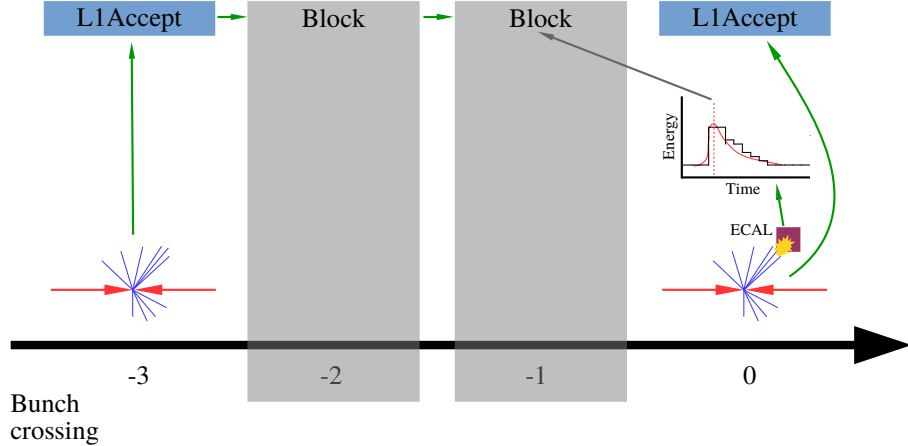


Figure 4.6: An un-pre-fireable event in which BX_{-3} protects BX_0 from being pre-fired. Green arrows indicate causality.

Figure 4.6), we re-define the efficiency:

$$\epsilon_{\text{pre-fire}}(p_T, \eta, \phi) = \frac{N_{\text{pre-fire } \text{BX}_0 | \text{BX}_{-3}}(p_T, \eta, \phi)}{N_{\text{BX}_0 | \text{BX}_{-3}}(p_T, \eta, \phi)} \quad (4.3)$$

By definition, all events in this ratio will be recorded. Figure 4.7 shows this efficiency as a function of jet location. We observe there is a “hot” ECAL tower near the location $\eta = -2.8$ and $\phi = 2$. Not only does this tower fire very frequently (leading to many particles, leading to many jets), but it almost always pre-fires. To first order, events with a jet in this crystal should be rejected. Beyond this, there is very little localization in the pre-fire probability (besides restriction to the ECAL endcap).

In Figure 4.8 we see $\epsilon_{\text{pre-fire}}$ as a function of p_T in a restricted η range. Firstly, we observe that $\epsilon_{\text{pre-fire}}$ increases as a function of p_T , and the turn-on is sharper as a function of EM p_T . This is explained by the mechanism of the pre-fire: the individual ECAL trigger seeds have a threshold of 30 GeV. The higher the jet p_T , the higher the probability of the jet depositing 30 GeV of EM energy in a localized area, setting off an L1 seed. Secondly, we observe a strong dependence on the reference triggers used to select BX_0 . For example, jet-based triggers (JetHT) lead to a much higher efficiency than p_T^{miss} -based triggers (MET). This is a consequence of zero suppression biasing the BX_0 triggers, as shown diagrammatically in Figure 4.9. Muon-based

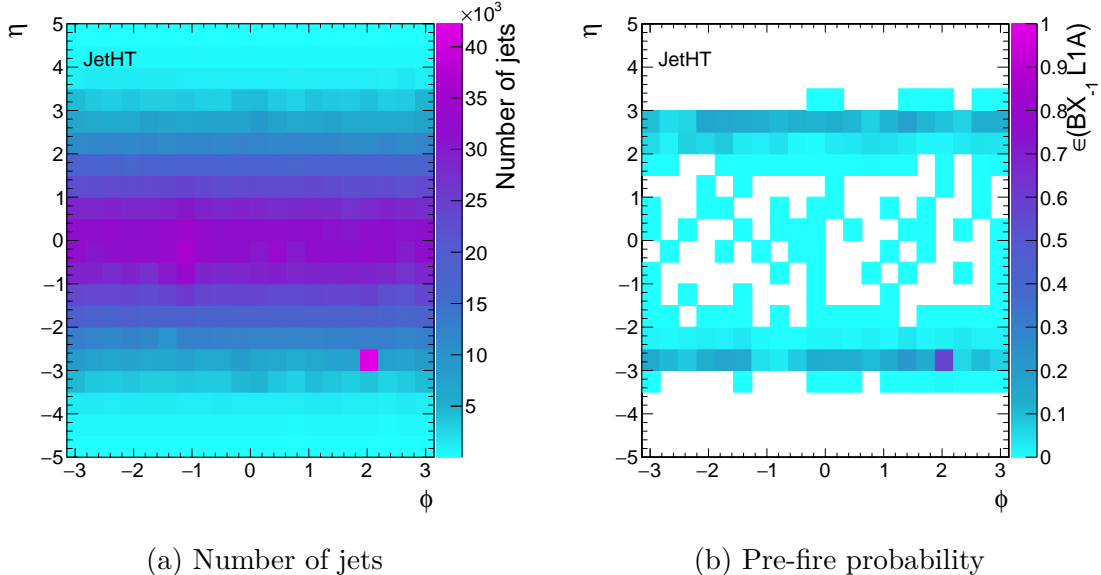


Figure 4.7: Distribution of jets and pre-fire events as a function of the jet location in the detector. Note the spike near $(\eta, \phi) = (-2.8, 2)$.

triggers (SingleMuon) are largely unaffected by the ECAL system, and therefore this measurement of $\epsilon_{\text{pre-fire}}$ is the least biased.

The probability of at least one jet pre-firing in an event is:

$$\epsilon_{\text{pre-fire}}^{\text{event}} = 1 - \prod_{j \in \text{jets}} \left(1 - \epsilon_{\text{pre-fire}}(p_T^j, \eta^j)\right) \quad (4.4)$$

The ϕ -dependence has been dropped, since it is clear from Figure 4.7 that the effect can be averaged over ϕ (once the spike is removed). Figure 4.10 shows $\epsilon_{\text{pre-fire}}(p_T, \eta)$ using muon-triggered and jet-triggered events. In the former case, statistical fluctuations make the region with $p_T > 250$ GeV unusable. Fortunately, this is the region in which the trigger bias is smallest, and so we switch to the jet triggered measurement above this threshold. A 20% uncertainty is assessed on the efficiency, which is derived from the difference between the SingleMuon and JetHT measurements.

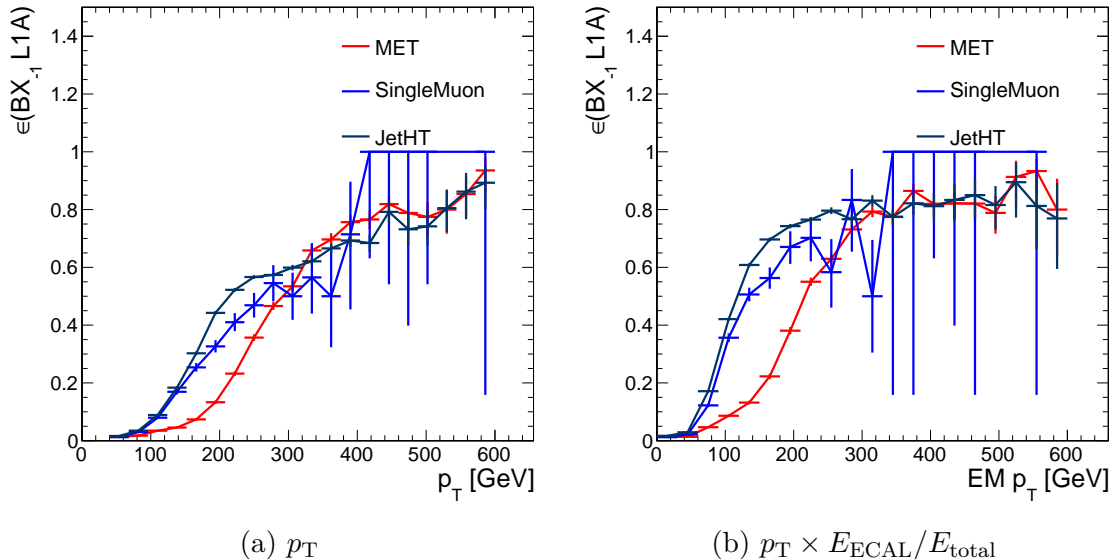


Figure 4.8: Probability that a given jet with $2.25 < |\eta| < 3$ causes a pre-fire in the L1 trigger due to ECAL mistiming. Two parameterizations are used: jet p_T and EM p_T . The three curves refer to which set of triggers are used to select BX_0 .

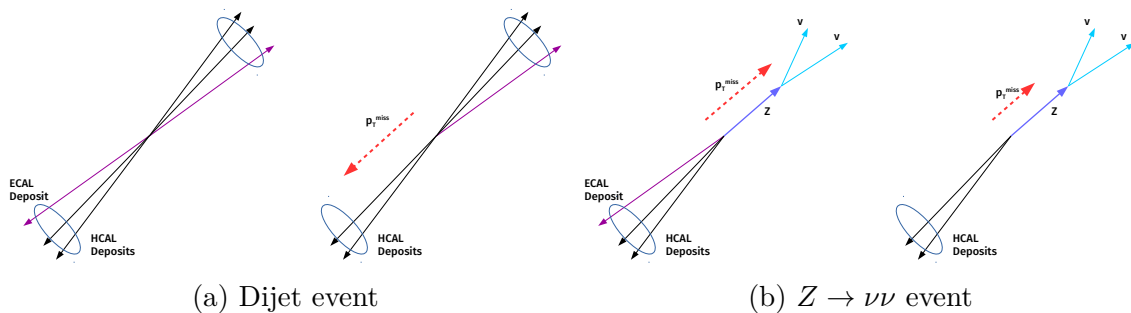


Figure 4.9: How zero suppression in the ECAL due to pre-firing can bias certain events. Subfigure (a) shows a dijet event, in which the loss of an ECAL deposit reduces the total H_T of the event, thereby lowering the probability of a jet-based trigger to fire. Subfigure (b) shows a $Z \rightarrow \nu\nu$ event, in which the loss of an ECAL deposit reduces the total p_T^{miss} of the event.

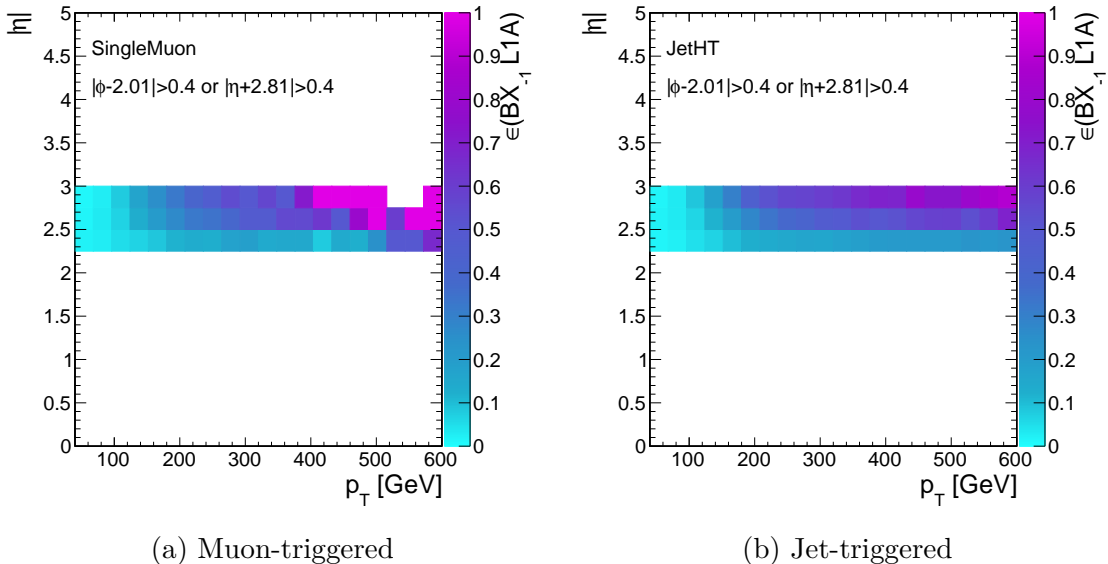


Figure 4.10: $\epsilon_{\text{pre-fire}}(p_T, \eta)$ with two different sets of reference triggers used to select BX_0 .

4.1.2 EW and QCD production of electroweak bosons

The primary backgrounds to the VBF production of invisibly-decaying Higgs bosons are $Z(\rightarrow \nu\nu)+2 \text{ jet}$ and $W(\rightarrow \ell\nu)+2 \text{ jet}$ production. At leading order, the relevant Feynman diagrams are either of the order $\alpha_{\text{EW}}^2 \alpha_{\text{QCD}}^4$ or α_{EW}^6 . We refer to the former as the QCD production mode and the latter as the EW mode. Examples Feynman diagrams are shown in Figure 4.11. The EW mode is essentially vector boson fusion, and so the terms EW and VBF will be used interchangeably.

As the vector boson is not directly detectable, the only experimental signatures are the jets. The jet kinematics are sensitive to the production mode (vector boson fusion vs QCD), as well as the spin of the produced boson. Some conclusions can be drawn from the kinematic distributions (Figure 4.12):

1. The yield ($\sigma \times A$) of the three VBF processes are relatively close in the relevant phase space (assuming $\mathcal{B}(H \rightarrow \chi\bar{\chi}) = 1$), but the QCD processes are 1-2 orders of magnitude higher.
2. The jet p_T and p_T^{miss} distributions in the signal are comparable to or softer than

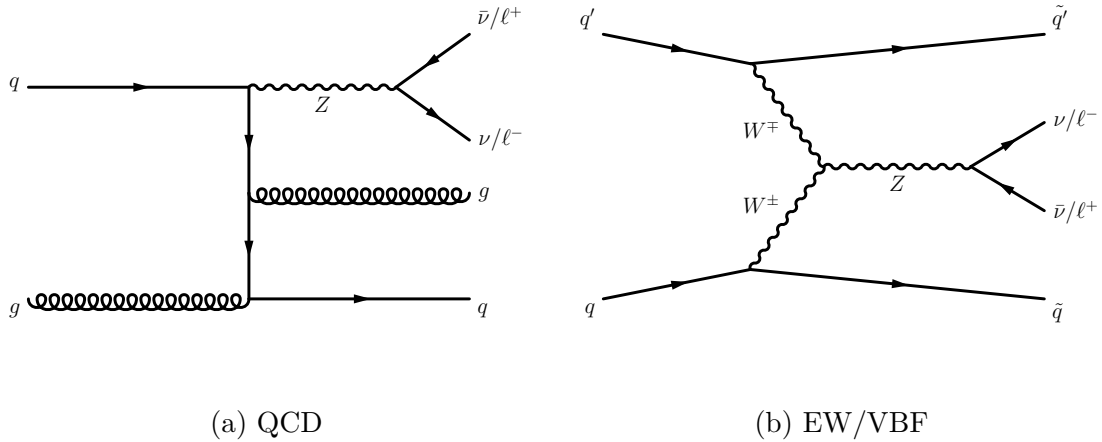


Figure 4.11: Examples of the two modes of producing Z bosons in association with 2 jets. Similar diagrams exist for W boson production.

the background processes. This is in contrast to other DM searches, in which the signal p_T^{miss} distribution is much harder than SM predictions.

3. VBF $H \rightarrow \chi\bar{\chi}$ produces fewer jets than SM processes.
4. VBF $H \rightarrow \chi\bar{\chi}$ produces relatively forward jets. QCD $V+\text{jets}$ produces mostly central jets. VBF $V+\text{jets}$ produces jets that are somewhere between these distributions.

To fully exploit these kinematic distributions, we look at “VBF-tag” observables, which are functions of the two leading jets. These are defined as:

m_{jj} : Invariant mass of the dijet system.

$\Delta\eta_{jj}$: Absolute value of the difference in pseudorapidity of the two jets.

$\Delta\phi_{jj}$: Absolute value of the difference in azimuthal angle of the two jets.

These distributions are shown in Figure 4.13. The first two distributions look different in QCD and VBF processes and are therefore useful to reduce QCD backgrounds. On the other hand, $\Delta\phi_{jj}$ is sensitive to the spin of the boson produced in a VBF process, and therefore can distinguish between Higgs and electroweak boson production.

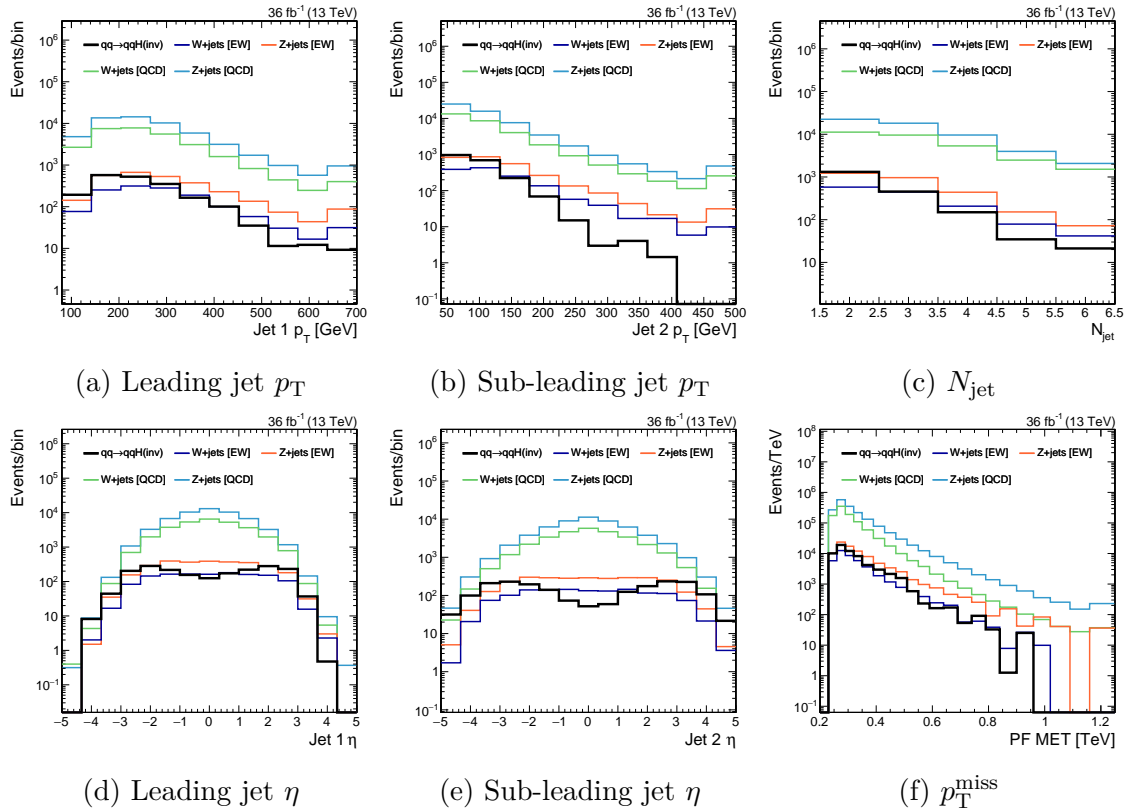


Figure 4.12: Event kinematic distributions, as compared between H vs Z vs W production, and VBF vs QCD modes.

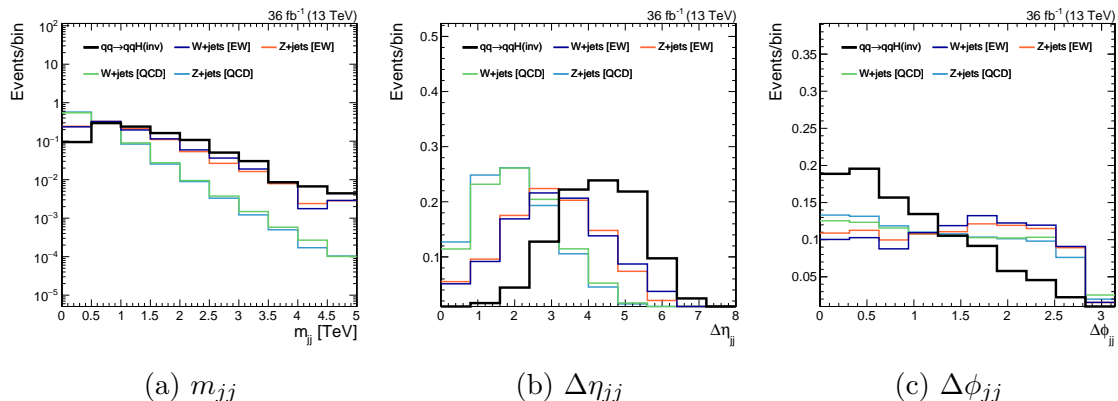


Figure 4.13: VBF tag observable distributions, as compared between H vs Z vs W production, and VBF vs QCD modes.

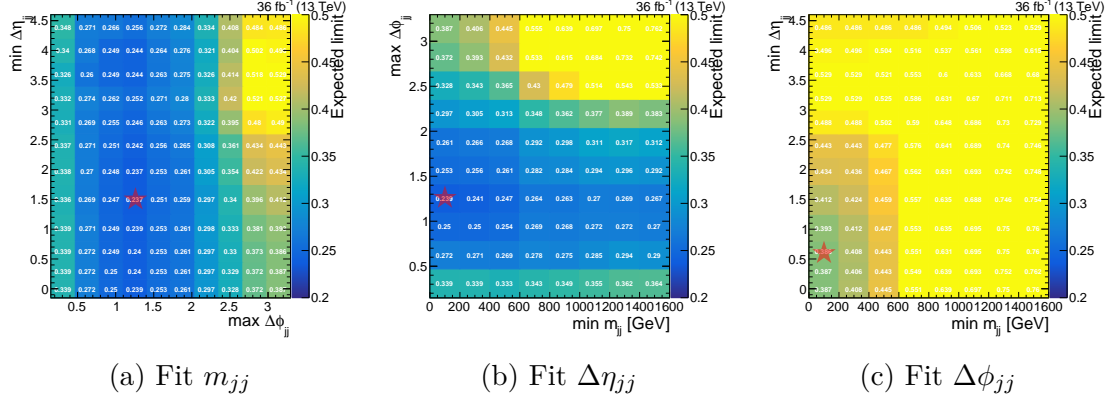


Figure 4.14: Optimization of the dijet kinematic selection, in three different fitting distribution scenarios.

4.1.3 Sensitivity optimization

A “baseline” selection is defined as:

- $p_T^{\text{miss}} > 250$ GeV: driven by trigger efficiency, as discussed in Section 4.1.1.
- $p_T^{\text{jet}} > 80, 40$ GeV: require two VBF jets, lower p_T thresholds set by trigger efficiency
- $N_{e,\mu,\tau,\gamma} = 0$: veto leptonic decays of Z and W , $t\bar{t}$, diboson production, γ +jet, etc.
- $\min \Delta\phi(\text{jet}, p_T^{\text{miss}}) > 0.4$: remove QCD multijet events.
- $|p_{T,\text{calo}}^{\text{miss}} - p_T^{\text{miss}}| < p_T^{\text{miss}}/2$: remove miscalibrated events.

As the tag variables each show some level of separation between signal and backgrounds, we can choose to either fit the distributions or use them to select events. To find the optimal choice, we fit each of the distributions in turn, and scan the other two observables. The details of this fit and the background estimation are described in Section 4.2. The metric is chosen to be the expected 95% CLs upper limit on $\mathcal{B}(H \rightarrow \chi\bar{\chi})$. Figure 4.14 shows the result of this optimization. The dijet mass is found to be the best distribution to fit, while requiring $\Delta\eta_{jj} > 1$ and $\Delta\phi_{jj} < 1.5$.

4.2 Background estimation

To estimate the combined m_{jj} spectra of the EW and QCD V +jet backgrounds, we employ a similar visible-to-invisible strategy as described in Section 3.2. In this case, the transfer factors \mathbf{T} are a function of m_{jj} . Control regions are defined using dilepton (single-lepton) selections to estimate the Z (W) contributions. Again, p_T^{miss} is replaced by U (Equation 3.7) to mimic the signal region selection. Because there are *two* components to estimate in each CR (QCD and EW), we slightly modify the likelihood. Adding only the $\mu\mu$ CR to constrain the Z +jet component for now:

$$\begin{aligned} \mathcal{L}(\mathbf{d} | \mu, \boldsymbol{\mu}_{\text{SR}}^{Z \rightarrow \nu\nu}, \boldsymbol{\theta}) = \prod_{i \in \text{bins}} & \left[\text{Pois} \left(d_i^{\text{SR}} \mid \mu S_i^{\text{SR}}(\boldsymbol{\theta}) + \mu_{\text{SR},i}^{Z \rightarrow \nu\nu} + \frac{\mu_{\text{SR},i}^{Z \rightarrow \nu\nu}}{T_{Z,i}^{\text{QE}}(\boldsymbol{\theta})} + B_i^{\text{SR}}(\boldsymbol{\theta}) \right) \right. \\ & \times \text{Pois} \left(d_i^{\mu\mu} \mid \frac{\mu_{\text{SR},i}^{Z \rightarrow \nu\nu}}{T_{Z,i}^{\mu\mu}(\boldsymbol{\theta})} + \frac{\mu_{\text{SR},i}^{Z \rightarrow \nu\nu}}{T_{Z,i}^{\mu\mu}(\boldsymbol{\theta}) T_{Z,i}^{\text{QE}}(\boldsymbol{\theta})} + B_i^{\mu\mu}(\boldsymbol{\theta}) \right) \left. \right] \\ & \times \prod_{j=0}^{n_\theta} p_j(\theta_j) \end{aligned} \quad (4.5)$$

While the notation largely follows that used in Equation 3.11, one additional term has been introduced. This is a “transfer factor” linking the QCD and EW components in the signal region, so that the only free parameter is $\boldsymbol{\mu}_{\text{SR}}^{Z \rightarrow \nu\nu}$:

$$T_{Z,i}^{\text{QE}} = \frac{N_i^{\text{SR}}(\text{QCD } Z \rightarrow \nu\nu)}{N_i^{\text{SR}}(\text{EW } Z \rightarrow \nu\nu)} \quad (4.6)$$

where as always, the yields N are predicted using MC. Kinematic distributions from the two dilepton CRs are shown in Figure 4.15.

In the region $m_{jj} > 2.5$ TeV, the statistical power of the dilepton regions is extremely limited. For this reason, and to estimate the W +jets contribution in the SR, we add two single-lepton CRs in analogy to what is done in Section 3.2. Figure 4.16 shows the level of agreement between the data and MC in these CRs. The likelihood

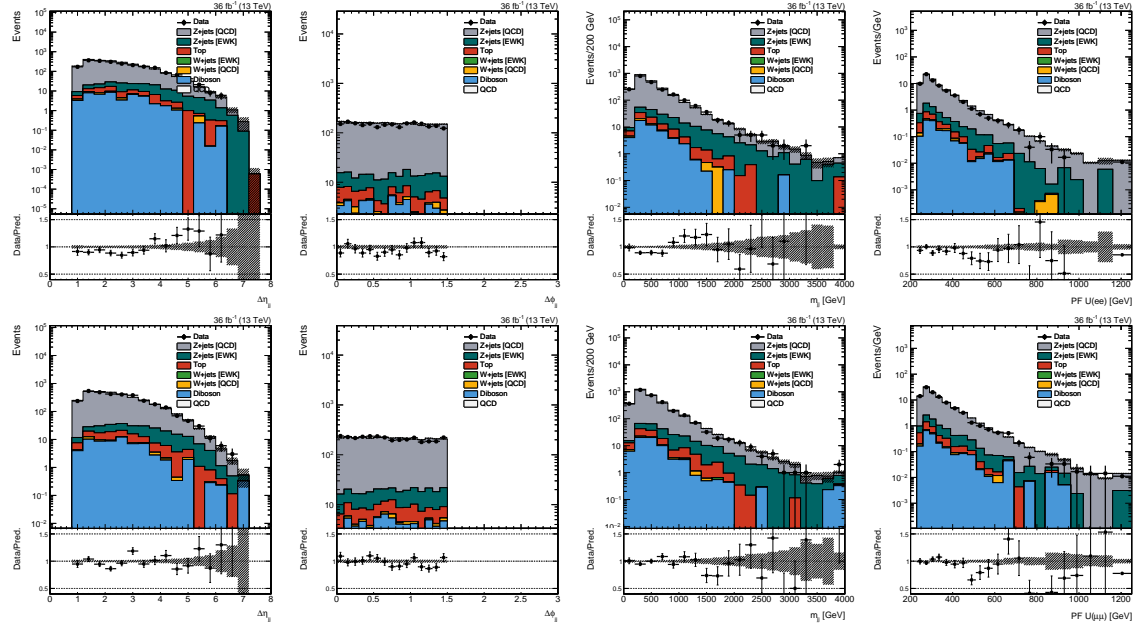


Figure 4.15: Dijet and recoil distributions in the dielectron (top) and dimuon (bottom) CRs.

is modified to include the constraints of the single-lepton CRs:

$$\begin{aligned} \mathcal{L}(\mathbf{d} | \mu, \boldsymbol{\mu}_{\text{SR}}^{Z \rightarrow \nu\nu}, \boldsymbol{\theta}) = & \\ \prod_{i \in \text{bins}} \left[\text{Pois} \left\{ d_i^{\text{SR}} \mid \mu S_i^{\text{SR}}(\boldsymbol{\theta}) + \left(1 + \frac{1}{T_{Z,i}^{\text{QE}}(\boldsymbol{\theta})} \right) \left(1 + \frac{1}{T_{Z/W,i}^{\text{SR}}(\boldsymbol{\theta})} \right) \mu_{\text{SR},i}^{Z \rightarrow \nu\nu} + B_i^{\text{SR}}(\boldsymbol{\theta}) \right\} \right. & \\ \times \prod_{X=\mu,e} \text{Pois} \left\{ d_i^X \mid \left(1 + \frac{1}{T_{Z,i}^{\text{QE}}(\boldsymbol{\theta})} \right) \frac{\mu_{\text{SR},i}^{Z \rightarrow \nu\nu}}{T_{W,i}^X(\boldsymbol{\theta}) T_{Z/W,i}^{\text{SR}}(\boldsymbol{\theta})} + B_i^X(\boldsymbol{\theta}) \right\} & \\ \times \prod_{X=\mu\mu,ee} \text{Pois} \left\{ d_i^X \mid \left(1 + \frac{1}{T_{Z,i}^{\text{QE}}(\boldsymbol{\theta})} \right) \frac{\mu_{\text{SR},i}^{Z \rightarrow \nu\nu}}{T_{Z,i}^X(\boldsymbol{\theta})} + B_i^X(\boldsymbol{\theta}) \right\} \right] & \times \prod_{j=0}^{n_\theta} p_j(\theta_j) \quad (4.7) \end{aligned}$$

To validate that the transfer factors are reasonably well-simulated (within the assigned uncertainties), Figure 4.17 uses the following ratios of CRs as proxies for transfer

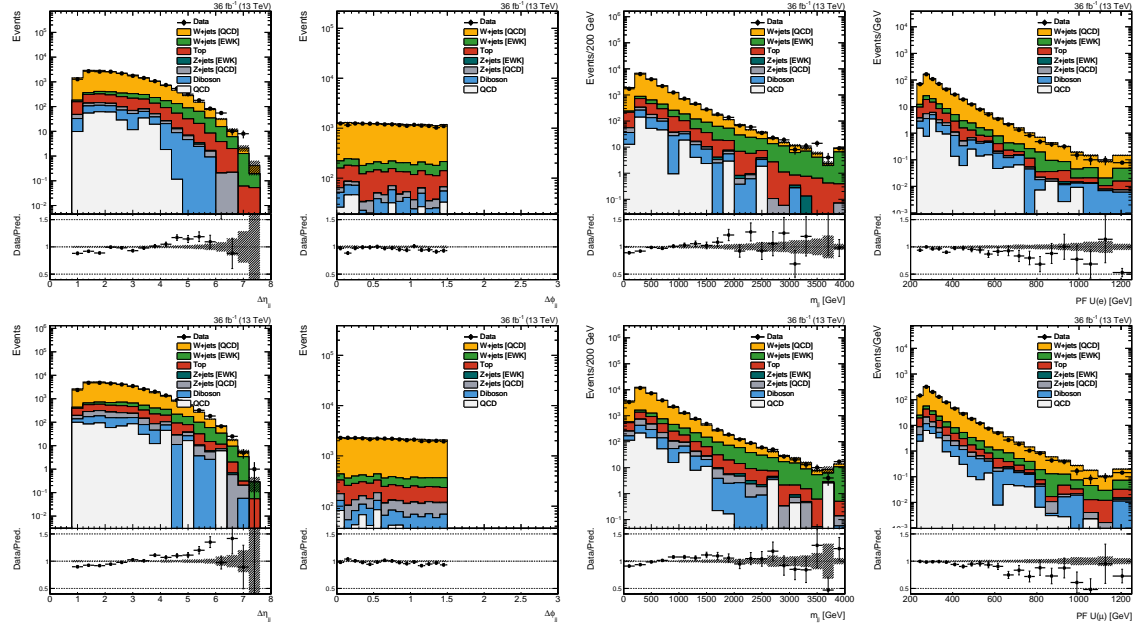


Figure 4.16: Dijet and recoil distributions in the single-electron (top) and single-muon (bottom) CRs.

factors:

$$\begin{aligned}
 \mathbf{T}_Z^{\mu\mu}, \mathbf{T}_Z^{ee} &\sim \frac{N_{\mu\mu}(Z \rightarrow \mu\mu)}{N_{ee}(Z \rightarrow ee)} \\
 \mathbf{T}_W^{\mu}, \mathbf{T}_W^e &\sim \frac{N_\mu(W \rightarrow \mu\nu)}{N_e(W \rightarrow e\nu)} \\
 \mathbf{T}_{Z/W}^{\text{SR}} &\sim \frac{N_\mu(W \rightarrow \mu\nu) + N_e(W \rightarrow e\nu)}{N_{\mu\mu}(Z \rightarrow \mu\mu) + N_{ee}(Z \rightarrow ee)}
 \end{aligned} \tag{4.8}$$

4.3 Results

The dijet mass distribution in data is fit in all signal and control regions, the results of which are shown in Figure 4.18. As no statistically significant excess over the Standard Model is observed, we translate the results into upper limits on the branching ratio of $H \rightarrow \chi\bar{\chi}$. As the signal hypothesis, both the VBF and gluon fusion (with 2 extra jets) Higgs production modes are considered; the latter contaminates the SR due to its relatively large cross section. After the signal region selection criteria, the

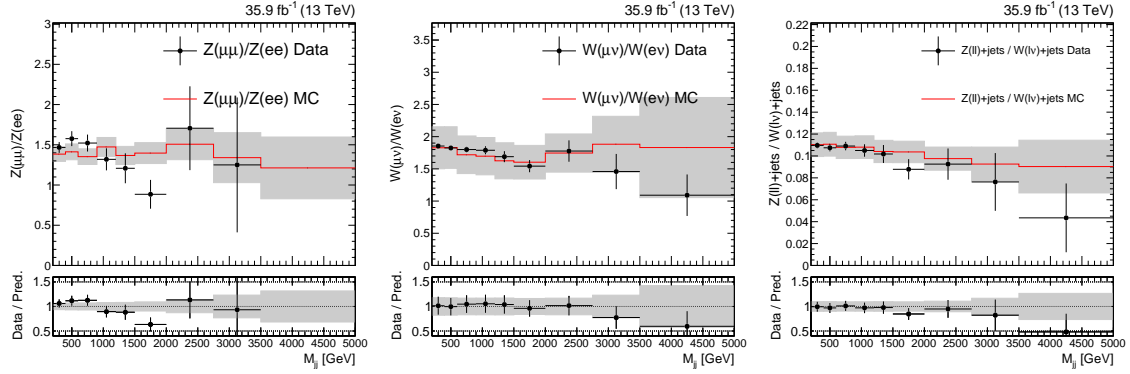


Figure 4.17: Validation of the VBF transfer factors using control region data. The transfer factor proxies are found to agree quite well with the data within the post-fit uncertainties

two modes contribute approximately equal yields. Assuming $m_H = 125$ GeV, the observed 95% CL upper limit is 0.33. Assuming a background-only hypothesis, the expected distribution of upper limits has median 0.33, with the 1 standard deviation band covering [0.18, 0.35]; the observation therefore represents an upwards fluctuation slightly under 1σ .

We further scan m_H and set upper limits on $\sigma(qq \rightarrow qqH)\mathcal{B}(H \rightarrow \chi\bar{\chi})$. The upper limits are shown in Figure 4.19, and the observed (expected) limits exclude $m_H < 540$ GeV (635 GeV) assuming a branching ratio of 100%.

As described in the beginning of this chapter, each Higgs production mode corresponds to a potential invisible Higgs search channel. While VBF is the most sensitive, the total sensitivity can be improved by statistically combining all channels. Other results from CMS cover searches for associated production of a Higgs boson, either with a leptonically-decaying Z boson ([??]) or a hadronically-decaying weak boson ([??]); and for gluon fusion production, with at least one jet originating from the initial state or heavy quark loop ([??]). The details of these searches are left to the referenced literature, but a summary of their results is provided in Figure 4.20. When statistically combining the results, most experimental nuisances are treated as correlated between the searches, with the exception of the VBF jet energy scale dependence. This is because the VBF category selects forward jets, whereas other

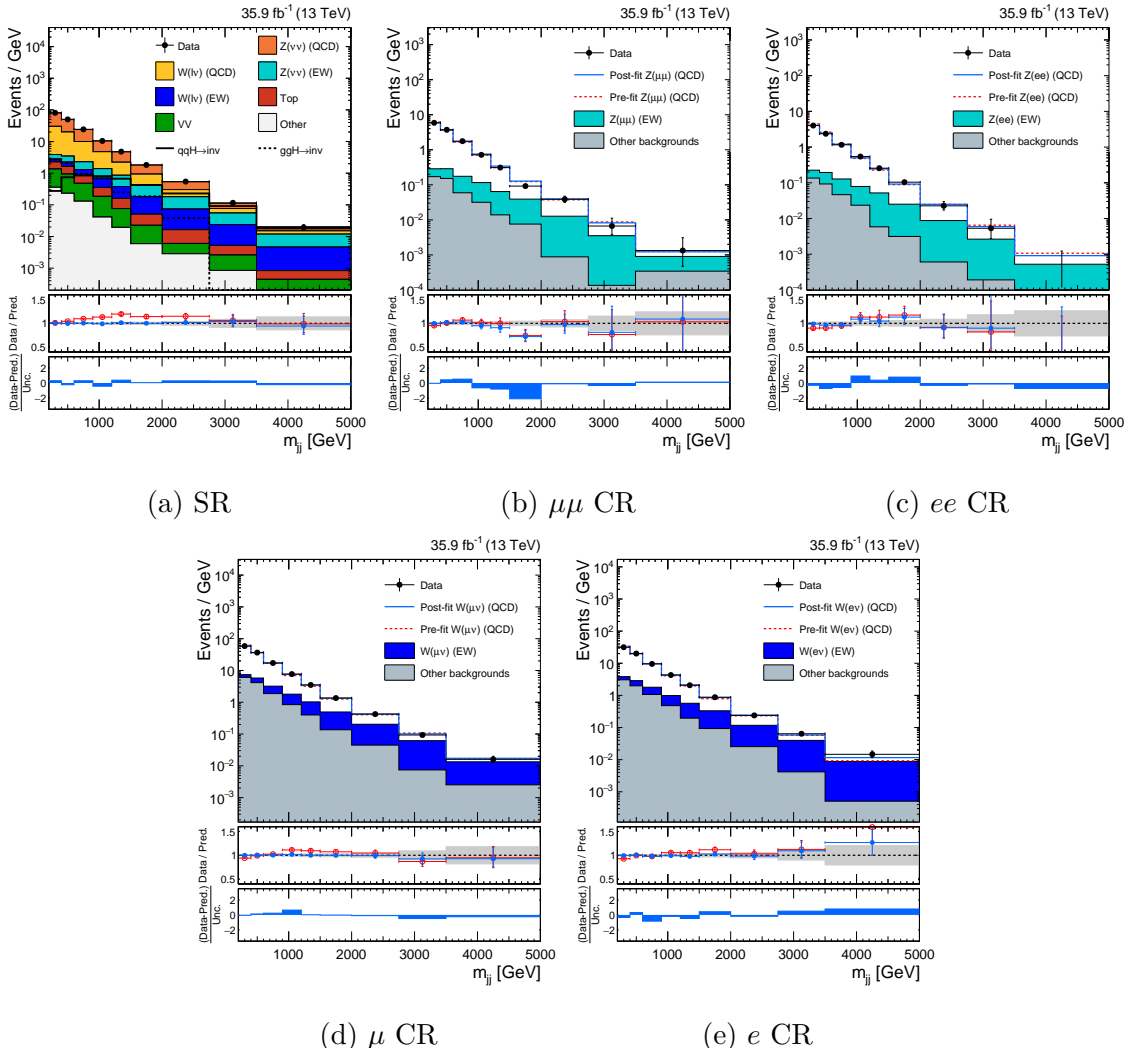


Figure 4.18: Post-fit m_{jj} distributions in the various signal and control regions. The uncertainties (gray bands) and bin pulls (blue bands) are defined by varying the nuisances by one standard deviation around the maximum likelihood estimate.

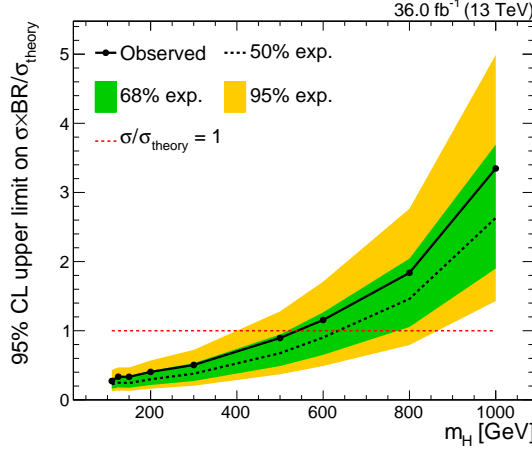


Figure 4.19: Upper limits on $\sigma \times \mathcal{B}/\sigma_{\text{theory}}$ as a function of m_H , where σ refers to the total production cross section of the Higgs boson with mass m_H . If one assumes that $\sigma = \sigma_{\text{theory}}$, then the upper limits can be interpreted directly as constraints on $\mathcal{B}(H \rightarrow \chi\bar{\chi})$.

searches generally probe central jets. Theoretical nuisances (e.g. those affecting W/Z or ZZ/WZ ratios) are left uncorrelated between all searches. The combined result constrains $\mathcal{B}(H \rightarrow \chi\bar{\chi})$ to be less than 0.26 at 95% CL, which approximately corresponds to a 1 standard deviation fluctuation upward relative to the median expected limit of 0.20.

Higgs-mediated DM can also be probed by direct detection (DD) experiments. We interpret the combined 90% CL upper limit (for consistency with DD conventions) on $\mathcal{B}(H \rightarrow \chi\bar{\chi})$ as an upper limit on the spin-independent cross section of DM-nucleon scattering. First, we convert the branching ratio into a partial width:

$$\Gamma_{H \rightarrow \chi\bar{\chi}} = \frac{\mathcal{B}(H \rightarrow \chi\bar{\chi}) \cdot \Gamma_{\text{SM}}}{1 - \mathcal{B}(H \rightarrow \chi\bar{\chi})}, \text{ where } \Gamma_{\text{SM}} = 4 \text{ GeV} \quad (4.9)$$

Then, using the results described in Reference [??], $\Gamma_{H \rightarrow \chi\bar{\chi}}$ is translated into $\sigma_{\chi N}^{\text{SI}}(m_\chi)$, where the only free parameter is the DM mass. Figure 4.21 compares the CMS exclusions with those from DD experiments [??]. Also shown for comparison is the “neutrino floor”, which is the cross section of coherent scattering of solar neutrinos, and a limiting factor for DD experiments. At low m_χ , CMS is able to significantly

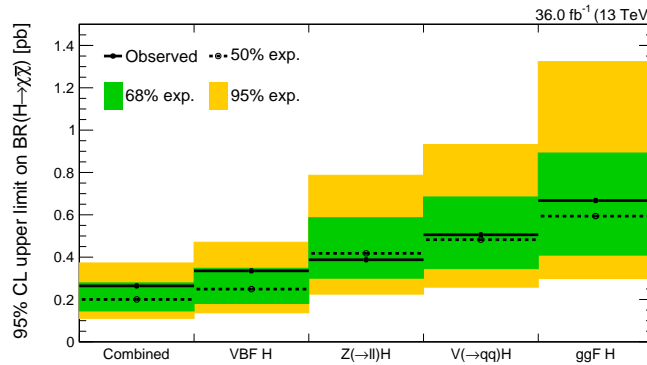


Figure 4.20: Upper limits on $\mathcal{B}(H \rightarrow \chi\bar{\chi})$ after statistically combining all of the CMS searches for $H \rightarrow \chi\bar{\chi}$ conducted on 36 fb^{-1} of data collected in 2016. For comparison, the upper limits of each of the individual categories are also shown.

extend the DD constraints, reaching well below the neutrino floor.

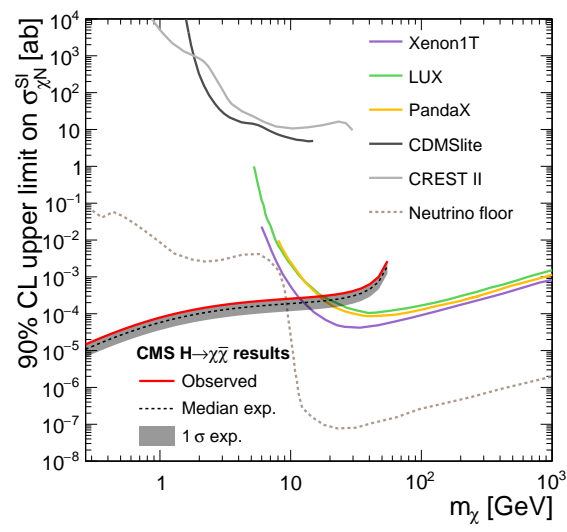


Figure 4.21: Upper limits on $\sigma_{\chi N}^{\text{SI}}$ as a function of m_χ . Shown are the combined results from the CMS invisible Higgs searches, as well as various direct detection experiments.

Bibliography

- [1] W Adam, R FrÄijhwirth, A Strandlie, and T Todorov. Reconstruction of electrons with the gaussian-sum filter in the cms tracker at the lhc. *Journal of Physics G: Nuclear and Particle Physics*, 31(9):N9, 2005.
- [2] Richard D. Ball, Valerio Bertone, Stefano Carrazza, Christopher S. Deans, Luigi Del Debbio, Stefano Forte, Alberto Guffanti, Nathan P. Hartland, Jos  I. Latorre, Juan Rojo, and Maria Ubiali. Parton distributions for the LHC Run II. *JHEP*, 04:040, 2015.
- [3] G. L. Bayatian et al. CMS Physics Technical Design Report, Volume I: Detector Performance and Software. 2006.
- [4] A Benaglia et al. The CMS ECAL performance with examples. *Journal of Instrumentation*, 9(02):C02008, 2014.
- [5] M. Benedikt, P. Collier, V. Mertens, J. Poole, and K. Schindl. LHC Design Report. 3. The LHC injector chain. 2004.
- [6] Cristina Biino. The CMS Electromagnetic Calorimeter: overview, lessons learned during Run 1 and future projections. *Journal of Physics: Conference Series*, 587(1):012001, 2015.
- [7] P. Billoir and S. Qian. Simultaneous pattern recognition and track fitting by the kalman filtering method. *Nuclear Instruments and Methods in Physics Research Section A: Accelerators, Spectrometers, Detectors and Associated Equipment*, 294(1):219 – 228, 1990.
- [8] Serguei Chatrchyan et al. Description and performance of track and primary-vertex reconstruction with the CMS tracker. *JINST*, 9(10):P10009, 2014.
- [9] Sergui Chatrchyan et al. The CMS experiment at the CERN LHC. *Journal of Instrumentation*, 3(08):S08004, 2008.
- [10] CMS Collaboration. https://twiki.cern.ch/twiki/bin/view/CMSPublic/SWGuideGlobalHLT#Trigger_development_for_Run_2.
- [11] D. de Florian et al. Handbook of LHC Higgs Cross Sections: 4. Deciphering the Nature of the Higgs Sector. Technical Report FERMILAB-FN-1025-T, Oct

2016. 869 pages, 295 figures, 248 tables and 1645 citations. Working Group web page: <https://twiki.cern.ch/twiki/bin/view/LHCPhysics/LHCHXSWG>.

- [12] Cinzia De Melis. The CERN accelerator complex. *Complexe des accélérateurs du CERN*. Jan 2016. General Photo.
- [13] Ansgar Denner, Stefan Dittmaier, Tobias Kasprzik, and Alexander Mück. Electroweak corrections to $W +$ jet hadroproduction including leptonic W -boson decays. *JHEP*, 08:075, 2009.
- [14] Ansgar Denner, Stefan Dittmaier, Tobias Kasprzik, and Alexander Mück. Electroweak corrections to dilepton + jet production at hadron colliders. *JHEP*, 06:069, 2011.
- [15] Ansgar Denner, Stefan Dittmaier, Tobias Kasprzik, and Alexander Mück. Electroweak corrections to monojet production at the LHC. *Eur. Phys. J. C*, 73:2297, 2013.
- [16] Daniel Abercrombie *et al.* Dark Matter Benchmark Models for Early LHC Run-2 Searches: Report of the ATLAS/CMS Dark Matter Forum. 2015.
- [17] Lyndon Evans and Philip Bryant. LHC Machine. *JINST*, 3:S08001, 2008.
- [18] R. Fruehwirth. Application of kalman filtering to track and vertex fitting. *Nuclear Instruments and Methods in Physics Research Section A: Accelerators, Spectrometers, Detectors and Associated Equipment*, 262(2):444 – 450, 1987.
- [19] R Fruehwirth, Wolfgang Waltenberger, and Pascal Vanlaer. Adaptive Vertex Fitting. Technical Report CMS-NOTE-2007-008, CERN, Geneva, Mar 2007.
- [20] Stefan Kallweit, Jonas M. Lindert, Philipp Maierhöfer, Stefano Pozzorini, and Marek Schönher. NLO electroweak automation and precise predictions for $W+multijet$ production at the LHC. *JHEP*, 04:012, 2015.
- [21] Stefan Kallweit, Jonas M. Lindert, Stefano Pozzorini, Marek Schönher, and Philipp Maierhöfer. NLO QCD+EW automation and precise predictions for $V+multijet$ production. In *50th Rencontres de Moriond on QCD and High Energy Interactions La Thuile, Italy, March 21-28, 2015*, 2015.
- [22] Vardan Khachatryan *et al.* Performance of Photon Reconstruction and Identification with the CMS Detector in Proton-Proton Collisions at $\sqrt{s} = 8$ TeV. *JINST*, 10(08):P08010, 2015.
- [23] Johann H. Kuhn, A. Kulesza, S. Pozzorini, and M. Schulze. Logarithmic electroweak corrections to hadronic $Z+1$ jet production at large transverse momentum. *Phys. Lett. B*, 609:277, 2005.
- [24] Johann H. Kuhn, A. Kulesza, S. Pozzorini, and M. Schulze. One-loop weak corrections to hadronic production of Z bosons at large transverse momenta. *Nucl. Phys. B*, 727:368, 2005.

- [25] Johann H. Kuhn, A. Kulesza, S. Pozzorini, and M. Schulze. Electroweak corrections to hadronic photon production at large transverse momenta. *JHEP*, 03:059, 2006.
- [26] Johann H. Kuhn, A. Kulesza, S. Pozzorini, and M. Schulze. Electroweak corrections to hadronic production of W bosons at large transverse momenta. *Nucl. Phys. B*, 797:27, 2008.
- [27] K. Rose. Deterministic annealing for clustering, compression, classification, regression, and related optimization problems. *Proceedings of the IEEE*, 86(11):2210–2239, Nov 1998.
- [28] A. M. Sirunyan et al. Particle-flow reconstruction and global event description with the CMS detector. *JINST*, 12(10):P10003, 2017.
- [29] A. M. Sirunyan et al. Identification of heavy-flavour jets with the CMS detector in pp collisions at 13 TeV. *JINST*, 13(05):P05011, 2018.
- [30] A. M. Sirunyan et al. Performance of the CMS muon detector and muon reconstruction with proton-proton collisions at $\sqrt{s} = 13$ TeV. *JINST*, 13(06):P06015, 2018.